Fast and Sensitive Detection of Bacteria by Means of

AC Electrokinetics and Micro-Raman Spectroscopy

By

David Shiqi Liao

A thesis submitted to the Department of Chemical Engineering

In conformity with the requirements for the

Degree of Master of Applied Science

Queen's University

Kingston, Ontario, Canada

November 2015

Abstract

Rapid diagnosis of pathogens requires the ability to detect the presence of a target pathogen in a sample at as low concentrations as possible. In the present thesis, a surface-based method that can provide early and label-free detection of target microorganisms in water is presented. The method combines three key features, namely, (a) accelerated transportation to, and focusing of bacteria on, the detection surface by means of alternating current (AC) electrokinetic effects; (b) selective capture of the target microorganism using surface-immobilized antibodies; (c) sensitive detection of target bacteria with micro-Raman spectroscopy. The non-uniform electric field is created by an AC signal-driven planar, quadrupolar, gold microelectrode array that is deposited on the detection surface (oxidized silicon wafer). The combined effects of AC electroosmosis and dielectrophoresis concentrated the bacteria onto a surface within a few minutes. Bacterial detection is subsequently, accomplished through Raman spectra acquired at pre-determined locations near the electrodes after sample removal and rinsing of the capture surface. Detection was successful at concentrations as low as 10^2 bacteria/mL using a sample volume of 50 μL. The method is sensitive enough to detect the capture of a single bacterium.

The bacterial capture efficiency was found to be strongly dependent on the selection of the applied voltage and AC frequency values. Tests performed in the range 1-20 V_{pp} and 1 kHz-1 MHz showed that the most effective operating conditions was (12 V_{pp}, 10 kHz). Overall, high bacteria capture efficiencies were observed at low frequencies (≤10 kHz).

The mechanism of bacteria capture was investigated with the aid of numerical simulations. It was found that the capture efficiency was very high under electric field conditions that cause a strong AC electroosmotic effect. The simulations results were in qualitative agreement with the experimental observations.

Acknowledgements

I would like to thank my supervisor, Dr. Aristides Docoslis, for this opportunity to perform research for his group at Queen's University, as well as his support and guidance. I would like to thank Ms. Shiva Golchi, who trained me on the laboratory equipment and experimental procedures. Also, credits should go to Mr. Joshua Raveendran for his help with the Matlab coding, as well as Dr. Shane Guo for his guidance with the simulations.

The help of technical staff was invaluable, and I appreciate the support of Mr. Steven Hodgson and Ms. Kelly Sedore. The bacteria strains used in the experiments were generously donated by Ms. Dorothy Agnew (department of Biomedical and Molecular Sciences, Queen's University).

Table of Contents

List of Figures

List of Tables

List of Abbreviations

EK - Electrokinetic

EO - Electroosmotic / Electroosmosis

EDL - Electric double layer

ET - Electrothermal

DEP - Dielectrophoresis

CM - Clausius Mossotti

V_{PP} - Volts, peak to peak

V_{rms} - Volts, root mean squared

twEO - Traveling wave electroosmosis

AC - Alternating current

E. coli - *Escherichia coli*

M. luteus *Micrococcus luteus*

CFU - Colony forming units

List of Symbols

Symbol	Unit	Description		Symbol	Unit	Description
C_{DL}	F/m²	Double layer capacitance		E	V/m	Electric field
F_{DEP}	N	Dielectrophoretic force		Ke	-	Clausius Mossotti factor
K_B	J/K	Boltzmann's constant		Pe_L	-	Peclet number
p	Pa	Pressure		T	K	Temperature
U_{wall}	m/s	EO fluid velocity at the end of EDL		V	V	Potential
V	V	Potential in Bulk		a	m	particle radius
V_0	V	Applied Voltage		k	W/(m*K)	thermal conductivity
V_s	V	Potential at the end of EDL		q	C/m²	Charge of EDL per unit area
e_0	C	Electron Charge		t	S	Time
ε_m	F/m	Electric permittivity of medium		z	-	Ion charge number
ε_p	F/m	Electric permittivity of particle		η	Pa*s	dynamic fluid viscosity
ε_r	-	relative permittivity of water		ν	m	Effective size of Ion
Λ	-	ACEO correction factor		ρ	C/m²	Surface Charge Density
CFU	-	Colony Forming Units		σ	S/m	Conductivity of medium
G	m/s²	Acceleration of gravity				

1.0 - Introduction

The United States market for pathogen detection is estimated to be $214 million USD in 2015 [1], signifying the importance of preventing the spread of pathogens. Though there is no standard in the field of 'rapid' pathogen detection, the method involved would preferably have the three desired attributes: it would produce accurate and reliable results, the results would be available within a sufficiently quick time, and it would be portable to provide point-of-care testing. Portability is especially important to put into practice. Without the portability aspect, samples must be sent to a central location, and analysis would have to be performed sequentially. But with portable, automated, point of care analysis, test kits could be sent to the sampling location and tests can be performed in parallel and results delivered on site. This is especially important for the detection of pathogens such as *Escherichia coli*, *Ebola*, and *Vibrio cholera*.

For bacteria, the traditional method of testing is the bio-chemical test. Bacteria are cultured in various media and the cultures are tested for metabolic products. Typically, many different tests are done simultaneously in an assay. The bacteria are placed inside various media, each with a chemical to determine the presence of a characteristic metabolite. By analysing the combination of metabolites produced, the species of bacteria could be determined. Although this test is reliable and easily transportable, it requires time for the bacteria to grow to a detectable concentration. Cultivation times typically range from 8 to 14 hours. Similarly, tests such as serological tests and phage typing that test the reactions of bacteria to antibodies and viruses, respectively, also require cultivation prior to testing. [2]

Analytical methods for bacteria which don't require high concentrations includes flow cytometry, and DNA/RNA based methods. Flow cytometry passes a stained or otherwise labelled cell suspension through a micro-channel such that the cells are aligned in single file. The cells are then sequentially detected through laser based methods. [3] Since individual cells are analysed, very dilute concentrations

can be used. DNA based methods can use the polymerase chain reaction to amplify a cell's DNA concentration within 2-3 hours prior to testing through gel electrophoresis or more advanced methods such as hybridization arrays. [4] There have been developments in portable PCR technology from companies such as Ahram Biosystems, and BioFire Defence, and also portable flow cytometry systems such as the one by Handyem. However, these technologies have yet to be included in standards set by the Centre for Disease Control and the World Health Organization.

There are portable testing methods available, such as hemagglutination tests and more recently, the test for Ebola by ReEBOV. Hemagglutination works on the theory that with certain antibodies, bacteria and viruses will cause blood cells to coagulate. However, blood coagulation may be affected by other reasons, thus increasing the probability for false positives or negatives. Similarly, the ReEBOV test works by binding the Ebola virus in the medium (blood, semen, etc.) to gold nanoparticles functionalized with antibodies, then separating the gold nanoparticles from the medium through thin layer chromatography. Some nanoparticles will be coagulated through the virus, and will travel a shorter distance than the uncoagulated particles. A positive result would then result in two distinct lines on the column. This test was proven to have an 8% chance of identifying false negatives and a 15% chance of identifying false positives, as proven by the WHO. [5]

In an effort to increase portability, reduce the amount of reagents required, and to decrease analysis time, there has been much research and effort invested into miniaturizing current pathogen detection methods using micro-fluidics and MEMS. At this scale, effects of the electric field on particles and fluids become more significant than other forces such as gravity and buoyancy. This is known as electrokinetic phenomena. At this scale, it would allow for functions such as individual cell capture and manipulation, or non-mechanical microfluidic pumping.

1.1 Objectives

The objective of this thesis is to explore a novel method for fast and sensitive detection of bacteria contained in mL sized water droplets. The method combines AC electrokinetic effects, generated by a planar quadrupolar microelectrode array, with micro-Raman spectroscopy. During this study, the influence of electric field parameters (voltage, AC frequency) and bacteria concentration on the "sampling" efficiency of the microelectrode array, i.e., its ability to cause accelerated focusing and capture of bacteria on predetermined locations on the detection surface, will be investigated.

The mechanism by which electric field-generated phenomena can cause accelerated bacteria capture on the surface of quadrupolar microelectrodes will also be investigated with the aid of numerical simulations. The flow field and force field experienced by bacteria during microelectrode operation under the most promising experimental conditions will be investigated in order to correlate the effect of the latter with the observed sampling performance. Since the ultimate target of this project is the development of an accelerated bacteria sampling and detection technique for tests in drinking and recreational water (lakes, pools); therefore, the study will be restricted to aqueous bacterial suspensions of low electrical conductivity on the order of 1 mS/m.

1.2 Thesis Outline

Chapter 2 provides an introduction to electrokinetic phenomena that are most commonly used for bacteria capture and concentration. A literature survey on the applications of Raman spectroscopy towards bacteria detection and identification is provided

Chapter 3 provides the details of the materials used and methods employed in this work for conducting the experimental tests and numerical simulations.

Chapter 4 contains the results and analysis of the experiments, whereas Chapter 5 contains the results and analysis of numerical simulations of the microchip. The results will first be correlated with the

relevant theory behind electrokinetic. They will then be used to provide an explanation for the effects of varying operating conditions.

Chapter 6 gives conclusions and recommendations for future research.

2.0 - Background

2.1 – Theory of AC Electrokinetics

Electrokinetic phenomena involves the action of an electric field on either inherent or induced charges. These charges are resent in the fluid, resulting in some motion of the fluid, or in a particle, resulting in some motion of the particle. Similarly, the motion of these charges through some other sources (gravitational, pressure gradient, acoustic, etc.) would result in a potential, or current. In the context of this thesis, the focus will be on electrokinetic phenomena present under an alternating current (AC), namely: dielectrophoresis, electrothermal flow, and AC electroosmosis.

The AC electroosmotic force (EO) is generated when a tangential component of the electric field interacts with the electrical double layer (EDL) on the surface of the electrode. This results in a flow within the diffuse layer of the EDL. Through viscous and inertial effects, this velocity is then transferred into the bulk.

The electrothermal force on the liquid (ET) is the result of an electric field interacting with a temperature gradient. The temperature gradient creates a gradient in dielectric properties within the liquid. When an electric field is applied, force gradient is experienced in the liquid.

Dielectrophoresis (DEP) is a force experienced by a particle within an electric field gradient. With a gradient in the electrical field, there will be a force gradient throughout the particle. This net force will either be in the direction of the electric field gradient (positive DEP) or in the opposite direction of the electric field gradient (Negative DEP).

2.1.1 - Electric Field

Alternating current (AC) electrokinetic phenomena, such as AC dielectrophoresis, AC electroosmosis, and electrothermal flow, are all dependent on the electric field, described using poisson's equation, or more specifically, gauss's law:

$$\nabla \cdot (-\varepsilon_m \cdot \nabla V) = \rho \qquad \text{(Eq 1)}$$

Where V is the electrical potential throughout the medium, ε_m is the electric permittivity of the medium, and ρ is the charge density. In the bulk, the charge density is taken to be equal to zero. So, it simplifies down to the Laplace equation, assuming the permittivity is isotropic:

$$\nabla^2 V = 0 \qquad \text{(Eq 2)}$$

Generally speaking, the surface potential between water and another phase induces a phenomenon called the electrical double layer, where induced or inherent charges from the water will migrate towards the surface, creating a shielding effect in response to the surface potential. Within the electrical double layer, the charge density, ρ, is not zero, and the Laplace equation cannot be applied.

The surface potential on the electrodes changes with respect to time, due to an alternating voltage being applied. Therefore, the electrical double layer (EDL) will also be transient and frequency dependent, due to the amount of time needed for the EDL to charge. In numerical simulations, the electrical double layer is typically modeled as a discontinuous layer, due to insufficiently small element sizes. Similar to a capacitor, it will charge and discharge. And the time averaged behaviour of the EDL will be frequency dependent. If we assume that the electrical double layer is acting as a discrete capacitor, and the electrode system behaves like an RC circuit, then we can model the double layer capacitance through a charge balance, [6] displayed in (Eq 3).

$$\sigma \frac{\partial V_s}{\partial n} = \frac{\partial q}{\partial t} \qquad \text{(Eq 3)}$$

Where q is the charge of the electrical double layer per unit area, and $\partial V_S/\partial n$ is the normal component of the electrical field at boundary between the EDL and the bulk. The time-averaged solution can be found by taking the Fourier transform. For low voltages, and thin double layers, it can be assumed that there is a linear relationship between the charge and the voltage, and the surface charge can be simplified as (Eq 4).

$$q = C_{dl}(V_S - V_0).$$
(Eq 4)

Where V_0 is the applied voltage, V_S is the potential at the boundary between the EDL and the bulk, and C_{dl} is the capacitance of the electric double layer. After taking the Fourier transform, the following PDE can be found to solve for the potential at the surface. [7]

$$\sigma \frac{\partial V_S}{\partial n} = i\omega C_{dl}\left(V_S - \frac{V_0}{2}\right)$$
(Eq 5)

Where ω is the operating frequency, and σ is the medium conductivity. However, under higher voltages, and with thicker electrical double layers, the capacitance of the electrical double layer will not be constant, and is instead represented by the following equation, derived by Freise: [8] Compared to the Gouy-Chapman model, this model of the EDL capacitance takes into account the steric effects of the ions. At higher applied voltages, using this model, the EDL charge density plateaus close to the surface, making it more accurate at higher applied voltages.

$$C_{dl} = \frac{\partial q}{\partial V} = \frac{\varepsilon_0 \varepsilon_r}{\lambda} \sqrt{\frac{\sinh(z\Psi_{D\_i})}{\left(1 + 2\upsilon \sinh^2\left(\frac{z\Psi_{D\_i}}{2}\right)\right)\sqrt{\frac{2}{\upsilon}\ln\left(1 + 2\upsilon \sinh^2\left(\frac{z\Psi_{D\_i}}{2}\right)\right)}}}$$
(Eq 6)

Where $\Psi_{D\_i} = \left|\frac{e_0\sqrt{(V_S-V_0)(V_S-V_0)^*}}{k_B T}\right|$, signifying the drop in potential across the EDL, and υ is the effective size of the ions in the EDL. Substituting this capacitance into equation 4 makes for a highly non-linear equation, where an approximate answer can be found through iteration. The proper equation can only be derived by taking the integral of this equation to obtain a relationship between the charge and the potential difference, then substituting that equation into equation 3, and taking the Fourier transform.

2.1.2 - Dielectrophoresis

The dielectrophoretic force (DEP force) is the result of an uneven polarization force acting on a particle as a result of a non-uniform electric field. (Figure 1) This have been well documented in many electrokinetic experiments where particles have shown to move under the influence of dielectrophoresis, starting from the early 1900's, but the first time this phenomena have been properly addressed is by Herbert A. Pohl in 1950. [9]
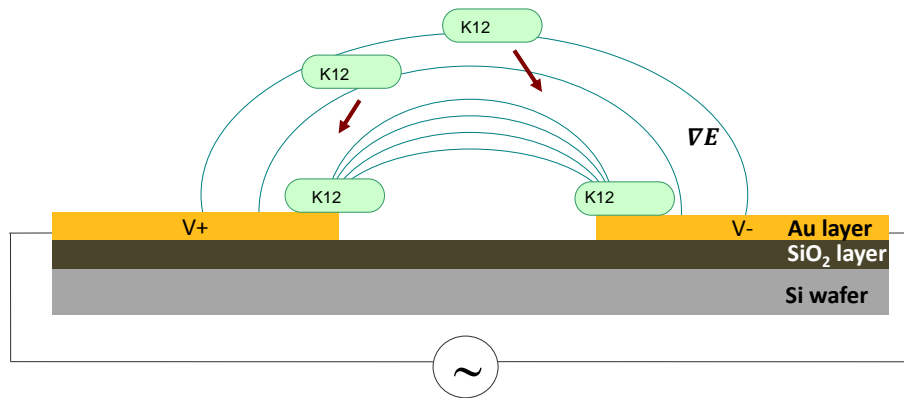
Figure 1: Visualization of the response of E. coli experiencing positive dielectrophoresis. The E. coli is pulled towards the electric field gradient, landing in areas where the electric field is strongest. The arrow indicates the direction of the DEP force on the bacteria.

By 1958, this phenomenon was further investigated and better defined by Pohl. A model was developed by Pohl to explain this matter. The force was described as the product of the dipole moment and the electric field gradient. And for a spherical particle, the equation was simplified to (Eq 7). [10]

$$F_{DEP} = \frac{3}{4}\pi a^3 * \varepsilon_0\varepsilon_r * \text{real}[Ke] * \nabla|E_i|^2 \qquad \text{(Eq 7)}$$

Where 'a' is the particle radius, 'Ke' is the Clausius Mossotti (CM) factor, given by (Eq 8) and 'E' is the electric field in the 'i' direction, where 'i' could be the x, y, or z axis.

From (Eq 7), there are four main factors that affect the dielectrophoretic force on the particle: the geometry/volume of the particle, the dielectric properties of the particle and medium, the frequency of the applied field, and the gradient of the applied field intensity.

The frequency of the applied field determines the activation of certain polarization mechanisms within the particle, and the medium. Within the bacteria, orientation and ionic polarization mechanisms are mainly responsible for the changes in permittivity within the applied frequency range. The effects of the frequency on the DEP force are modeled by the Clausius Mossotti factor (CM factor). (Eq 8)

$$Ke = \frac{(\varepsilon_p - \varepsilon_m)}{\varepsilon_p + 2\varepsilon_m} \qquad \text{(Eq 8)}$$

The Clausius Mossotti factor is a function of the dielectric constant of the particle, as well as the dielectric constant of the medium. Under some conditions where the fluid becomes more polarized than the particle, the particle may experience force facing away from the electric field gradient, or a negative dielectric force. There are many polarization models that can be used to model complex biological particles, but in the context of this thesis, the polarization mechanism for a bacteria cell proposed by Asami *et al.* will be considered. [11]
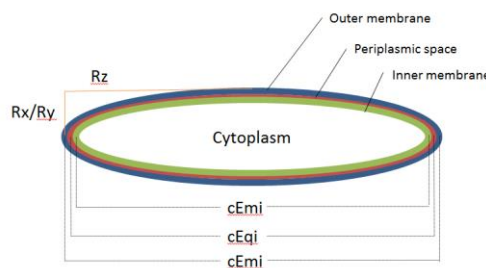
*Figure 2: Model of a cell, by Asami et al., for calculation of the CM factor. R$_i$ symbolises the dimensions of the cell, and cE$_{**}$ symbolises the electric constants of those components. (where ** represents "mi" for membrane, or "qi" for periplasmic space)*

The model assumes the cell is an ellipsoid composed of three membranes encapsulating cytoplasm. [11]

Since the cell membrane shields the inner organelles from electrical effects, the insides do not need to

be modeled. The calculation of the Clausius Mossotti factor of this model is through the equations

derived by Asami *et al.* [3] and Coska *et al.* [4]. The details of the model will be provided in the appendix

(A1). Each of the three membranes have different electrical properties, which are modeled through a set

of parameters derived by Asami *et al*. These parameters are frequency dependent and would have

complex components. An average dielectric property is calculated for each of the three membranes,

then the CM factor is calculated for each geometry. Since the relaxation time of unbound water within

the bulk is around the order of gigahertz, the relative permittivity of water were taken to be a constant

of 81.

The effect of medium conductivity on the dielectrophoretic force has to do with the difference in

electrical properties between the particle and the medium, or more specifically, the Clausius Mossotti

factor. When the conductivity is increased, the CM factor changes from something similar to Debye

relaxation. (Figure 3)
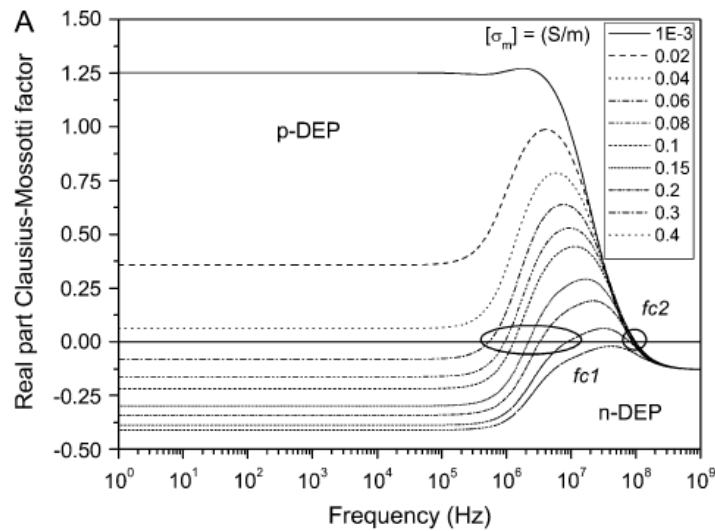
Figure 3: Evolution of the real part of the Clausius-Mossotti factor with changes in the medium conductivity (in S/m^{-1}); fc1 and fc2 refer to the crossover frequencies. [5]

As the frequency continues to increase, the Clausius Mossotti factor will eventually become a constant, due to the deactivation of each of the polarization mechanisms within the cell membrane, leaving only the dielectric properties of the cell cytoplasm and the medium. At roughly 2.5 GHz, the molecular dielectric mechanisms of water starts to deactivate, and the DEP force would then plateau.

The geometry and size of the particle will also play a large role in the influence of dielectrophoresis. For instance, an ellipsoid will have a stronger dielectrophoretic force acting on its length than its width. If the length of the particle is not oriented towards the electric field gradient, this imbalance of forces will induce a torque on the particle. This is the basis of electro-rotation. Due to this phenomenon, it can be assumed the ellipsoid will be oriented towards the field gradient in a stagnant electric field.

Since dielectrophoresis depends on the gradient of the electric field, which itself is dependent on the geometry of the electrodes, the DEP force decays very quickly away from the electrode. With increased frequency, there will be less double layer shielding, resulting in higher DEP forces. This phenomenon will be further reflected in the simulation results below.

2.1.2 - Electroosmotic Flow

As the electrical double layer forms on non-parallel electrodes, the time-averaged electric field passing

through the EDL will no longer be fully perpendicular to the surface. This tangential component of the

field will act on the ionic charge, creating an electroosmotic (EO)

flow (Figure 4)

ACEO Force Profile
ACEO Velocity Profile
Diffuse Layer
Stern Layer
Surface
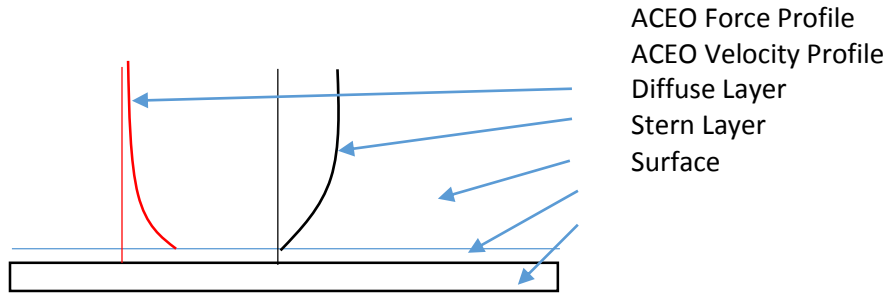
Figure 4: Alternating Current Electroosmosis flow and force profiles

The charges in the electrical double layer of each electrode shield the charges on the electrode, so the

electroosmotic flow will be in the opposite direction of the electrical field. The expression for

electrokinetic flow was derived by Green *et al.* [12] [13] (Eq 9)

$$U_{wall} = \frac{0.5 \cdot \varepsilon_0 \varepsilon_r \cdot \Lambda}{\eta} \cdot \text{Real}[(V_S - V_0) \cdot Conj(-E_t)] \qquad \text{(Eq 9)}$$

Where Λ is the correction factor represented by the percentage of the capacitance provided by stern

layer with respect to the total EDL, E_t is the component of the electrical field tangential to the double

layer, η is the dynamic fluid viscosity, V_S is the potential at the end of the EDL, and V_0 is the applied

voltage.

As a result of the electric field being frequency dependent, the EO velocity is also frequency dependent.

By looking at the timescales of the electrode environment, one can infer the frequency ranges where

electroosmotic flow becomes significant. Since the EDL is modeled as a discontinuous layer, the

electroosmotic flow is typically characterized as a slip velocity occurring on the boundary between the

bulk and the EDL. For the electroosmotic effect to affect fluid above the surface, it would have to be

12

present, or in effect for a certain amount of time for its flow profile to develop. This amount of time is known as the inertial time scale. The inertial time scale for a fluid is defined as L^2/v_f, where L is the characteristic length, and v_f is the fluid viscosity. For example, if the height of the channel was 100 μm, and the kinematic viscosity of the fluid (water) was 10^{-6} m^2/s, then the characteristic time scale would be 0.01 s, or 100 Hz. From the point of view of the time scale of 100 Hz, phenomena occurring at any frequency less than 100 Hz would appear to be discontinuous and periodical. Meanwhile, any phenomena occurring at a frequency higher than 100 Hz would appear to be continuous. Having the slip velocity occur in a relatively periodic manner, at a frequency shorter than the time scale necessary for the momentum to continuously transfer to the bulk, would not result in a significant bulk flow. So, the frequency would need to be larger than 100 kHz for the electroosmotic velocity to be significant.

Similarly, the timescale for the electrical double layer to form is on the order of 0.1 to 100 μs, as calculated by Morrow *et al.* [14], increasing with applied voltage and decreasing with the concentration of the saline solution. This corresponds to a frequency range between 1 MHz and 10 kHz, respectively. For larger voltages on the order of 100 mV, and at more dilute concentrations (0.001 M), the characteristic frequency of the EDL would be around 10 kHz. Past this frequency, there would a rapid drop in electroosmotic velocity.

Both the electroosmotic force and the dielectrophoretic force are dependent on the ionic strength of the solution, represented by the conductivity, or salinity. For electroosmosis, increasing the conductivity of the solution would increase shielding effects of the double layer, thus decreasing the double layer length, and the region which electroosmosis takes place. This is reflected in the characteristic EDL relaxation time. The sensitivity of electroosmosis to the ionic strength is relatively high, with a 6.1 X 10^{-3} M increase in the salt concentration potentially causing an 8-fold decrease in electroosmotic velocity. (Figure 5a)

An increase in the voltage would mainly result in a higher electroosmotic velocity, due to higher electric

fields, but would also shift the relaxation frequency as indicated by Morrow *et al.* This is reflected

experimentally in the studies done by Studer *et al.* [15], and Brown *et al.* [16]. (Figure 5b)

a)   b)
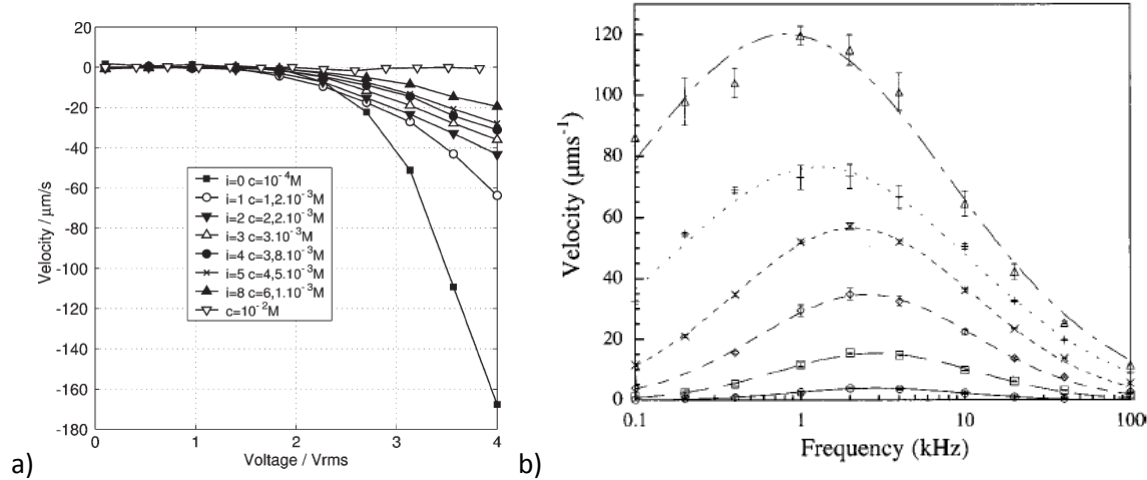
Figure 5: a) Variation of the ACEO pumping speed with the driving signal amplitude for increasing salt concentrations. Driving signal frequency is 50 kHz. It can be seen that velocity magnitude increases with applied voltage, but decreases with increasing ionic strength. Reprinted from Studer et al *[15] b) The scaled fluid velocity plotted against the applied frequency at six different values of the applied potential: 0.2 V_{RMS} (O), 0.4 V_{RMS} (□), 0.6 V_{RMS} (◊), 0.8 V_{RMS} (X), 1.0 V_{RMS} (+), and 1.2 V_{RMS} (Δ). Reprinted from Brown* et al *[16]*

Under high voltages (>1.41Vpp) and in dilute ion concentrations, (~1 mS/m) bulk electroosmotic velocity

at its maximum is on the order of 100 μm/s, and has a maximum value in the 1-10 kHz range. A table of

example ACEO velocities are below: (Table 1)

Table 1: Examples of electroosmotic velocity. twEO stands for traveling wave electroosmosis.

Electroosmotic Velocity	Operation Voltage/Frequency	Conductivity	Electrode Separation	Sampling Point (above electrodes)	Reference
150 μm/s	8 V_{pp} / 1 kHz	10^{-4} M KCl	4.5 μm	Average Velocity	[15]
118 μm/s	3.39 V_{rms} / 1 kHz	10^{-4} M NaNO$_3$	4.5 μm	80 μm	[16]
5 μm/s	4 V_{pp} / 1 kHz	55 μS/cm KCl	250 μm	0.5 μm	[17]
75 μm/s (twEO)	2.5 V_{PP} / 1 kHz	10^{-4} M	10 μm	120 μm	[18]

2.1.3 - Electrothermal Flow

The electric properties of the medium are also temperature-dependent. Thus, an electric field propagating through the medium with temperature gradients will also induce an uneven body force on the medium. This force is known as the electrothermal force, (Eq 11) for which the constants are expressed in (Eq 12) to (Eq 15). The Navier stokes equation (Eq 10) can then be used to solve for fluid flow through the substitution of this force.

$$0 = \nabla \cdot [-pI + \eta(\nabla u + (\nabla u)^T)] + \mathbf{F} \tag{Eq 10}$$

$$F_i = 0.5 * Real\left(A * (\nabla T \cdot E) \cdot E_i + B * |E|^2 * \frac{dT}{di}\right) \tag{Eq 11}$$

$$A = \frac{\sigma \varepsilon_0 \varepsilon_r (\alpha - \beta)}{\sigma + i\omega_0 \varepsilon_0 \varepsilon_r} \tag{Eq 12}$$

$$B = -0.5 * \varepsilon_0 \varepsilon_r * \alpha \tag{Eq 13}$$

$$\alpha = \left(\frac{1}{\varepsilon_r}\right)\left(\frac{\partial \varepsilon_r}{\partial T}\right) \cong -0.00397 \tag{Eq 14}$$

$$\beta = \left(\frac{1}{\sigma}\right)\left(\frac{\partial \sigma}{\partial T}\right) \cong 0.02 \tag{Eq 15}$$

Where 'i' could be the Cartesian coordinates x, y, or z, E is the electric field, T is the temperature, p is the pressure, I is the identity matrix, and ε_r is the relative permittivity of water.

Temperature gradients can be caused through Joule heating. This can be explained as the heat generated from the resistance of the current traveling through the surrounding medium. (Eq 16).

$$-\nabla \cdot (k\nabla T) = \sigma \cdot |E|^2 \tag{Eq 16}$$

Where k is the thermal conductivity. Similarly, this force is dependent on the frequency and the voltage.

The relaxation time of the EDL would vary with the electric field. Points closer to the electrode edge, with a higher electric field, would have a smaller relaxation time, or higher relaxation frequency. Areas with the relaxation frequency smaller than the operating frequency will be relatively unshielded. This is most likely to be areas away from the edge of the electrode. In the case of planar electrodes, where the areas closer to the electrode are shielded while the areas farther away are unshielded, the current will

be passing through areas further away from the surface. And by looking at the distribution in the current density, the behaviour of the ET flow could be predicted.

At higher frequency ranges, the electrodes would be full unshielded, and joule heating will occur mainly at the electrode edges. To maximise ET flow, the frequency would need to be adjusted such that the regions with a high temperature gradient and electric field are maximized. With the electrode shielding regions mainly changing with frequency, the ET flow patterns would not change significantly with voltage.

2.2 – Literature Regarding Electrokinetic Cell Capture

Optimization of cellular capture using electrokinetic forces requires many independent parameters to be taken into account. Generally speaking, the relevant electrokinetic forces can be sorted into two categories: long range forces, and shorter ranged forces. The long range phenomena that affect particle motion typically involve fluid flow. Such examples are electroosmosis, turbulence, and bulk fluid flow. For instance, the electrode designs by Hoettges *et al.* [19] and Melvin *et al.* [20] mainly takes advantage of the electroosmotic force to concentrate and capture cells.

On the other hand, parallel electrodes and interdigitated electrode designs use mainly the dielectrophoretic force for cell capture. Although the dielectrophoretic force has a shorter range, the DEP force can be made many orders of magnitude stronger than the long reaching forces such as electroosmosis, due its dependence on the electric field gradient. Furthermore, the DEP force can be tuned to be more selective towards particles of a certain dielectric property, as shown by Cheng *et al.* [21] [22], and Castellarnau *et al.* [23].

The fluid is typically used to concentrate bacteria and cells into an area on the order of 1000 μm^2, where the DEP force would then be responsible for further concentration and retention within this region. By tuning operation conditions, certain mechanisms can be made more or less significant to optimise bacteria capture.

Table 2: Summary of literature involving electrokinetic bacteria concentration

Author	Electrode Shape	Description	Performance	Source
T.P. Hunt, R.M. Westervelt	3D tweezers-shaped	-Tweezers-like pair of electrodes to focus electric field at a single point to manipulate single cells	-Captures single cells	[24]
M.R. Tomkins *et al.*	2-D quadrupolar electrodes	-Induces DEP and EO forces to concentrate bioparticles from the bulk to the space between the electrodes	-Noticeable concentration of viruses at 10^9 pfu/mL	[25]
Silicon Biosystems	Array of proprietary DEP capture wells	-Cells are captured in the DEP wells, and by turning certain elements of the array on and off, selected cells are moved to a capture zone and eluted.	-Capable of eluting very high purity cell suspensions	[26] [27]
S. Menad *et al.*	Array of 2D square electrodes, offset from each other	-Negative DEP used to concentrate cells in the space between electrodes	-Cells in suspension captured onto electrode surface. Tissue formation was present	[28]
C.F. Chou *et al.*	2D parallel electrodes with triangular walls in between electrodes to focus electric field. (electrodeless DEP)	-the field gradient was created by using triangular dielectric walls to focus the field to a point between the electrodes.	-walls focus the field captured cells at the focused point.	[29]
K.F. Hoettges	2D Electrodes with intersecting	-In addition to the DEP force between the	-Bacteria found to be between the	[19]

et al.	circular nodes like a zipper	electrodes, the electroosmotic force also concentrated bacteria to the centre of the nodes.	electrodes but mainly captured in the centre of the electrodes, as that had the greatest capture area.	
N. Gadish *et al.*	2D Interdigitated electrodes	Ridges on the channel roof induced turbulent flow, while the floor of the channel contained interdigitated electrodes.	Turbulent flow allowed more cells to be captured through DEP, compared to laminar flow.	[30]
M.D. Pysher *et al.*	2-D parallel electrodes with a series of sharp walls between electrodes to focus electric field. (electrodeless DEP)	The field gradient was created by using a series of triangular walls to focus the field to a point between the electrodes.	-varying walls focus the field to different degrees captured cells with different sizes and dielectric properties.	[31]
L. Yang	Interdigitated Electrodes	DEP force from interdigitated electrodes concentrated cells	Collection with DEP was better than through adsorption alone.	[32]
N. Swami *et al.*	2-D parallel electrodes with sharp walls along with a circular grounded electrode in between electrodes to focus electric field.	Used a combination of wall geometry and a small grounded electrode in the centre of the field to focus the electric field to manipulate DNA	DNA hybridization was found to occur at a greater rate in the regions of high electric field concentration.	[33]
Cheng *et al.*	parallel electrodes printed on the roof and floor of	A flow is induced through a microchannel created by compressing two glass plates. Electrodes	Electrodes successfully used to trap bacteria and DNA functionalized beads.	[21] [22]

	microchannel such that the electric field would run across the across the channel, forming walls	printed on both glass plates create DEP 'walls' which frequency and voltage can be adjusted to influence various particles differently.	For DNA matching, flowrate was then adjusted such that only perfectly matched DNA would be attached to the trapped beads.	
E.M. Melvin *et al.*	2-D linear electrodes, with one thicker than the other, arranged in a square-shaped spiral.	Inequivalent electrodes lead to an EO pumping effect. This effect was used to concentrate particles into a single area.	Cells were concentrated into the center of the square-shaped spiral. Some cells were captured on the electrodes, due to the DEP effect.	[20]
D. Cai *et al.*	Planar electrode with insulated areas to focus electric field (iDEP)	iDEP was used to capture cells, after which the entire electrode was moved to a separate chamber along with cells to perform PCR	With the help of iDEP for cell capture, identification of separate species was limited to 3 hours.	[34]
Schäfer *et al.*	Parallel planar electrodes on the roof and floor of the microchannel. But the floor contains nano-tips to focus the DEP force	Under smaller voltages, the nano-tips creates a DEP force, acting as a kind of tape to trap the bacteria	Bacteria were trapped, as expected, to the areas containing the nano-tips	[35]

When working with biological cells, properties such as cell viability must be taken into account. The viability of cells affects dielectric properties to such a degree that DEP have been used to sort live and dead cells. [36] And high voltages are known to be lethal to cells, as they perforate the cell membrane. This technique, in moderation, is known as electroporation, and is used to make the cells more susceptible to certain drugs, or genetic manipulation. A study was done by LaLonde *et al.*, finding that decreases in cell viability only become noticeable at 300 volts and extended exposure times of roughly 1 minute. Furthermore, the shape of electrodes also has an effect in that sharper electrodes, producing denser electric fields, will decrease cell viability with the same operating conditions. [37]

When working with sub-micron particles such as viruses and DNA, the DEP force is significantly reduced due to the size of the particles. Thus, the fluid motion would then be more important in these applications, and must be scaled down accordingly to avoid overwhelming the DEP force.

2.3 – Raman Spectroscopy Literature Review

Concentration of biological cells and particles through electrokinetic phenomena can be used in conjuncture with a variety of detection techniques, including immunoassays and DNA hybridization. However, these techniques require labeled antibodies or DNA, which are expensive and difficult to manufacture. [38] One label-free method proven to accurately identify cells is through Raman Spectroscopy.

Like other spectroscopic techniques, Raman spectroscopy is based on measuring the intensity of the inelastically scattered light from a sample. When electromagnetic radiation hits a molecule, some of the radiation is scattered through Rayleigh scattering, where the wavelength of the scattered light remains the same (elastic scattering). However, through what is known as the Raman effect, some of the light is inelastically scattered. This scattered light is shifted to typically a larger wavelength than the incident light, and is detected by a spectrometer. The output would then be the intensity of the shifted light at a wavelength relative to the incident light with the unit of cm^{-1}. [39] Raman spectroscopy is a non-destructive technique which has the major advantage of being able to acquire spectra inside water-based media. It is also able to focus on samples with microscopic dimensions, making it a label free method for detecting and identifying bacteria. However, within the scope of this thesis, Raman spectroscopy will only be used for detection.

After acquisition, the spectrum of a sample could be analysed manually by identifying peaks, or through a spectra sorting technique known as principle component analysis (PCA). The signal at each wavelength shift in the processed spectrum is considered to be one variable. The principle component would then be a weighted linear combination of each variable. This would be equivalent to having a plot of N dimensions, with N being the number of wavelengths measured, and each point on the plot would be

equal to each acquired spectrum. The principle component would then be the lines of best fit through

cloud of points, through all N dimensions, with all of them orthogonal to each other.

A summary of studies using Raman spectroscopy to detect and identify bacteria have been tabulated

below. (Table 3) Some of these methods include electrokinetic manipulation as a form of pre-

concentration, and others include analysis techniques such as PCA.

Table 3: Summary of literature involving Raman spectroscopy for bacterial detection

Author	Pre Concentration Method	Raman Spectra Type	Sorting Method	Procedural Description	Results	Ref.
Naja *et al.*	N/A	SERS (Ag NP)	N/A	-Ag NP Deposited onto surface. Layer of proteins and antibodies used to attach specific bacteria	-Detection of single bacteria via SERS was possible	[40]
Hou *et al.*	Vortex Concentration via ACEO using a needle	SERS (Ag NP)	N/A	-Vortex induced in bulk, causing cells to concentrate in stagnant area, after which IR Raman was possible	-Bacteria Detection down to 10^4 CFU/mL	[41]
Cheng *et al.*	Cells concentrated with 'dielectrophoretic walls' in a microfluidic channel	SERS (roughened Au surface)	N/A	-As an offshoot of their previous works, cells were concentrated via dielectrophoretic walls induced across the height of the channel, with a roughened gold surface deposited on the ceiling above the area where cells are expected to be collected	-Chip proven to both separate and collect cells for analysis	[42]
Sengupta *et al.*	N/A	SERS (Ag NP)	N.A	-A study on the detection limits of SERS by varying the concentration of *E. coli* in suspension	-Detection limit found to be (10^3 CFU/mL)	[43]
Schröder *et al.*	Centrifugation, followed by	N/A	N/A	-Using centrifugation followed by DEP to concentrate cells for analysis via IR Raman	-*E. coli* was detected in urine samples of $>10^5$	[44]

				Spectroscopy	CFU/mL	
	Dielectrophoresis via quadrupolar electrodes printed on a chip					
Schultz et al.	Drying the bacteria suspension	Micro-Raman spectroscopy	PCA, Confusion Matrix	-Spectrums of various bacteria were compared using statistical methods to see how much they vary.	-It was possible to identify different strains of bacteria via Raman spectroscopy with at least an 88% certainty.	[45]
Huang et al.	N/A	Micro-Raman Spectroscopy	PCA, DFA, HCA	-Various sections of the spectra were analysed and compared to each other via MVS methods to not only determine species, but also C^{13} adsorption.	-A correlation was found between C^{13} adsorption and band shifts. -It was also possible to identify different strains.	[46]
Stöckel et al.	N/A	Micro-Raman spectroscopy	PCA, LDA, SVM	-Spectra of bacterial spores were taken and compared to each other	-Anthrax strain was determined with at least 96% accuracy	[47]
Strola et al.	N/A	Raman Spectroscopy	PCA, Confusion	-Bacteria suspension was diluted to a standard optical density, then the Raman spectra was taken	-Growth phases were shown to be	[48]

		of bulk Solution	matrix	at different times, signifying various growth phases	distinguishable through Raman with an accuracy of 42-79%.	
Stöckel *et al.*	Drying	Raman Spectroscopy of dried sample	LDA, SVM	-Cells were cultured in milk, then dried before Raman spectra was taken.	-Bacteria were identified in milk with at least a 94% sensitivity	[49]
Zhou *et al.*	N/A	SERS via Ag deposition onto cells	HCA	-Instead of binding Ag nanoparticle to the cells, silver ions were reduced to form nanoparticles directly on the cell surface.	-SEM shows successful deposition of Ag NP onto cells. -Detection limits decreased to 10^3 CFU/mL	[50]

The sensitivity of using Raman spectroscopy for bacteria detection can be enhanced using gold or silver

nanoparticles in a technique called surface enhanced Raman spectroscopy (SERS). There are two

theories which address the surface enhancement aspect of SERS: the electromagnetic theory, where

surface plasmons are excited, and resonate with the molecules which come into contact with the

surface, and the chemical theory, where new bonds are formed between the surface and the analyte,

creating new electron levels which have an enhanced Raman effect. [51]

As SERS works on the principle where only the outermost surfaces of the cell are affected, certain peaks

pertaining to the Raman spectrum of *E. coli* will be amplified. Comparing the works of various

researchers, the Raman spectrum of *E. coli* has the following characteristic peaks:

Table 4: Location of significant peaks in a Raman spectra of E.coli. Peaks in bold are amplified through SERS, summarized from the study by Schultz et al. [45]. Amplified peaks derived from Sengupta et al. [43]. Chemical groups derived from Strola et al. [52].

Raman Shift (cm^{-1})	Relative Intensity	Chemical Group
781	**Medium**	**Cytosine, Uracil**
1001	Medium	Phenylalanine
1170	**Weak**	**C-C, C-O, C-N, C-O-H**
1242	**Medium**	**C-C skel, C-O-C Stretching**
1338	**Strong**	**C-H Deflection**
1445	**Medium**	**CH$_2$ scissoring**
1573	Mid	Guanine, Adenine, Amide II
1605	Mid	Phenylalanine
1655	**Mid**	**Amide I**
2925	Strong, Broad	C-H Stretching

The outer cell wall of *E. coli* is lipopolysaccharide's, composing of phosphates, sugars, and lipids. As such,

the peaks ranging from a shift of 1200 to 1450 cm^{-1}, representing C-O-C stretching, and C-H stretching

are amplified. Underneath the outer cell wall, is an inner cell membrane composed of peptidoglycan, a polymer composed of sugar and amino acids. As such, peaks at 781 cm^{-1} and 1655 cm^{-1} are also amplified, but to a lesser extent, due to nano-particles being known to penetrate cell membranes.

However, the problem with SERS is that it is often cited as being difficult to reproduce. The nanoparticles which provide the SERS effect also affect other molecules or particles in the solution. Since SERS effect is known to amplify signals up to 10^{10} times, signals due to contamination will also be amplified, necessitating a relatively pure bacteria sample for a clean, reproducible signal. As such, researchers such as Schultz *et al.* chose not to use Raman in their studies despite working with concentrations down to 10^4 CFU/mL. [45] Thus, it is especially important to include a reliable pre-sorting step in SERS applications, as Cheng *et al.* have done. [42]

3.0 Experimental Overview

The capture effectiveness of a quadrupolar electrode setup was tested by running trials while varying the bacterial concentration, and with various functionalized surfaces. Detection was then performed with Raman spectroscopy. (Figure 6) The microchips used were of the same design as the one used by M.R. Tomkins and J. Wood. [53] Schematics of the electrodes are include further on. (Figure 12) The microelectrodes were manufactured thorough first masking with photoresist, then has gold deposited on its surface through electron beam evaporation, as documented by Shiva Golchi. [54]

Clean Chip	Functionalize Chip Surface	Bacteria Capture	Qualitative Observation and Raman Spectroscopy
(3.1 Chip Cleaning)	(3.2 Chip Functionalization)	(3.4 Bacterial Capture)	(3.5 Observation and Raman Spectroscopy)

Prepare Cell Suspension	Count Bacteria	Dilute to Desired Concentration
(3.3 Preparing a Cell Suspension from Culture)	(3.3 Preparing a Cell Suspension from Culture)	(3.3 Preparing a Cell Suspension from Culture)

Figure 6: Experimental Flow Diagram

The chip was first cleaned, and functionalized if needed. The cell suspension was prepared from cultures just prior to the experiments. To perform the capture, a droplet of the bacterial suspension was placed onto the electrodes, while a signal generated provided an AC voltage of 12 Vpp, at 10 kHz. The electrodes were set up under a microscope, so as to periodically observe the capture process for electrode damage. After capture, the samples were quickly rinsed with DI water, or were washed with 0.1M phosphate buffer solution in a shaker, then dried with nitrogen. Observations were made quantitatively, and by using Raman spectroscopy.

3.1 Chip Cleaning

The procedure is summarized in a flowchart below in Figure 7.

The water used in the experiments were deionized, then passed through a 0.45 μm filter by Millipore®.

The final conductivity was measured to be 4.4 μS/cm.

The chips were was cleaned by first washing the chip sequentially with water, ethanol, acetone, then

water, without allowing any of the previous solvent to dry to avoid residue formation. After the final

solvent wash with water, the chips were was dried with high-purity nitrogen.
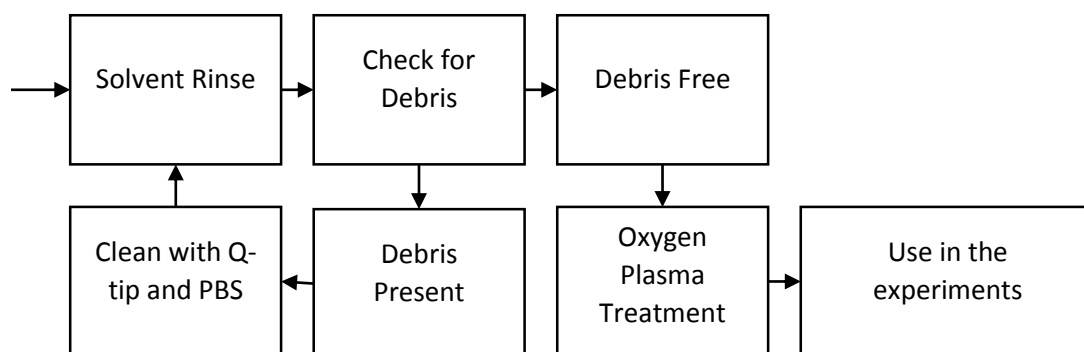
Figure 7: Flow diagram of chip cleaning procedure.

After solvent cleaning, the microchips were inspected under 1000X magnification to check for debris, or

whole bacteria that might not have been removed through solvent rinse. Bacteria produce adhesins and

other chemical factors that facilitate their adhesion to surfaces. This makes them particularly hard to

remove, requiring mechanical and/or chemical means. Leftover bacteria were removed by dragging a Q-

tip dipped in 0.1 M phosphate buffer solution over the microelectrode surface.

After mechanical cleaning, the chips were quickly rinsed again with multiple solvents. If the chip was

observed to not be damaged, and free of debris, it was put through oxygen plasma treatment for 30

minutes. Oxygen plasma treatment creates free radicals and unstable functional groups on the surface,

leading to a more polar surface, which may adversely affect surface functionalization and bacteria capture. Thus, the chips were left for at least 8 hours in air to equilibrate prior to use in the experiments.

3.2 Chip Functionalization

The functionalization setup is a Petri dish filled 1/3 full with water, with a microscope slide propped up above the water surface. A droplet containing a concentrated solution of the molecule was placed on top of the chip. The drying of the antibody solution would result in a coffee right effect where the majority of the antibody would be deposited on the outer edges of the droplet. To prevent the droplet from drying during functionalization, the petri dish is sealed with parafilm.

Prior to any functionalization, the chip was UV-ozone treated for 1 hour, then immediately immersed in DI water for 20 minutes. After drying, 25 µL of a 5 mg / µL Biotin-BSA in phosphate buffer solution was placed on top of the chip inside the functionalization setup, then left overnight.

Afterwards, each chip was rinsed quickly with phosphate buffer solution, then placed inside a petri dish filled with 1/3 full of phosphate buffer solution. The dish was then placed onto a shaker for 15 minutes. The chip was then taken out, washed with water, dried with nitrogen, and then placed onto the functionalization setup. Avidin stock solution was diluted to 2.5 mg/mL, then 25 µL was placed onto the chips. It was then left to functionalize for 2 hours.

The chip was rinsed with water, dried with nitrogen, and then functionalized with 25 µL of biotin conjugated antibody. The concentration for which is 4 mg/mL. The functionalization of the antibody should be for at least 3 hours before use. The chip was rinsed with water, and dried with nitrogen before use.

A schematic of the functionalization scheme is shown in (Figure 8).
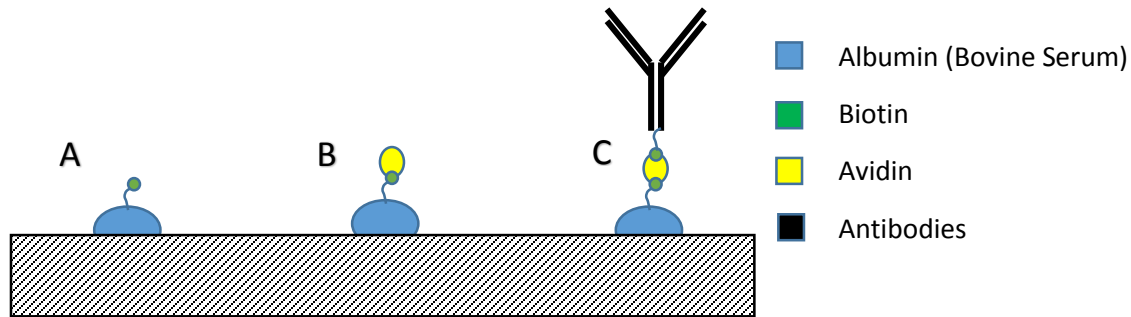
Figure 8: Bovine serum albumin attached to a biotin molecule was first adsorbed onto the surface. (A) Avidin was then added. (B) Finally, biotin conjugated antibodies were added.

3.3 Preparing a Cell Suspension from Culture

The bacteria species used were transferred from a culture grown on Petri dishes to a centrifuge vial filled with 500 µL of water. The suspension was agitated with a pipette, then vortexed to evenly suspend the bacteria.

After suspension, the bacteria were washed by first centrifuging from the suspension for 10 minutes at $5.8X10^3$ G. The supernatant was removed, new water was added up to the 500 µL mark and the bacteria were suspended using the previously mentioned methods. This procedure was repeated twice.

The bacteria were serially diluted 100 fold such that counting was possible. 60 µL of the bacteria suspension was then pipetted into a Petroff-Hausser counter and the concentration of bacteria was determined. The bacteria were then serially diluted to the desired concentrations for capture (10^6-10^3 CFU/mL)

3.4 Bacterial Capture

An AC voltage was applied to the electrodes using a signal generator for 15 minutes. (Figure 9) The chip was connected to the signal generator through a custom set-up where conducting clamps held the chip

down. 50 μL of the cell suspension was deposited on the microelectrode centre, beading into a drop

balanced on top of the chip. The droplet was deposited in the center of the chip. During capture,

microelectrode tips were observed through a 10X objective lens to ensure no electrode damage or

bubble generation was present.
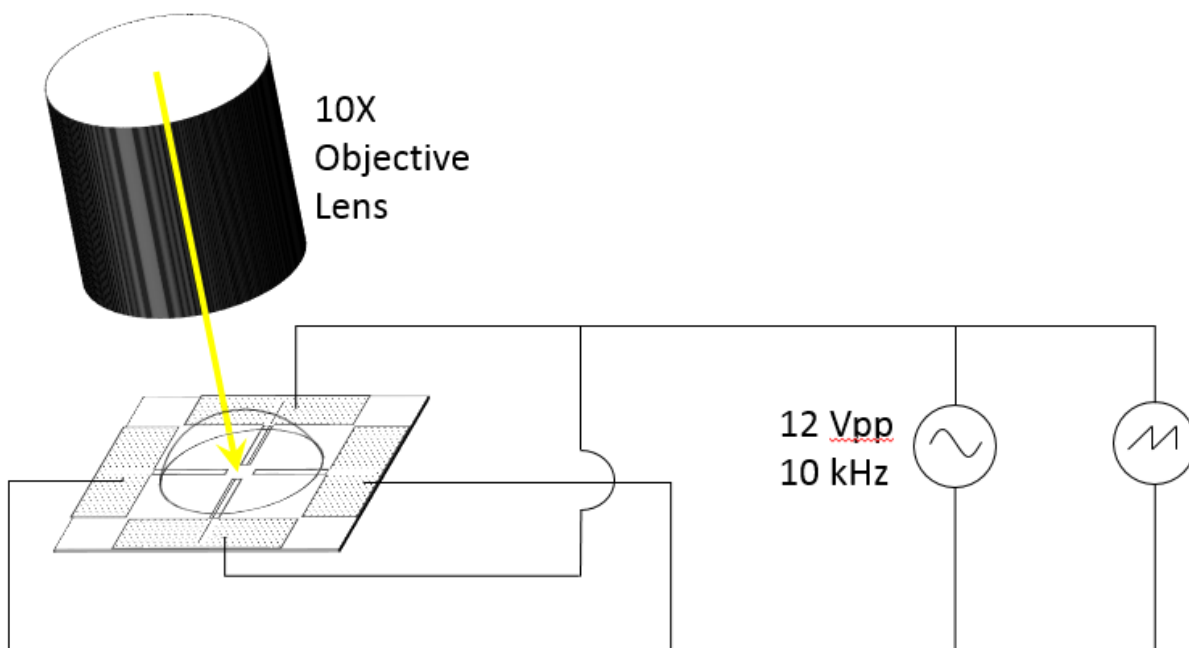
Figure 9: Bacteria capture electrode setup. Bacteria capture was monitored through a visual light microscope at 10 times magnification, and through an oscilloscope, which was connected in parallel to a signal generator.

After capture, the chip was quickly rinsed with water, then dried with nitrogen. The chip was observed

using a visual light microscope under 1000X magnification, after which the Raman spectrum was taken.

3.5 Observation and Raman Spectroscopy

The system used was a LabRAM Jobin-Yvon/Horiba micro-Raman spectrometer with a 632 nm He/Ne

laser of 17 mW with an 1800gr/mm grating and an Olympus BX41 microscope system. Spectra collection

was performed with the following settings: X100 microscope objective, 500 μm pinhole, 500 μm slit

width, and 60 s exposure time. Focus of the Raman laser was obtained by repeatedly taking the spectra of the silica substrate and refocusing such that the silica peak at 1000 cm^{-1} was maximized.

The Raman spectra were acquired at 12 different points, then averaged before correction for baseline and noise. These points are located along the line of least separation between the electrode tips. One point is located at the midpoint of each line, and two at either end. While bacteria would mainly collect at the edges of the electrode, the point in the center between the electrodes was chosen to allow for the averaged signal to be a function of the concentration. For if there is a lot of collection, the spectrum taken in between the electrodes would add to signal intensity.
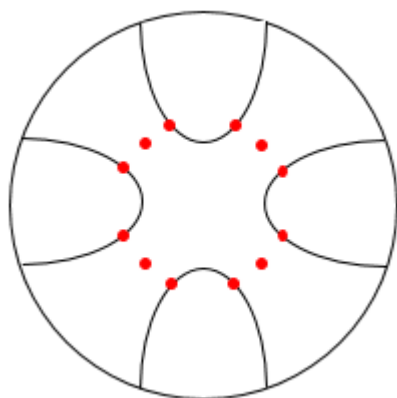
Figure 10: Points where the Raman spectra were taken. One point is located at the midpoint of the line of minimum separation between the electrode tips, and two at either end of the line.

3.6 Simulations

The simulations of electrokinetic phenomena involved in bacteria capture were conducted in COMSOL Multiphysics®, version 3.5. There are three main phenomena that affect the motion of bacteria. ACEO and ET forces affect the motion of the fluid, while DEP is a force which directly affects the bacteria. The electrode design contains four planes of symmetry, two of which bisects the electrodes and intersects at the center of the chip. So, it is expected that at each of the quadrants, the flow will be identical, and reflected along the planes of symmetry. Thus, only one quadrant of the electrode chip was simulated.

Furthermore, the assumption was made that the fluid flow will be steady state, and with a very dilute suspension of bacteria. So, distortions of the electric field due to the presence of bacteria was considered to be negligible.

3.6.1 Mesh and Model Design

The mesh density is highest around the electrode tips and edges, and increases exponentially towards those points. The mesh density at the tips of the electrodes is roughly 450450 elements / mm, while the mesh density at the outer edge is approximately 4.93 elements / mm. (Figure 11) The model was meshed in this way because previous simulations with a courser mesh indicated that the most significant effects of the electrokinetic phenomena originated from the electrode junction.
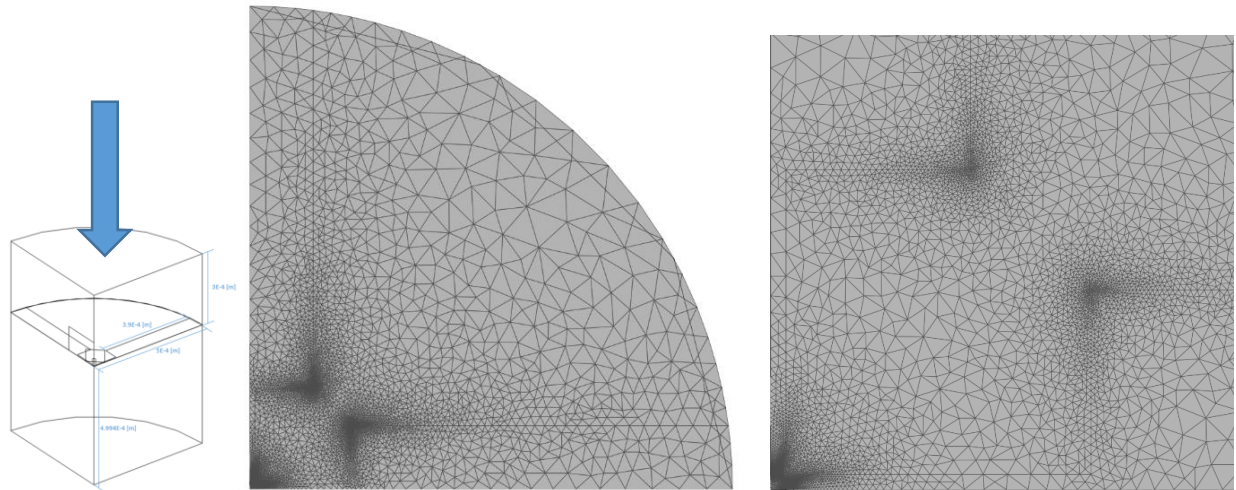
Figure 11: Pictures of the mesh density on the plane containing the electrode surface. When zoomed in, it can be seen that the mesh density around the electrode tips points increase exponentially.

Schematics of the model design are shown below. The droplet is modeled up to 0.3 mm above the

electrodes, while the silicon is model down to a depth of 0.5 mm. The total width of the model was

made to a length of 0.5 mm.
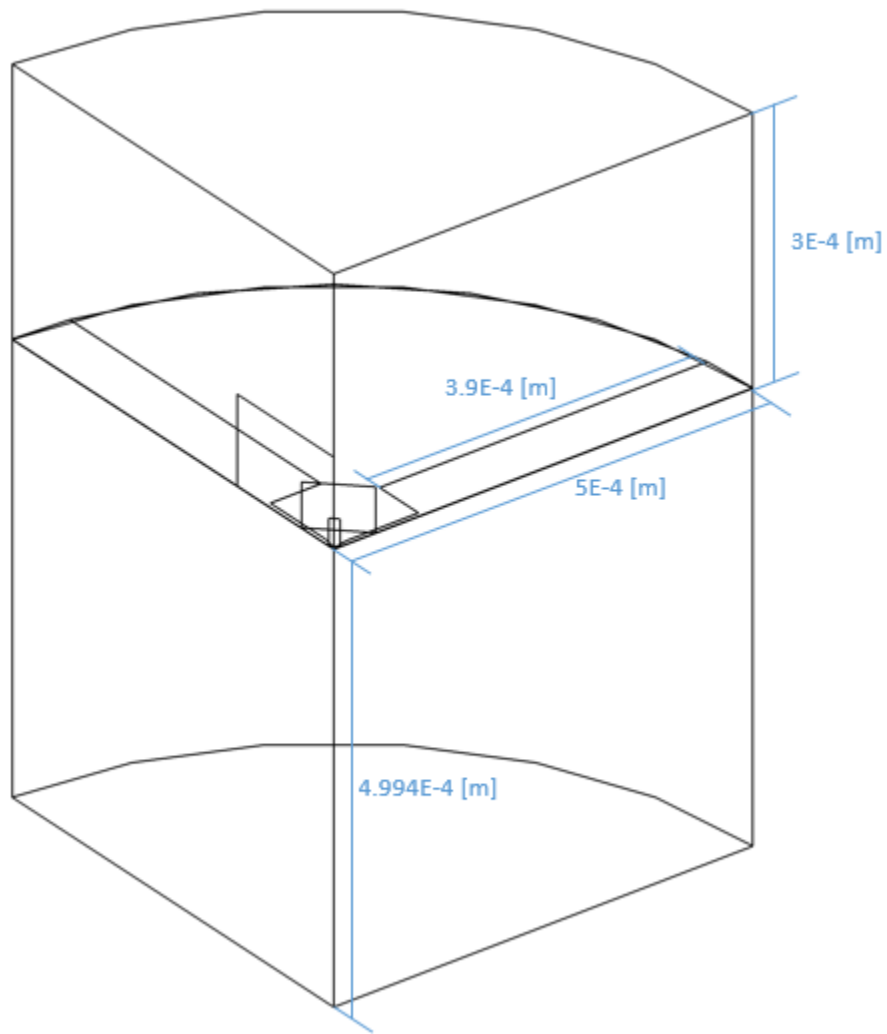
Figure 12: Bulk dimensions of the model.
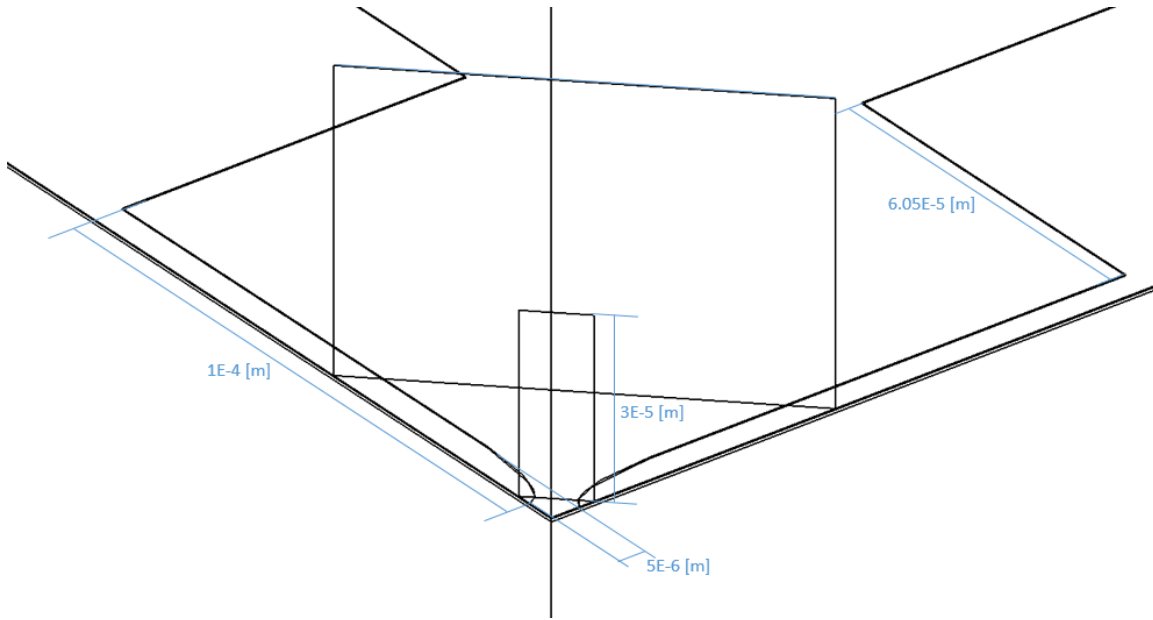
Figure 13: Zoomed in electrode tip dimensions
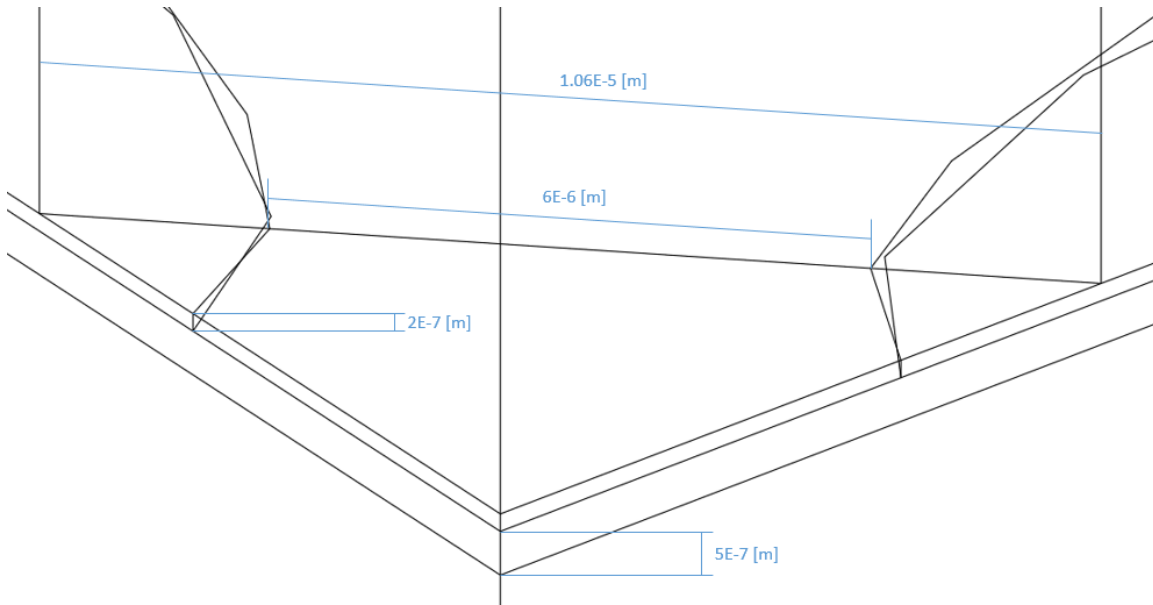
Figure 14: Electrode tip dimensions

3.6.2 Electric Field Calculations

The electric field for our system originates from one electrode, propagating through the medium, represented by the Laplace equation, (Eq 17) and terminating at the other electrode. All other outer boundaries except the electrodes were set as symmetry boundaries. (Eq 18) The insulating silica layer and the silicon layer were set as continuous boundaries, but with a different permittivity.

$$\nabla \cdot (-\varepsilon_0 \varepsilon_r \cdot \nabla V) = 0 \qquad \text{(Eq 17)}$$

$$n \cdot (-\varepsilon_0 \varepsilon_r \cdot \nabla V) = 0 \qquad \text{(Eq 18)}$$

Where, V is the potential at any given point in the model.

The EDL was modeled as an infinitesimally thin layer on top of the electrode, where the boundary condition on the electrode was made to be the potential between the EDL and the bulk. This was calculated by first looking at the charge balance within the electrical double layer. [7] Where Φ is the potential at the surface, equivalent to V. (Eq 19)

$$\sigma \frac{\partial \Phi}{\partial n} = \frac{\partial q}{\partial t} \qquad \text{(Eq 19)}$$

If the electric double layer is very thin and at low applied voltages, we can assume that there is a linear correlation between the charge and the drop within the electrical double layer, then we can say the charge can be expressed as follows: where V in this case is the applied voltage.

$$q = C(\Phi - V) \qquad \text{(Eq 20)}$$

Where C is the capacitance of the EDL, Φ is the potential at the end of the EDL, and V is the surface potential. These values, as periodic functions of time, are expressed below:

$$\Phi = \Phi_0 e^{i\omega t} e^{i\theta} \qquad \text{(Eq 21)}$$

$$V = \frac{V_0}{2} e^{i\omega t} \qquad \text{(Eq 22)}$$

Where, θ is the phase shift. The applied voltage is seen as the reference where the phase shift is zero.

Combining (Eq 19) to (Eq 22), we obtain the following:

$$\sigma \frac{\partial \Phi_0}{\partial n} e^{i\omega t} e^{i\theta} = C \frac{\partial}{\partial t} \left(\Phi_0 e^{i\omega t} e^{i\theta} - \frac{V_0}{2} e^{i\omega t} \right) \tag{Eq 23}$$

Then, taking the Fourier transform of both sides, we end up with

$$\sigma \frac{\partial \Phi_0}{\partial n} e^{-i\theta} = i\omega C \left(\Phi_0 e^{-i\theta} - \frac{V_0}{2} \right) \tag{Eq 24}$$

Where $\Phi_0 e^{-i\theta}$ is the complex conjugate of the potential at the edge of the electrical double layer (EDL) at time zero. So, the equation can also be written as:

$$\sigma \frac{\partial \Phi^*}{\partial n} \Big|_{t=0} = i\omega C \left(\Phi^*|_{t=0} - \frac{V_0}{2} \right) \tag{Eq 25}$$

Further calculations typically rely on the magnitude of the potential, so in practical calculations, using either the potential or its conjugate would yield no difference.

However, at higher voltages and conductivities, we cannot assume that there is a linear correlation between charge and voltage. Instead, this correlation will be (Eq 26).

$$C_{dlv\_i} = \frac{\varepsilon_0 \varepsilon_r}{\lambda} \sqrt{\frac{\sinh(z\Psi_{D\_i})}{\left(1 + 2v \sinh^2\left(\frac{z\Psi_{D\_i}}{2}\right)\right) \sqrt{\frac{2}{v} \ln\left(1 + 2v \, sinh^2\left(\frac{z\Psi_{D\_i}}{2}\right)\right)}}} \tag{Eq 26}$$

Where v is the non-zero fraction volume of the ions, and is typically used as a correction factor. Ψ_{D_i} is represented by the following:

$$\Psi_{D\_i} = \left| \frac{e_0 \sqrt{(\Phi_i - V_E)(\Phi_i - V_E)^*}}{k_B T} \right| \tag{Eq 27}$$

Where e_0 is the electron charge, and V_E is the applied voltage on the electrode.

Keeping the infinitesimally thin double layer assumption, this new correlation was applied. But with this equation being highly non-linear, the solver wasn't able to converge to a solution due to a lack of

memory. Thus, a manually iterative process was used where the C calculated in one iteration was used to solve for the voltage in the next iteration. The flow diagram would be as follows:
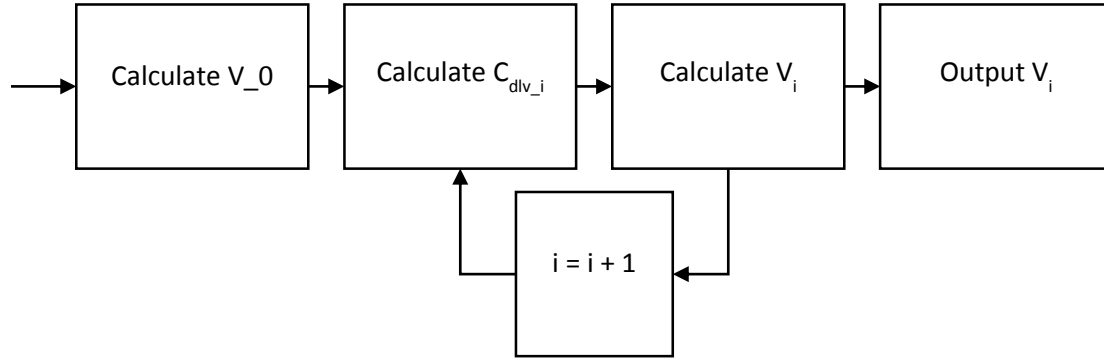
From previous simulations, the fluid velocities calculated would have a range with a difference of 5 orders of magnitude. Since the main area of focus would be on the tips of the electrodes, and most phenomena was dependent on the electric field, the convergence criteria was set to be a difference of 0.001% between iterations for the average electric field over the electrode tips. This was found to have been obtained within 11 iterations.

3.6.3 Calculations for the Dielectrophoretic Force

Each component of the dielectric force is calculated separately, through the following equations. (Eq 28) (Eq 29)(Eq 30).

$$F_{DEPx} = \pi\, r_x^2 r_z\, \varepsilon_r \varepsilon_0 \text{Re}[CM]_x \frac{d|E|^2}{dx} \qquad \text{(Eq 28)}$$

$$F_{DEPy} = \pi\, r_x^2 r_z\, \varepsilon_r \varepsilon_0 \text{Re}[CM]_x \frac{d|E|^2}{dy} \qquad \text{(Eq 29)}$$

$$F_{DEPz} = \pi\, r_x^2 r_z\, \varepsilon_r \varepsilon_0 \text{Re}[CM]_z \frac{d|E|^2}{dz} \qquad \text{(Eq 30)}$$

Each component of the gradient of the squared magnitude of the electric field was calculated through (Eq 31).

$$\frac{d|E|^2}{di} = \frac{d}{di}[(E_x)(E_x)^* + (E_y)(E_y)^* + (E_z)(E_z)^*] \qquad \text{(Eq 31)}$$

Where 'i' could be in the x, y, or z direction. Because the electric field intensity is expressed as an imaginary number, the components were multiplied by the complex conjugate of themselves, rather than squared.

The Clausius Mossotti factor (CM factor) was calculated using the model provided by Asami *et al*. [11] The prescribed constants used were described in the paper. At a conductivity of 1 mS/m, for an ellipsoidal *E.coli* cell, the calculated Clausius Mossotti factor does not change significantly from a range of 100 Hz to 1 MHz, which is the range of frequencies that capture is observed.
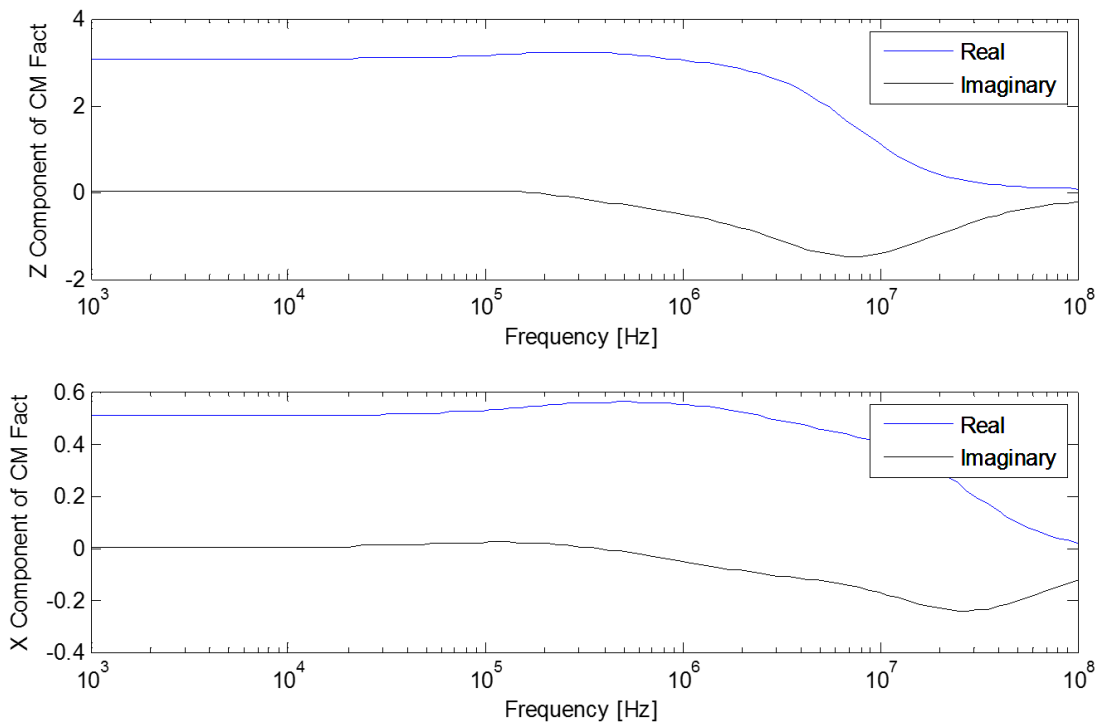
Figure 15: Graph of the Clausius Mossotti factor along the x and z axis of an E. coli cell, using the model developed by Asami et al. For these graphs, the real component would always be larger than the imaginary component.

So that the DEP force is comparable with fluid flow velocties resulting from electroosmotic flow and electrothermal flow, the DEP forces is translated into a terminal velocity. Within a viscous fluid the DEP force will be balanced out by the drag force, or stokes force, resulting in a constant velocity relative to

the fluid. This velocity can be found by utilizing the friction factor of the particle. (Eq 32) This friction

factor was assumed to be the same as a randomly moving ellipsoid. (Eq 33) [55]

$$F_{dep} = F_{stokes} = f * U_{dep} \qquad \text{(Eq 32)}$$

$$f[kg/s] = \frac{6\pi\eta R_y}{\log\left(\frac{2R_y}{R_z}\right)} \qquad \text{(Eq 33)}$$

Then, the overall velocity of the particle would be the sum of the fluid velocity plus the terminal velocity,

within certain limits that will be discussed in section 3.3.6.

3.6.4 Electroosmotic Flow Calculations

The electroosmotic force is calculated through the Navier Stokes equation with the assumptions of a

Newtonian fluid and viscous flow. The system under observation is a volume within the microfluidic

droplet 300 μm in height. Velocities within this volume should not exceed 500 um/s, [56] [16] with a

total average velocity of 0. With generous assumptions, the Reynolds number in this system should then

be on the order of magnitude of 10^{-6}, which is well in the region of laminar or viscous flow. The equation

used by COMSOL is:

$$0 = \nabla \cdot [-p\mathbf{I} + \eta(\nabla\mathbf{u} + (\nabla\mathbf{u})^T)] + \mathbf{F} \qquad \text{(Eq 34)}$$

Where **F** is the force vector, and set equal to zero.

In the case of AC electroosmosis, there is no force term describing fluid motion in the bulk, but instead

there is a slip velocity modeled as a boundary condition. In the simulation, with each component of the

slip velocity is calculated separately. [13]

$$u_{wall\_i} = \frac{\varepsilon_0\varepsilon_r}{2\eta}\Lambda * \mathrm{Re}[(V - V_E)(E_i)^*] \qquad \text{(Eq 35)}$$

Where 'i' stands for either the x, y, or z direction, and Λ is a correction factor, introduced by Bazant *et al*.

[57] Other than the electrodes, silicon surfaces were described as having no-slip conditions, and

symmetry and open boundaries were described accordingly.

3.6.5 Electrothermal Flow Calculations

The governing method of heat transfer is determined through the Peclet number, given by (Eq 36). The Peclet number is a dimensionless number describing whether heat transfer with a fluid will be dictated by conduction or advection. For numbers larger than 1, heat transfer will be governed by advection

$$Pe_L = \frac{Lu}{a} \qquad\qquad (Eq\ 36)$$

Where 'a' is the thermal diffusivity (of water), being 0.143E-6 [m^2/s]. [57] L*u is the length scale multiplied by the average velocity, respectively. This comes to a value of 0.0003[m]*0.00002[m/s] = 5.98E-9 [m^2/s], using the height of the model, and the highest net velocity. Details are in appendix A3. The Peclet number would then be 0.042, and heat transfer can be modeled using only conduction.

Similarly, fluid flow from electrothermal effects is simulated through the incompressible Navier-Stokes equation. (Eq 34) The force exerted on the fluid is given by (Eq 10) to (Eq 15).

3.6.6 Plotting the Path of a Bacterium

There are two forces which would move the bacteria: dielectrophoresis, and the Stokes drag force. At equilibrium, the net velocity of the particle would be equal to the velocity of the fluid, plus the terminal velocity with respect to the fluid, provided by dielectrophoresis. For a massless particle, any change in the force would provide an immediate acceleration to its net velocity at equilibrium, and for a system in steady state, its path could be accurately plotted by finding its streamline, for its path line will coincide.

However, bacteria has mass. And any change in the force will be accompanied with a time required for it to reach equilibrium. If the assumption was made that a bacterium to simplify plotting its trajectory, the

time required for the bacteria to equilibrate to a change in forces, must first be found, in order to justify this assumption.

The equilibrium state of the bacterium would have zero net force. When the bacterium is out of equilibrium, it would take some time to accelerate to its new net velocity. There are two forces involved in this phenomena: the fluid force, and the DEP force, and we will consider them separately. Consider a case where a bacterium with an initial velocity is moving inside a very large amount of fluid with zero velocity. The only force involved in decelerating or accelerating a bacterium would be the fluid drag force, given by $F_{drag} = f * V$. Where f is the friction factor, and V is the velocity relative to the fluid. Taking the time integral of the equation with the velocity limits at V_0 and 0, we obtain (Eq 37). [58]

$$\frac{V}{V_0} = e^{-\frac{f}{m}t} \qquad\qquad \text{(Eq 37)}$$

The time constant for this process is m/f, calculated to be 5.5 X 10^{-8} seconds, which is the time it takes to decelerate to 37% of its original velocity. Considering the analogous case, where a constant force was pulling the particle through a fluid, where its initial velocity was a non-zero value, the same time constant could be derived.

Comparing a bacterium to a massless particle, the massless particle will experience instantaneous acceleration, whereas the bacterium will take time to accelerate to its equilibrium velocity. So, the pathline of a massless particle will not follow the pathline of a bacterium. However, it is possible to calculate the amount the bacterium will deviate by. Due to its slower acceleration, the bacterium will lag behind. For each element along a massless particle pathline, this could be calculated, and totaled.

The amount of time for the bacterium to reach 99.9% of its equilibrium velocity is 3.8E-7 seconds. To simply calculations, it is assumed that the bacteria will be traveling at its initial velocity along this element for this period of time, before accelerating instantaneous to the velocity at the end of the

element. Whereas the massless particle would instantaneously accelerate to the end of the element, and remain there.

The pathline for a massless particle were plotted, and the differences in trajectory were calculated as a magnitude, to a height of 1 μm above the surface. The pathlines plotted were confined to an area 10 μm by 10 μm at a height of 1 μm above the surface, to maintain relevance to the area where the bacterium is expected to land. The deviation between the pathline of the bacterium and the massless particle were summed for each element in a pathline, and an average was provided for all the pathlines in each operating condition.

Table 5: Average deviation between the pathline of the bacteria, and the pathline of a massless particle, provided as a magnitude.

Operating Conditions	Average Deviation (m)
8V 1kHz	-1.13572E-09
8V 10kHz	-3.32413E-08
8V 100kHz	-3.49568E-08
8V 1MHz	-3.43937E-08
13V 10kHz	-6.77295E-08
20V 100kHz	-2.68253E-07
20V 1MHz	-2.09101E-07

As seen, the difference in distance between the pathline of a bacterium and the pathline of a massless particle was, at most, on an order of magnitude of 100 nm, with an estimation method that over-estimated the difference due to acceleration. So, it can be safely concluded that the pathline of the bacteria could be estimated using the pathline of the particle.

4.0 – Experimental Results and Discussion

4.1 – *E. coli* Capture

An example of the bacterial collection patterns that form in the vicinity of the microelectrodes within a few minutes after the electric field is turned on can be seen in Figure 16a. It should be noted that these surfaces were not functionalized with antibodies, explaining the lack of retention. Furthermore, it should be noted that collection at high concentrations of bacteria will result in a distorted electric field, which would result in a consistent, but not regular collection of bacteria. The image was acquired while the water droplet containing the bacterial suspension was still in place. The bacteria, seen in Figure 16a as dark formations, collect near the edges of the gold microelectrodes. The speed and size of these bacterial formations are strongly dependent on the bacteria concentration in the droplet, but also on the AC electric field conditions (voltage, frequency). The result seen in Figure 16a was obtained under conditions of 20 Vpp, 1 MHz and bulk concentration of 10^9 bacteria/mL. The observed accumulation of bacteria is caused by *dielectrophoresis* (DEP), the deterministic motion exhibited by polarizable objects as a result of their interaction with a spatially non-uniform electric field [10]. The intensity of the latter depends on the voltage and frequency that is applied to the microelectrodes. The force that causes dielectrophoresis of bacteria (*dielectrophoretic force*, *FDEP*) depends on the properties of the liquid medium and microorganism, as well as the electric field characteristics. The time averaged force in the x direction is given by [55] in (Eq 28).

The Clausius-Mossotti factor (Re[Ke]) can be calculated from (Eq 8). The numerical sign of the parameter Re[Ke] has a major influence on the bacterial capture patterns. Specifically, when Re[Ke] assumes positive values, the dielectrophoretic force acting on the bacteria causes them to accumulate in areas of high electric field gradients; this phenomenon is termed *positive* DEP. In the opposite case (*negative* dielectrophoresis) the bacteria are pushed away from such high field intensity gradients. To help with

47

the visualization of locations where such high gradients exist in the microelectrode vicinity, the color

map of Figure 16b is included. Figure 16b displays the spatial variation of the gradient of the electric

field squared, a quantity that is proportional to the dielectrophoretic force. The simulations were

performed using the finite elements software COMSOL Multiphysics®. It can be seen that the high

electric field intensity gradients occur at the edges of the microelectrodes and become more intense as

the separation between neighboring, *i.e.*, oppositely charged, electrodes becomes smaller. Cross-

examination of Figure 16a and Figure 16b shows that the experimentally observed bacterial

accumulation patterns are the result of positive dielectrophoresis (Re[Ke]>0). Moreover, the strongest

capture force is expected to occur at the points where the separation gap between adjacent electrodes

is at its minimum. An example of the bacterial collection patterns around the microelectrode tips after

droplet removal and surface rinsing is seen in Figure 16c. The *E. coli* appear as green areas on the chip's

surface (brown background) between the gold microelectrode tips. Evidence that these areas

correspond to captured bacteria is provided by the SEM image of Figure 16d, where the green areas are

identified as bacterial capture locations. This capture pattern is also consistent with positive DEP, i.e.,

the concentration of captured *E. coli* becomes higher as the separation between adjacent

microelectrodes becomes smaller.
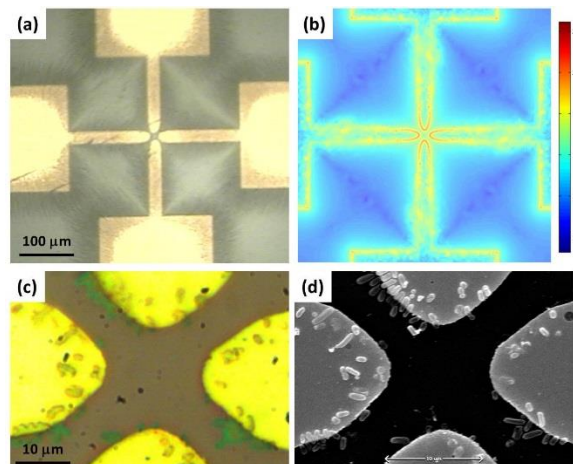
Figure 16: (a) A typical bacteria collection pattern under positive dielectrophoresis with the droplet still in place, and a voltage of 20 Vpp at 1 MHz. (b) Simulated electric field gradients on the surface of the microelectrode (c) Optical and (d) SEM images of bacteria collected at the microelectrode tips after droplet removal and rinsing.

4.2 Effect of AC Frequency and Applied Voltage on Bacterial Capture Efficiency.

The effect of AC frequency and voltage on the bacterial sampling efficiency was investigated. The AC electric field frequencies examined were 1 kHz, 10 kHz, 100 kHz and 1 MHz. First, the voltage applied across the electrodes was kept constant at 8 V_{pp}, which was found to be the highest potential difference that did not result in microelectrode damage at 1 kHz. Samples of 30 μL volume containing 10^6 particles/mL were subjected to an electric field continuously for a period of 15 min. The sampling interval of 15 min was determined experimentally to be the most effective electrification time. Longer exposures to the electric field produced no perceivable difference in the amount of captured bacteria.

The microchips were then rinsed with filtered water and dried in a nitrogen gas stream. The results show a trend of increasing collection efficiency with decreasing AC frequency (Figure 17, top row). For a voltage of 8 V_{pp} across the microelectrodes, no collection was noticeable in the case of 1 MHz, hence the results are omitted. Poor capture efficiency is noticed also for the case of 100 kHz, with better capture occurring at 10 kHz and 1 kHz. Although the observed capture patterns varied slightly among replicates, the results did not differ substantially between 10 kHz and 1 kHz and 8 V_{pp}. Overall, these tests show that, for the same applied voltage value, a better collection is to be expected at the lower electric field frequency window [1 kHz-10 kHz]. The variation of bacterial collection efficiency with frequency is an indication that AC electroosmosis plays a significant role in the signal amplification process. More specifically, it is known that AC electroosmosis becomes insignificant over 100 kHz [6], which in our case, coincides with the upper frequency limit of bacterial detection. A thorough exploration of the AC electroosmotic effect on the bacterial captures observed in our experiments has been reported elsewhere [25]. Although high AC frequencies show poor bacterial capture performance, they permit

higher voltages to be applied without noticeable electrode damage. Our experimental investigation showed that the maximum sustainable voltage, i.e., the voltage above which microelectrode deterioration due to electrochemical reactions begin to occur, increases gradually with frequency. For the specific set of microelectrodes used in our experiments, the maximum voltage values that could be applied were 8 V_{pp} (1 kHz), 13 V_{pp} (10 kHz), 20 V_{pp} (100 kHz), and 20 V_{pp} (1 MHz). The value of 20 V_{pp} corresponds to the maximum voltage outputted by the signal generator. The above differences can have a substantial effect on bacterial capture efficiency if one considers that dielectrophoresis scales with the second power of voltage (Eq 28). Figure 17 (bottom row) displays images of the electrodes taken after 15 minutes of sampling time under maximum allowable voltage for each frequency. The most effective combination among those examined was found to be 13 V_{pp} (max sustainable value) at 10 kHz, resulting in a very intense diamond pattern forming between the edges of adjacent electrodes. The results also underline the significant effect of applied voltage. Although insignificant collection was observed at 8 V_{pp} at 100 kHz, the captured bacteria at 20 V_{pp} are, in fact, more than those seen at 8 V_{pp}, 1 kHz. The bacteria collection performance at 1 MHz and all voltages up to 20 V_{pp} was very poor, hence it is not included in the comparison.
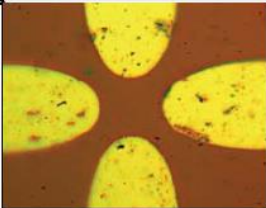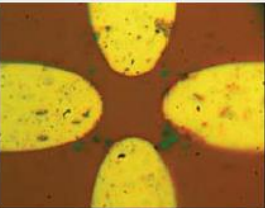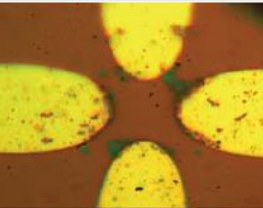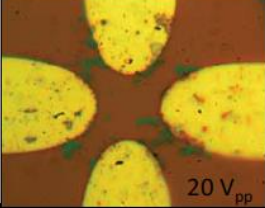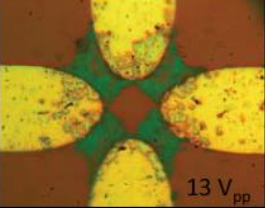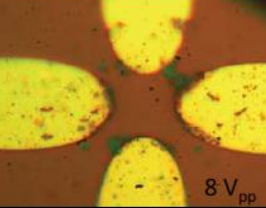
Figure 17: Testing bacteria capture at various voltages and frequencies. 50 µL of 10^6 bacteria suspension was collected for 15 minutes. Photographs were taken after capture, and after the droplet was washed with water and dried. The bacteria are seen as green spots against the brown silica background, and gold electrodes. Best capture is seen under conditions of 13 Vpp and 10 kHz. [59]

4.3 Detection of Bacteria with Micro-Raman Spectroscopy

4.3.1 Raman Spectra of Bacteria

Having identified a set of favorable (f, V) conditions for bacterial sampling, the focus is now shifted to the assessment of micro-Raman as a suitable signal transduction method. The Raman spectra for *E. coli* (target bacterium) and M. luteus are shown in Figure 18. The spectra were obtained from bacterial films formed on an oxidized silicon wafer through droplet evaporation. It can be seen that, in both cases, the strongest Raman shift occurs in the region 2850-3050 cm^{-1}, indicated by the arrow in Figure 18 and consists of overlapping, non-specific organic $>CH_2$ and - CH_3 stretching modes [40]. This broad peak is so strong that makes possible the detection of a single bacterium by means of micro-Raman spectroscopy. On the other hand, the (mono) layer of BSA and antibodies alone produces a very weak Raman signal with a peak of negligible intensity in the same region. Although the detection of captured bacteria can easily be accomplished by readily monitoring the 2850-3050 cm_{-1} Raman shift, use of a different region of the spectrum (1200-1800 cm_{-1}) is necessary for the identification of the captured microorganism. This can be accomplished by means of Principle Component Analysis (PCA). However, within the scope of this thesis, identification between *E. coli* and *M. luteus* is done by comparing the presence of the peak at 1528 cm^{-1}, which is characteristic of the compound sarcinaxanthin found in *M. luteus.* [60]
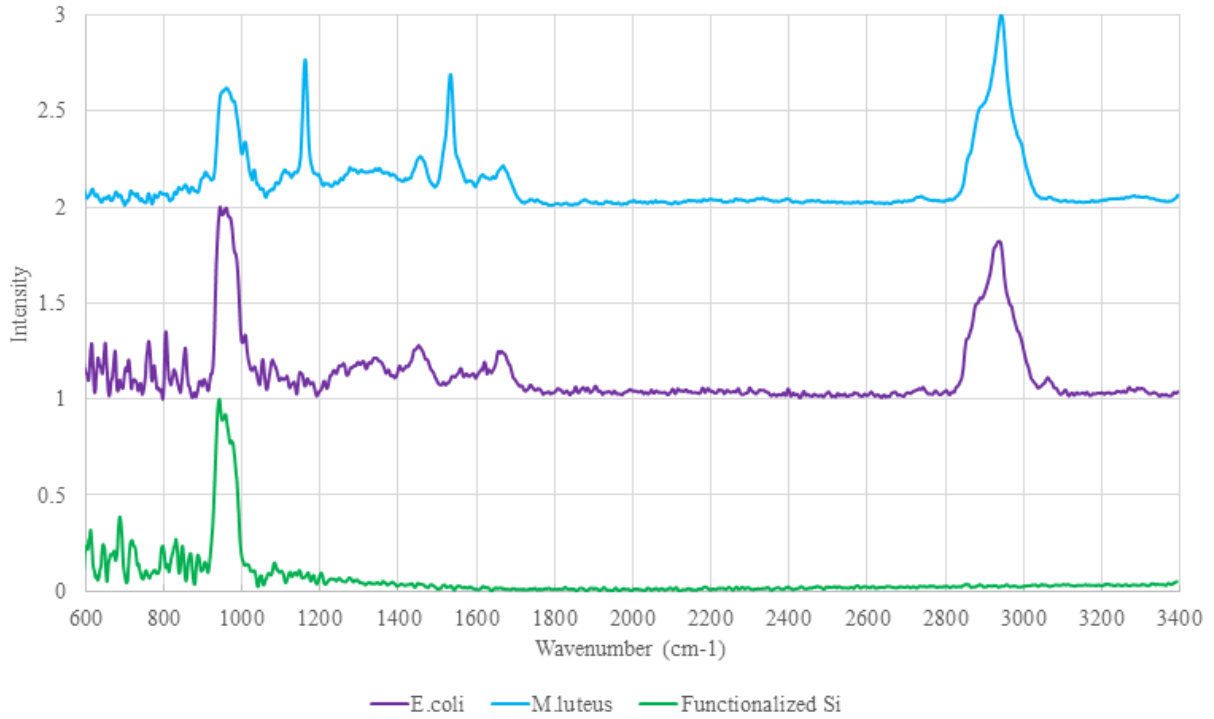
Figure 18: Spectra of E. coli on functionalized silica, M. luteus on functionalized silica, and the functionalized silica by itself. Results are normalized with respect to the highest peak, then shifted upwards.

4.3.2 Limit of Detection

The ability of the method to detect the presence of *E. coli* at low concentrations was tested and compared against various controls. The results are summarized in Figure 19. Figure 19a is a plot of the measured area-under-curve of the broad peak at 2850-3050 cm$_{-1}$ vs. bacterial concentration in the droplet. Each point in the graph represents the mean of 24 measurements (2 microelectrode sets x 12 locations per microelectrode). The data set indicated as "*E. coli*" corresponds to the results obtained when combining an anti-*E. coli* capture layer and an electric field of 12 V_{pp} and 10 kHz. *E. coli* detection from samples at concentrations as low as 10^2 bacteria/mL can be seen. This is impressive considering that a 50 µL droplet contains a total of roughly 5 bacteria. Visible light microscopy revealed that this detection signal was the result of 1 or 2 captured bacteria at the electrode tips. On the other hand, poor collection efficiency is observed at 12 V_{pp} on surfaces that contained BSA and Avidin but no antibodies (data set: "BSA at 12V"). Apparently, although the electric field can attract *E. coli* to the surface, the presence of a hydrophilic protein layer and absence of antibodies causes the removal of the captured bacteria during the rinsing step. Similarly, when an antibody layer is present but no electric field is activated, not collection can be observed within 15 min (data set: "Ab 0V").

The results acquired when combining an electric field and an antibody-functionalized layer (data set "*E. coli*") are plotted again in a log-log plot (Figure 19b) so that the strong signal acquired from low concentration samples can be appreciated. As also mentioned above, the method is sensitive enough to detect the presence of a single bacterium captured at the gaps between the electrode tips. In the present case, a second degree polynomial can correlate reasonably well the measured area-under-curve with bacterial concentration in the bulk of the sample droplet
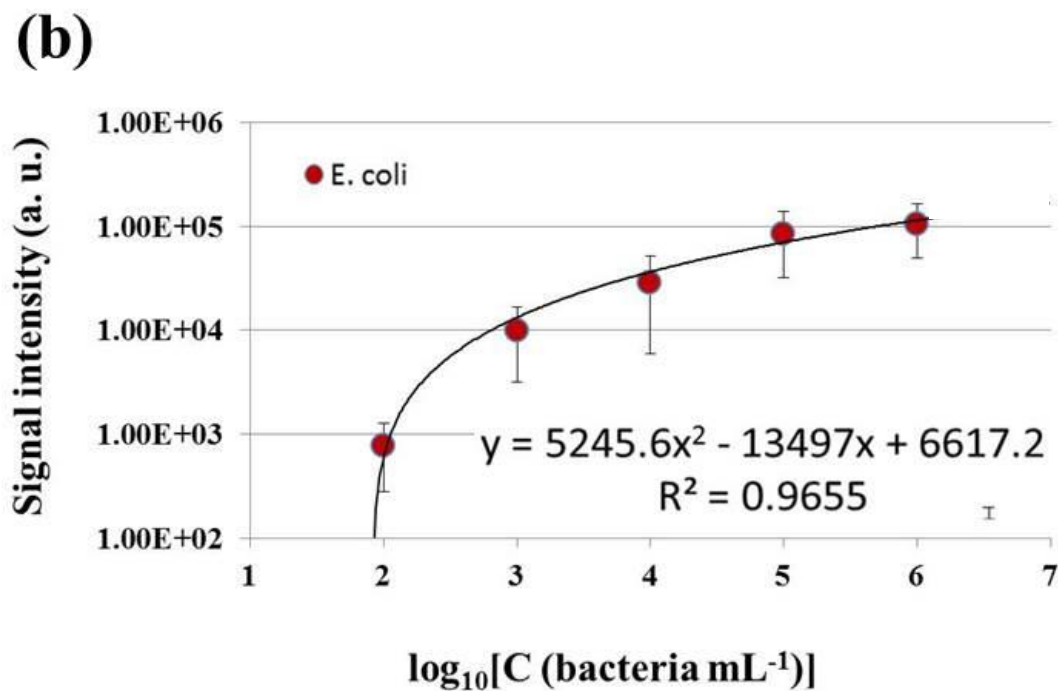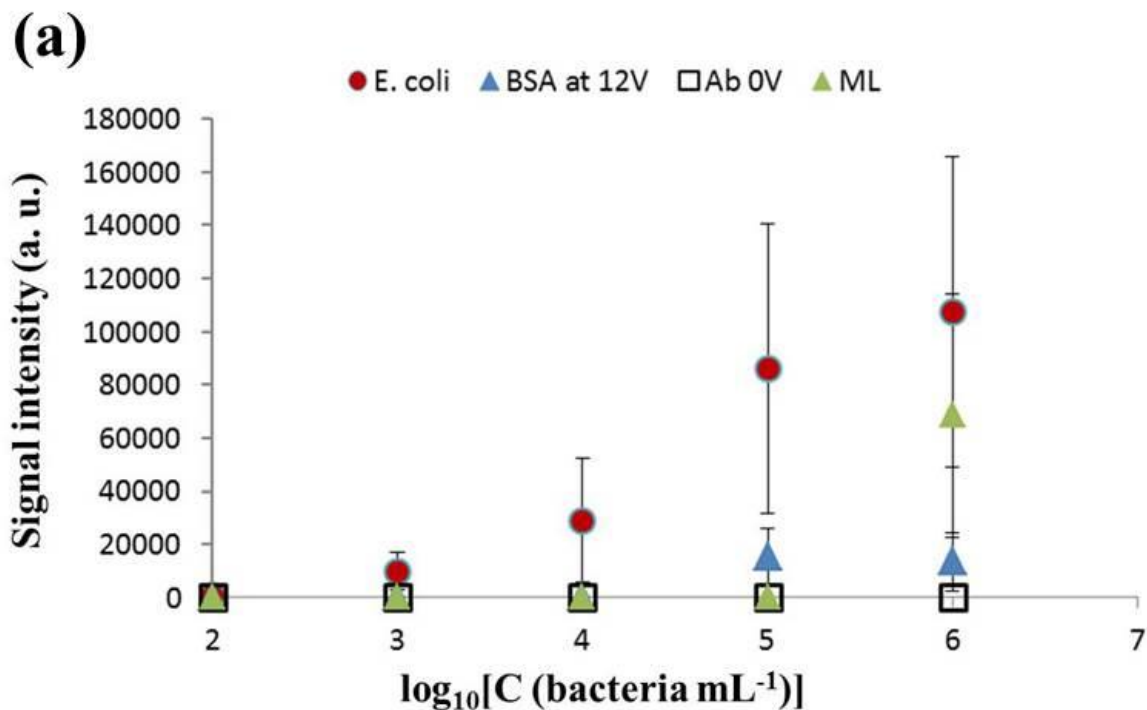
Figure 19: (a) Signal intensity as a function of bacteria concentration under various experimental conditions (b) Correlation between the Raman signal strength of captured E. coli K12 and their respective concentration in the water droplet on a log-log plot. The fitted function displays the relation between the signal intensity (y) and the concentration (x). No signal was obtained at 10 bacteria / mL, so the function was extrapolated downwards.

4.3.3 Selectivity

The selectivity of the method was tested by performing the same detection protocol using suspensions of *M. luteus* instead of *E. coli*. The results can be seen in Figure 19 (data set: "ML"). A remarkable degree of selectivity is observed for concentrations up to 10^5 bacteria/mL. At higher concentrations, it can be seen that some *M. luteus* becomes non-specifically attached to the surface. Finally, the ability of the method to selectively retain a target pathogen in samples containing mixed bacterial populations was briefly tested using 50:50 mixtures of *E. coli* and *M. luteus* with total concentration of 10^4 bacteria/mL. The sampling protocol was kept the same as before (10 kHz, 13 Vpp, 15 min of electric field exposure). Figure 20 shows a characteristic capture pattern from these tests. Identification of the captured bacteria performed with the aid of micro-Raman spectroscopy revealed the predominance of *E. coli* in the area of the microelectrode tips. Only one of the captured bacteria (circled) was identified as *M. luteus*. When the same experiment was repeated, no *M. luteus* could be detected in the same area. It must be noted that the results with *M. luteus* are presented here as the "worst case scenario" since this microorganism was found to be difficult to remove, once captured. Other experiments performed with *P. fluorescens* (results not shown) resulted in minimal retention of non-target bacteria, even at higher concentrations (10^9 bacteria/mL).
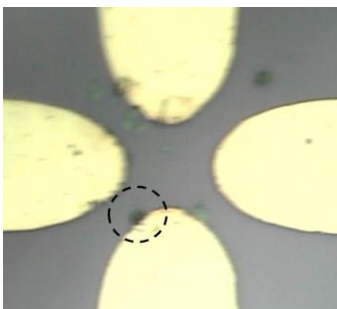
Figure 20: Demonstration of the method's selectivity to E. coli: (a) A collection pattern obtained from a sample containing a heterogeneous population of bacteria after droplet removal and rinsing. The identification of the captured microorganisms was performed with Raman spectroscopy. The dashed circle indicates the presence of a non-target bacterium (M. luteus)

5.0 - Simulation Results and Discussion

For an in depth understanding of the mechanisms behind bacteria collection, numerical simulations were performed. The purpose of the simulations was to explore the effect of operating conditions (AC frequency and applied voltage) on the resulting fluid flow patterns and force field acting on the bacteria. The three major electric field-dependent phenomena that were explored were: dielectrophoresis (DEP), electroosmotic flow (ACEO flow), and electrothermal flow (ET flow). Dielectrophoresis is manifested by the action of the dielectrophoretic force (DEP Force) on the particle as a result of the presence of electric field gradients. The ACEO flow is a fluid flow resulting from a tangential component of the electric field inside the electrical double layer. The electrothermal flow is a fluid flow, for which the driving force are temperature gradients in the fluid and electric field gradients.

Earlier simulations reported by Shiva Golchi [54] proved to be inconclusive and did not clearly link the observed experimental trends with the simulation. In the present case, several improvements were introduced in the simulations, in order to overcome the shortcomings of the previous effort. Specifically, the mesh density was increased near the electrode tips and edges, in order to allow a more accurate calculation of the electric field gradients in these areas

- A new visualization plane was added to allow the visualization of forces and fluid flow patterns in the area where the most intense bacterial collection was experimentally observed

- The calculation of the electrical double layer capacitance (C_{dl}) now takes into account ionic steric effects, rather than the Debye-Hückel model. The effect of this correction on the calculated C_{dl} value is illustrated in Appendix A4.

- Ratios of the DEP velocity to the fluid velocity were plotted on planes throughout the model, so that the significance of each of the driving forces could be inferred with respect to the distance away from the electrode.

5.1 Velocity Magnitudes at the Microelectrode Tips

The effect of operating conditions on the average electroosmotic and dielectrophoretic velocities was first examined locally in the area where the most intense bacterial capture was observed, i.e., along the line of minimum separation between neighbouring electrodes. (Figure *21*) Since the ACEO velocity originates from a slip velocity, the representative value was chosen to be an average over the electrode tips. Similarly, the dielectrophoretic velocity was chosen to be an average along the shortest length (red dotted line in Fig. 1). Since the DEP force is a force that acts on the bacteria themselves it cannot be compared to the ACEO fluid velocity. However, if we model a massless, point particle with the same stokes friction factor as an *E. coli* bacterium, we can translate this force into a terminal velocity.
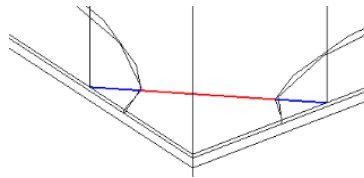
Figure 21: Lengths for which forces are averaged. The ACEO force is averaged over the lengths in blue (dotted line), and the DEP force is averaged over the length in red (dashed line). The total force is averaged over the entire coloured length.

The plots of the average ACEO fluid velocity, DEP force, equivalent DEP velocity, and net velocity across the lengths described in Figure 21 are shown in Figure 22. Figure 22a describes the average electro-osmotic velocity peaking at 10 kHz, with a velocity of 2.27E-3 m/s at 20 Vpp. Figure 22b describes the averaged DEP force, plateauing with frequency. We would expect higher values with higher frequencies, as there will be less electrode shielding, higher gradients, and higher DEP forces. (Eq 28) Figure 22c displays the net velocity as the magnitude of the sum of the vectors of the ACEO force, DEP force, and electrothermal force. Finally, the DEP force was translated to a terminal particle velocity, (Eq 32)

displayed in Figure 22d, so that it would be comparable to the ACEO force. The net velocity would be the sum of the vectors of the DEP terminal velocity, and the fluid velocity.
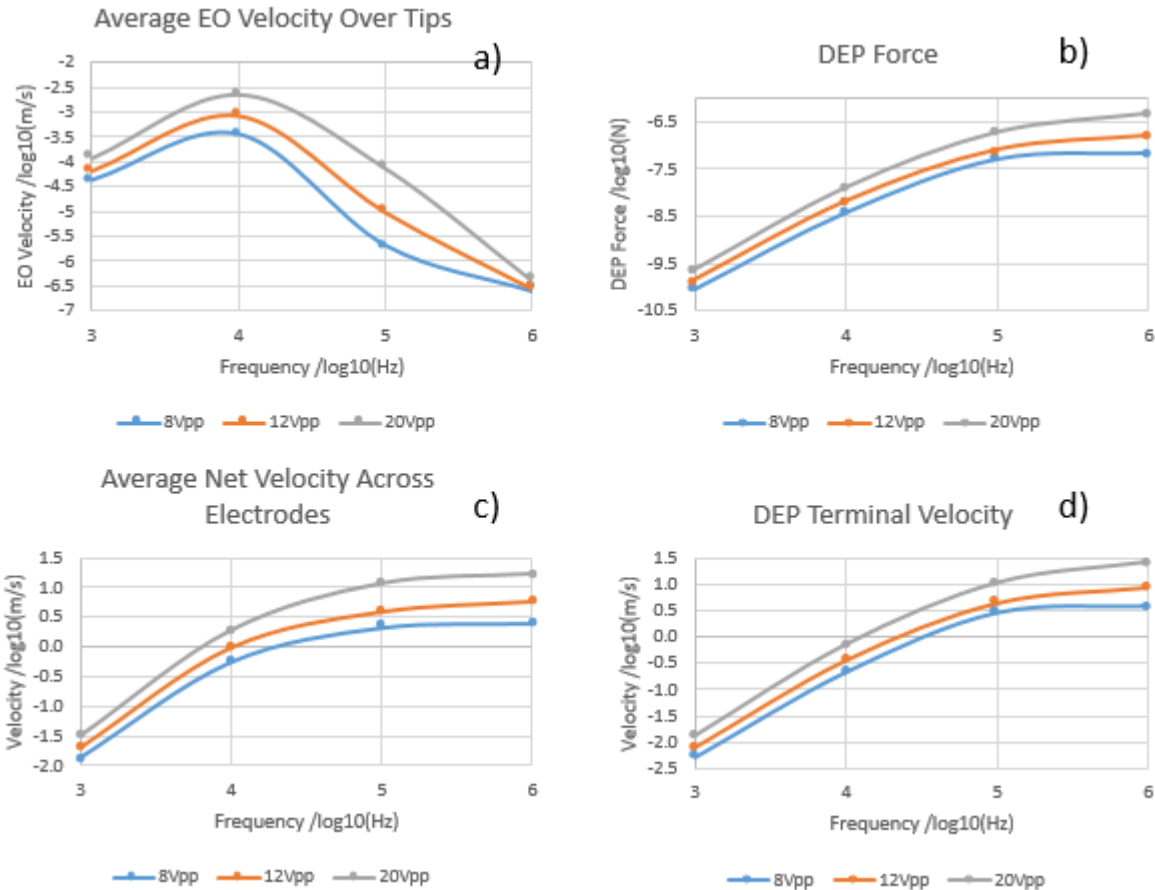
Figure 22: Graphs showing: a) averaged electro-osmotic velocity, b) dielectrophoretic force, c) net velocity, d) and the terminal velocity from the DEP force. The lengths for which these averaged values are obtained are shown in Figure 21.

ACEO would only occur at a frequency range where the EDL and a tangential electric field component are present. At frequencies much higher than the relaxation frequency, the EDL would not have time to form, whereas at frequencies much lower than the relaxation frequency, the EDL would form fully. In both cases, the ACEO flow would be minimized due to a reduced time aver force in the diffuse layer. The frequency at which the EDL would dissipate is dependent on the electric field strength, which is dependent on the electrode separation. The smaller the electrode separation, the higher the electric

field strength, and the higher the frequency at which the EDL would dissipate. This charge relaxation frequency can be estimated after making several assumptions, and is plotted in Figure 23. Calculations and assumptions are listed in Appendix A5.

Due to the distribution in charge relaxation frequencies over the electrode surface, operating at a fixed frequency close to theSince the charge relaxation frequency is dependent on electrode separation, more of the electrode will experience a relatively high ACEO flow at lower frequencies. However, this effect is supressed when only looking at the tips of the microelectrodes, as there was a relatively little difference in separation distance between the lengths of integration. At this separation distance of 6-10 μm, the frequency is roughly 10 kHz, (Figure 23) so it would be expected to see a peak in EO velocity at this operating frequency.

Across the electrode tips the equivalent DEP velocity is much greater in magnitude compared to the ACEO velocity, making it the dominant force in this region. (Figure 22a and Figure 22d) Furthermore, the trends displayed in the net velocity (Figure 22c) matches the trends found in the DEP velocity (Figure 22d).
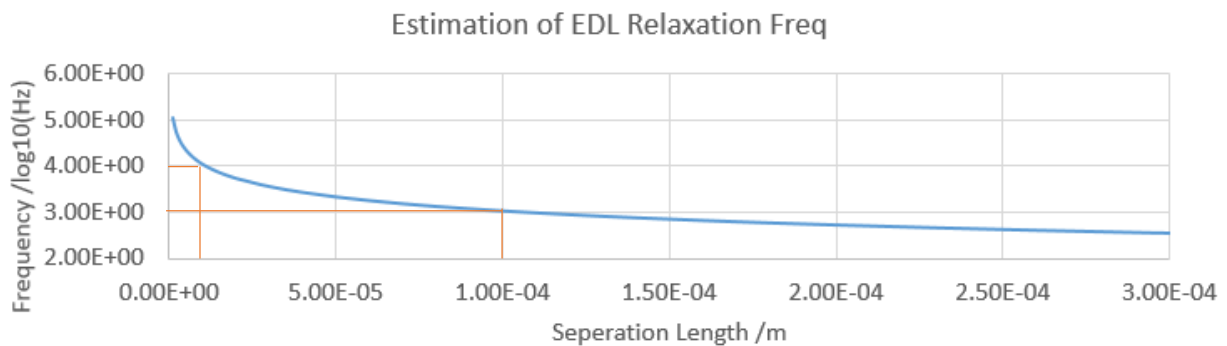
Figure 23: Charge relaxation frequency of the EDL with respect to separation distance between two corresponding points on each electrode. Around 10 kHz, areas on the electrode with separation distance smaller than 10 μm would be shielded with an EDL. At around 100 kHz, areas on the electrode with a separation distance smaller than 100 μm will be shielded with an EDL. Details of the calculation are provided in the appendix. (A5)

As seen in Figure 23, the charge relaxation time is higher with a smaller separation distance. Past a separation distance of 100 μm, the relaxation frequency drops down to below 1 kHz. It should be noted that this is just a generalization and other factors affect the electric field such as electrode geometry, and non-isotropic electrical properties, especially within the EDL in an alternating current.

Wei *et al.* measured the magnitude of the DEP force between particles using laser tweezers. For particles of similar size, between 1-2 microns, the DEP force was on the order of 1 pN using 2D electrodes with a 50 micron gap, 10 kHz, and 5Vpp. [61] Our simulations suggest that under the same frequency, the force experienced across the electrodes would be approximately 3 nN (Figure 22). The operating conditions used, however, were with an electrode separation of 6 μm and 8Vpp. To compare these two results on the same basis, a dimensional analysis was performed. Considering that the DEP force is proportional to the gradient of the square of the electric field, (Eq 28) the following correlation can be derived between the force predicted in this work (F_{dep1}) and that measured by Wei *et al.* (F_{dep2}):

$$\frac{F_{dep1}}{F_{dep2}} = \left(\frac{L_2}{L_1}\right)^3 \left(\frac{V_1}{V_2}\right)^2 = \left(\frac{50}{6}\right)^3 \left(\frac{8}{5}\right)^2 = 2370 \qquad \text{(Eq 38)}$$

Which is very close to the actual ratio of (3 nN/1 pN≈ 3000).

5.2 Velocity Correlations in the Bulk

In Figure 24, the phenomena moving the bacteria are presented as an average throughout the entire bulk of the model representing the liquid. Figure 24a shows the average electroosmotic velocity in the bulk. At frequencies larger than 1 kHz, the velocity falls down to smaller than 1 μm/s. Unlike at the tips of the electrodes, where the EO velocity peaks at 10 kHz, the EO velocity as an average throughout the entire liquid volume in the model decreases as the frequency increases, as seen in Figure 24a. Experiments by Brown *et al.* [62] and Studer *et al.* [15] suggest a peak in the bulk velocity at 1 kHz in similar conditions. This phenomenon can be explained by an increase in the amount of area experiencing significant electroosmotic flow as the frequency decreases. This explanation becomes more obvious in the following section.

 Figure 24b shows the average electrothermal velocity in the liquid. It peaks at a frequency between 10 and 100 kHz. The electrothermal velocity is highest at 10 kHz, with its second highest value being at 100 kHz. The driving force behind electrothermal fluid flow is the temperature gradient, caused by joule heating. Although the thermal gradient is higher at the surfaces, it is also subject to no-slip conditions, creating a maximum ET flow just above the surface. At relatively low conductivities of 0.001 S/m, the electrothermal flow is very small in comparison to the electro-osmotic flow, especially at the surface. Comparing the two fluid velocities, the averaged electrothermal fluid flow is only on par with the averaged electroosmotic fluid flow above 10 kHz, and 12 Vpp. This makes sense, as the ACEO velocity decrease drastically with frequency within the bulk.

Figure 24c is the terminal velocity resulting from the DEP force. It varies relatively little with frequency, compared to the other fluid velocities, with the largest difference being 1.68E-5 m/s at 20 volts peak to peak between 1 kHz and 1 MHz at 20Vpp. The trend for dielectrophoretic velocity with frequency at the tips of the electrodes remains the same for the bulk, i.e., the velocity plateaus with frequency. At lower

frequencies, the dielectrophoretic force and the electro-osmotic force are comparable in magnitudes. But as the frequency increases, the DEP velocity quickly becomes dominant in the bulk. However, just knowing the magnitudes of the relevant velocities cannot grant knowledge of the direction of flow. Flow patterns will be explored in the next section.

Figure 24d depicts the variation of net velocity with AC frequency and voltage. The net velocity is calculated by taking the sum of the three velocity vectors, then finding the average magnitude throughout the bulk. As it can be seen, the magnitudes of the net velocity are comparable to DEP velocity at frequencies higher than 1 kHz. With the DEP force comprising the majority of the net force, it is to be expected that the net force follows the same trend with frequency. However, at 1 kHz, where the DEP and electroosmotic velocities become comparable in magnitude, a substantial contribution from both effects to the net velocity can be observed.
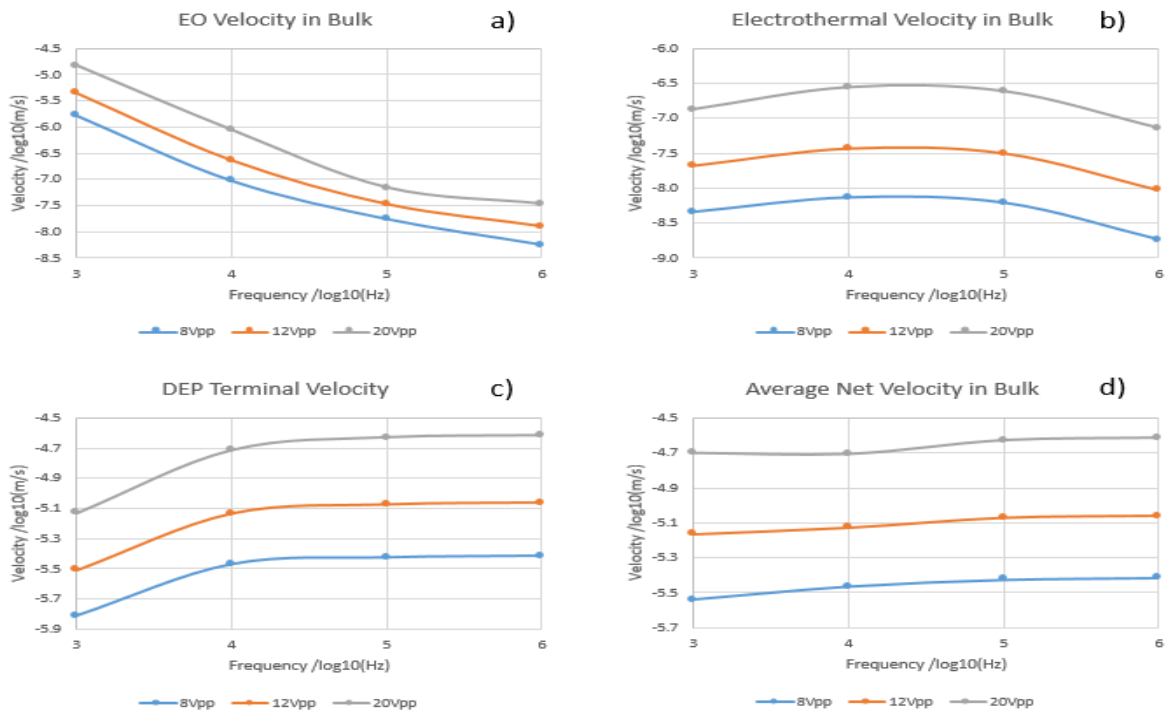
Figure 24: Plots of bulk averaged values for: EO velocity a), Electrothermal flow velocity b), DEP terminal velocity c), and the net velocity d).

5.3 AC Electroosmotic Flow

The vector field and colour plot of the ACEO velocity were plotted on the surface of the electrodes and adjacent parallel planes as well as the plane extending 80 µm from the line highlighted in Figure *21*, hereon referred to as plane 19. This was done to visualize the flow patterns and force field in the area where the bacteria capture was experimentally observed. (Figure 25)

Generally speaking, and with certain exceptions, the direction of the EO flow is consistent with theory, in that the fluid flow is seen to be drawn downwards towards the electrodes then brought outwards away from the electrode edges. Furthermore, at lower frequencies the flow is seen to flow over the electrodes, whereas at frequencies greater than 1 kHz, the flow is seen to circulate over the edges. (Figure 26) This is consistent with the findings of Morgan and Green. [55]

At lower frequencies, more of the electrode experiences a significant electro-osmotic flow, due to the distribution of charge relaxation times with respect to electrode separation distance. (Figure 23) This phenomenon is seen by contrasting the frequencies at 1 kHz, and 10 kHz at 8 Vpp in Figure 25. At 8Vpp and 1 kHz, a larger area on the electrode experiences a flowrate larger than 10 µm/s, than at 8 Vpp and 10 kHz. But larger magnitudes are found at the electrode tips at 8Vpp and 10 kHz. This is reflected in the flow patterns in the square area between the electrodes. At 1 kHz, more of the water is drawn towards the larger surface area, while at 10 kHz, the water is drawn evenly towards the electrode edges.

It should be noted that at some conditions, the ACEO flow is opposite of what is expected on the electrodes, as seen at 10 kHz in Figure 25). This can be explained through the geometry of the electrodes. At the tip, the magnitude of the electric field is much stronger, but further inwards, the charge relaxation frequency is met, creating a resonance effect. This creates two maxima in EDL shielding. This causes the electric field and ACEO flow to be in the opposite direction than what is to be expected in some areas. This phenomenon is described in Appendix A6.

Figure 25: ACEO velocity on the electrode, and adjacent surfaces. The colour represents the magnitude of flow, plotted on a log10 scale, ranging from 10^2.6 m/s to 10^-10.6 m/s. The arrows represent the direction of velocity. Different operation conditions were shown, with the frequency ranging from 1 kHz to 1 MHz, and the voltage ranging from 8 Vpp to 20 Vpp. The maximum operation voltage for the given frequency were determined experimentally, and are indicated. The colour scale was truncated to better show contrast between operating conditions.
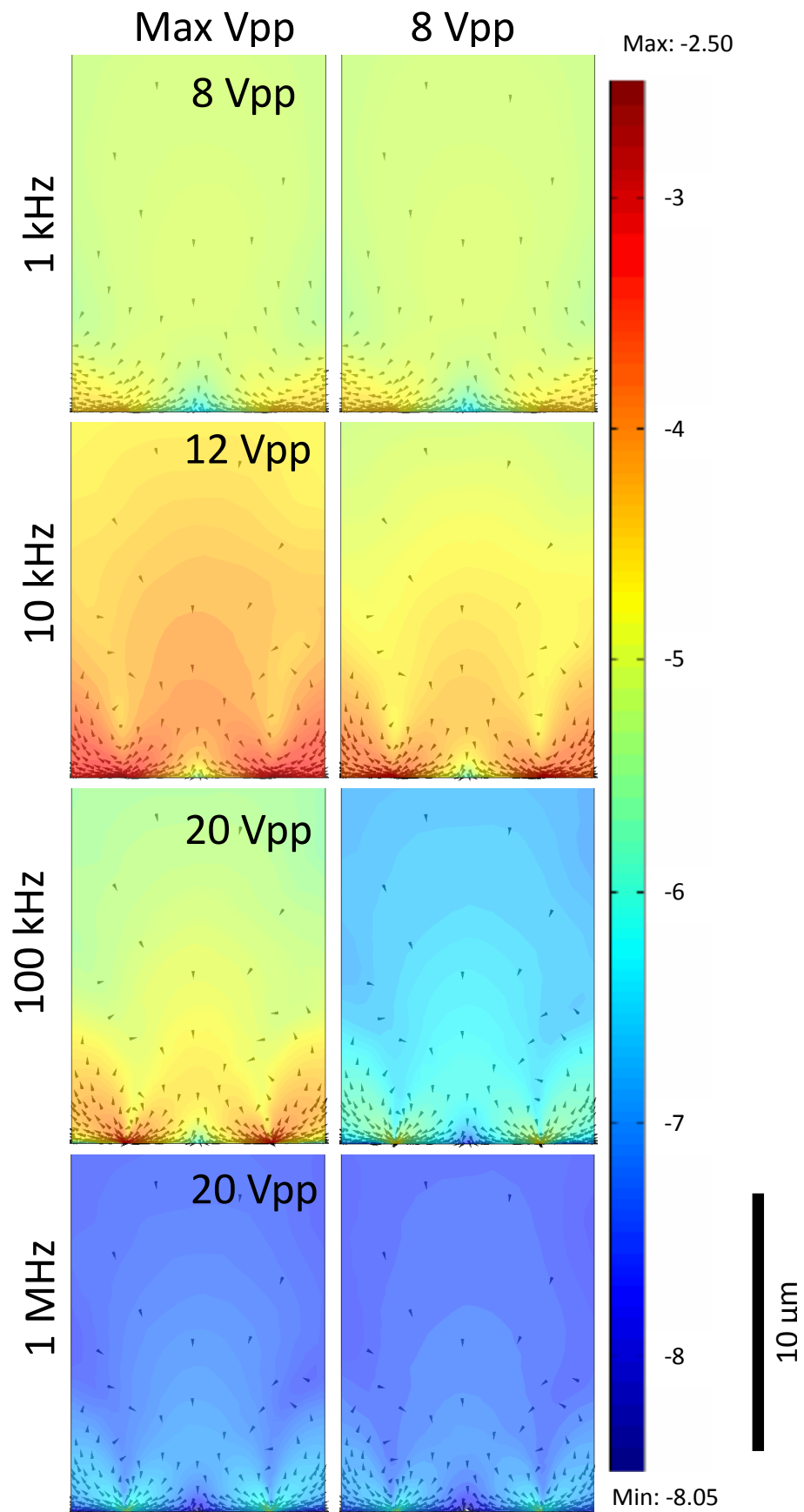
Figure 26: ACEO fluid flow vectors and magnitude plots on Plane 19, the plane intersecting the electrode tips extending 80 um from the electrode surface. The colour represents the magnitude of flow, plotted on a log scale, ranging from 10^2.5 m/s to 10^-8.5 m/s. The arrows represent the direction of flow. Different operating conditions were shown, with the frequency ranging from 1 kHz to 1 MHz, and the voltage ranging from 8 Vpp to 20 Vpp.

5.4 Dielectrophoretic Force

As explained in a previous section, a positive DEP force is experienced (Figure 15), meaning the force will be in the direction of the electric field gradient. This force can be translated to an equivalent terminal velocity for a massless particle with the same friction factor as an *E. coli* cell. Looking at the vector field plotted in Figure 27 and Figure 28, this trend is observed, as the vectors are pointing towards areas where a higher electric field is expected.

With increasing frequency, the DEP velocity is seen to increase. This is seen in Figure 22, Figure 24, and Figure 28. Looking closely at Figure 28, it is seen that the decreased shielding at higher frequencies results in an increased electric field gradient on the surface of the electrodes. At higher frequencies, the increased electric field gradient causes the DEP vector field to point towards the electrode tips.

This shielding effect is also seen in the X-Y plane in Figure 27. At 1 kHz, the DEP force is seen to be mostly perpendicular to the electrode surface and pointing downwards, at areas close to the edges. At areas where the electrode is shielded, there is also a higher electric field gradient. As the frequency increases, less of the electrode area becomes shielded and the DEP would gain more a tangential component, pointing toward the electrode edges.

Figure 27: DEP terminal velocity on the electrode, and adjacent surfaces. The colour represents the magnitude of flow, plotted on a log10 scale, ranging from 10^2.5 m/s to 10^-6 m/s. The arrows represent the direction of velocity. Different operation conditions were shown, with the frequency ranging from 1 kHz to 1 MHz, and the voltage ranging from 8 Vpp to 20 Vpp. The maximum operation voltage for the given frequency were determined experimentally, and are indicated. The colour scale was truncated to better show contrast between operating conditions.
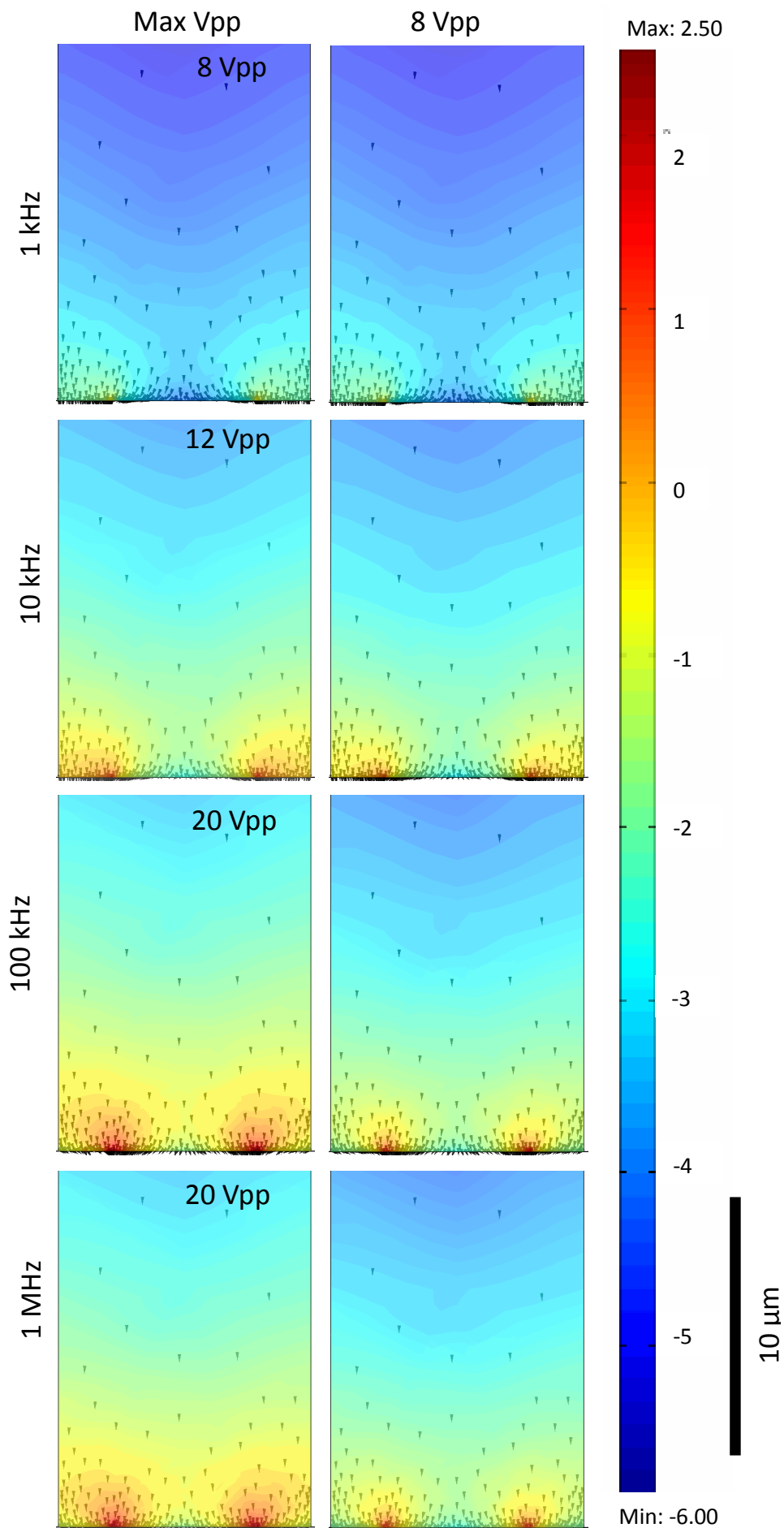
Figure 28: DEP terminal velocity vectors and magnitude plots on Plane 19, the plane intersecting the electrode tips extending 80 um from the electrode surface. The colour represents the magnitude of flow, plotted on a log scale, ranging from 10^2.5 m/s to 10^-8.5 m/s. The arrows represent the direction of flow. The maximum operation voltage for the given frequency were determined experimentally, and are indicated.

5.5 Electrothermal Flow Velocity

The electrothermal flow is dependent mainly on temperature gradients within the fluid. These temperature gradients cause differences in electrical properties, which result in an imbalance of forces on the liquid. Within this system, the temperature gradient is caused by joule heating through an alternating current. Thus, the electrothermal flow would directly be affected by the operating conditions. From the theory, the highest flowrates are to be expected in areas with a high electric field and temperature gradients.

With various frequencies, the electric field and temperature gradients will change due to shielding effects. As the shielding on the electrodes changes, the changes in current distribution will affect the areas that are joule heated, as well as the distribution in the electric field. This will result in a change in the flow patterns. Details are listed in the appendix. (A7) At 1 kHz, the flow points away from the electrode tips and towards the larger area of the electrodes. This can be seen in Figure 29, and in Figure 30, where the flow is pointed upwards and away from the tips.

At 10 kHz and 100 kHz, the flow can be separated into two sections: the section heading towards the electrode tips, and the section heading towards the larger area of the electrodes. This is seen as a U-shaped stagnation zone in Figure 29. As the voltage increases at the same frequency, the magnitudes of the flow also increases but the flow pattern stays consistent. (Figure 29)

The difference between the flow at 10 kHz, and 100 kHz can be distinguished in Figure 30. At 100 kHz, the flow curves up after flowing downwards.

At 1 MHz, the flow is reversed at the electrode tips (Figure 30), flowing upwards rather than downwards. Combined with the flow close the surface displayed in Figure 29, the electrothermal flow would flow towards the tips close to the surface, then upwards at the tips.

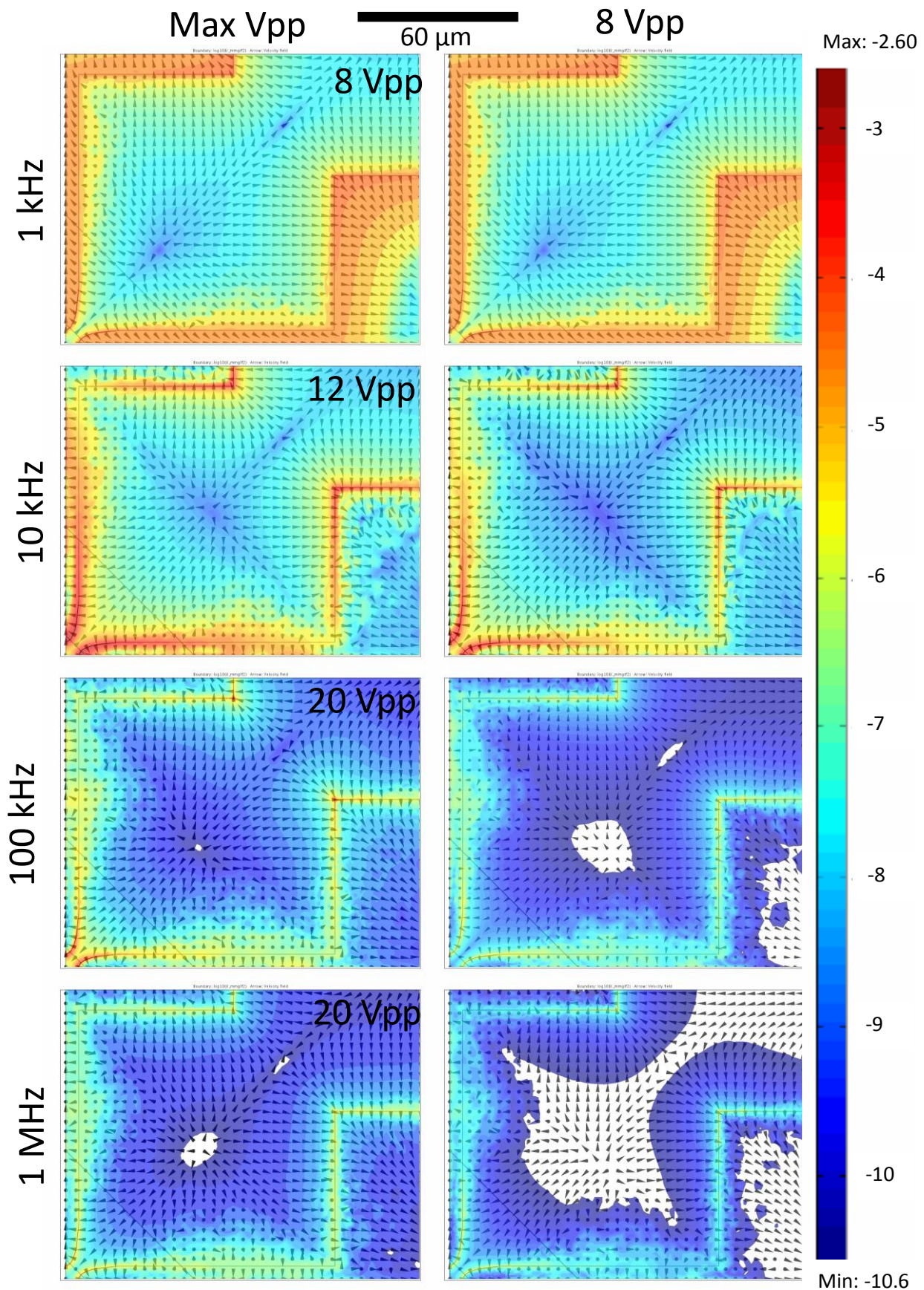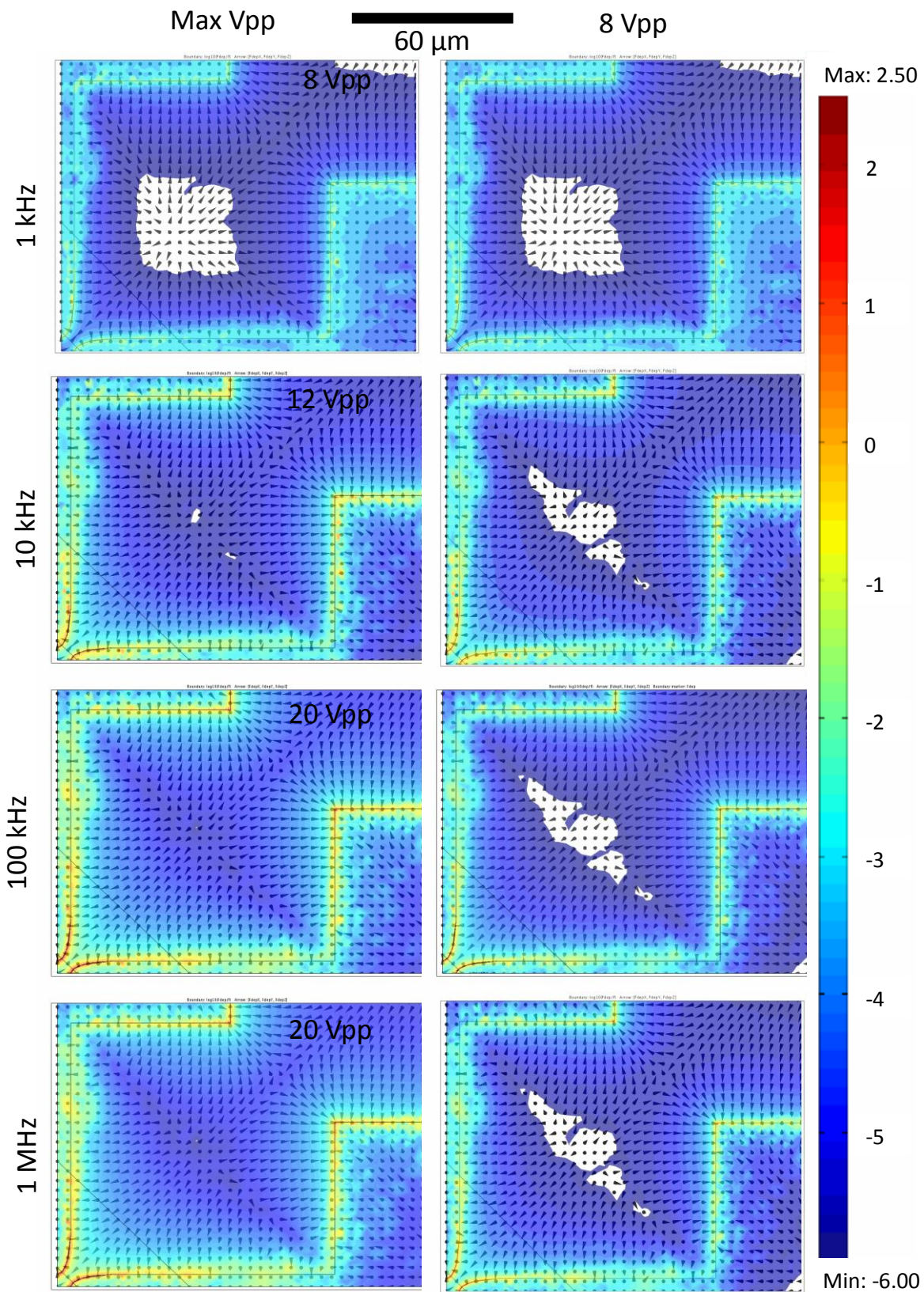*Figure 29: Electrothermal fluid flow on the electrode, and adjacent surfaces. The colour represents the magnitude of flow, plotted on a log10 scale, ranging from 10^-4.1 m/s to 10^-11.5 m/s. The arrows represent the direction of flow. Different operation conditions were shown, with the frequency ranging from 1 kHz to 1 MHz, and the voltage ranging from 8 Vpp to 20 Vpp. The maximum operation voltage for the given frequency were determined experimentally, and are indicated. The colour scale was truncated to better show contrast between operating conditions.*

Figure 30: ET fluid velocity vectors and magnitude plots on Plane 19, the plane intersecting the electrode tips extending 80 um from the electrode surface. The colour represents the magnitude of flow, plotted on a log scale, ranging from 10^-4.1 m/s to 10^-9.5 m/s. The arrows represent the direction of flow. Different operation conditions were shown, with the frequency ranging from 1 kHz to 1 MHz, and the voltage ranging from 8 Vpp to 20 Vpp.

5.6 Net Particle Velocity

The vector field of the net particle velocity are the sum of the electroosmotic flow vectors, the electrothermal flow vectors, and the equivalent velocity of the DEP flow vectors. Comparing the flow patterns and magnitude distributions in Figure 31 and Figure 32 with the figures depicting DEP velocities (Figure 27, Figure 28), it can be seen that the DEP force causes the majority of the net flow close to the surface.

Beyond the surface of the liquid, pathlines were used to visualize particle flow. (Figure 33, Figure 34) These pathlines were plotted using the streamline function in COMSOL, where curves tangent to the velocity was plotted. However, these massless particle would also experience the dielectrophoretic force, in addition to fluid flow. But since they are massless, these particles would instantaneously accelerate to a terminal velocity. This property would make massless particles easy to track under steady state conditions, as its pathline could be plotted by finding the curves tangent to the sum of the fluid velocity, and terminal velocity.

Although plotting pathlines evenly distributed over the liquid would not give specific information as to the capture of bacteria, it would give a qualitative understanding of the path of the bacteria under various frequencies to aid in future microelectrode designs. Since the effects of voltage on particle flow patterns cannot be distinguished on this scale, plots were made for frequencies ranging from 1 kHz to 1 MHz at 8Vpp.

The net particle flow is mainly the sum of two driving forces: the electro-osmotic flow, and the dielectrophoretic force. The ACEO flow is responsible for most of the horizontal flow components in the X-Y plane, while the DEP flow is mainly responsible for the vertical components. Compared to the surface plots, where the flow profiles are closely related to DEP velocity vectors at all operating

conditions, the pathlines suggest that beyond the surface, the particle flow patterns follow ACEO fluid flow at lower frequencies, and DEP velocity vectors at higher frequencies.

Referring to Figure 33, At 1 kHz, the velocity vectors are seen to point into the page from the center of the model towards the electrode tips, then outwards along the electrodes. Closer to the surface, the flow becomes vertical, and points downwards under the influence of the DEP force. As the frequency increases to 10 kHz, the flow changes to flow over the left electrode towards the tips, and away from the tips towards the right electrode. The vertical component closer to the surface extends further upwards. When the frequency increases to 100 kHz, and 1 MHz, the vertical component becomes increasing larger, while the horizontal flow pattern stays the same.
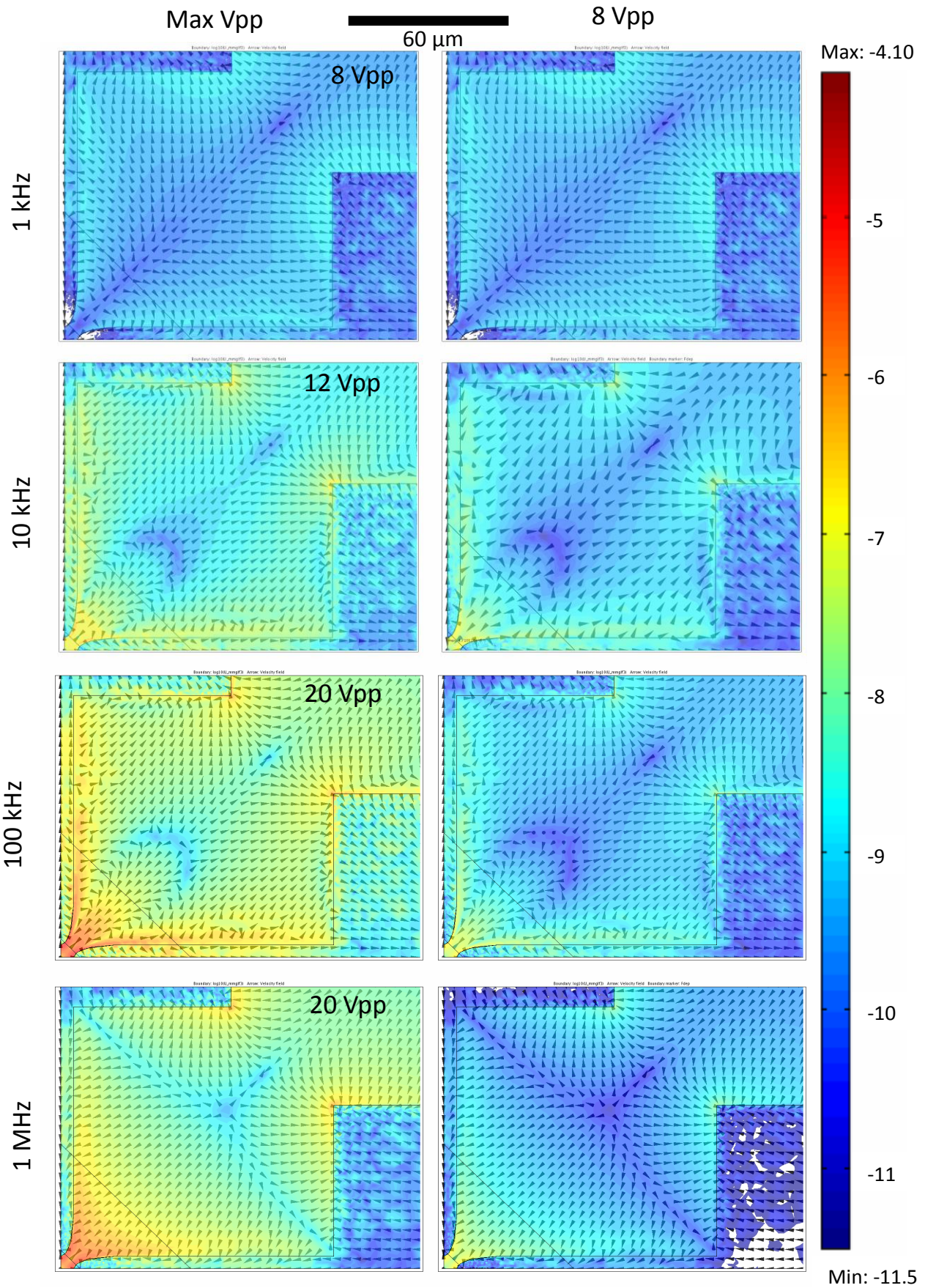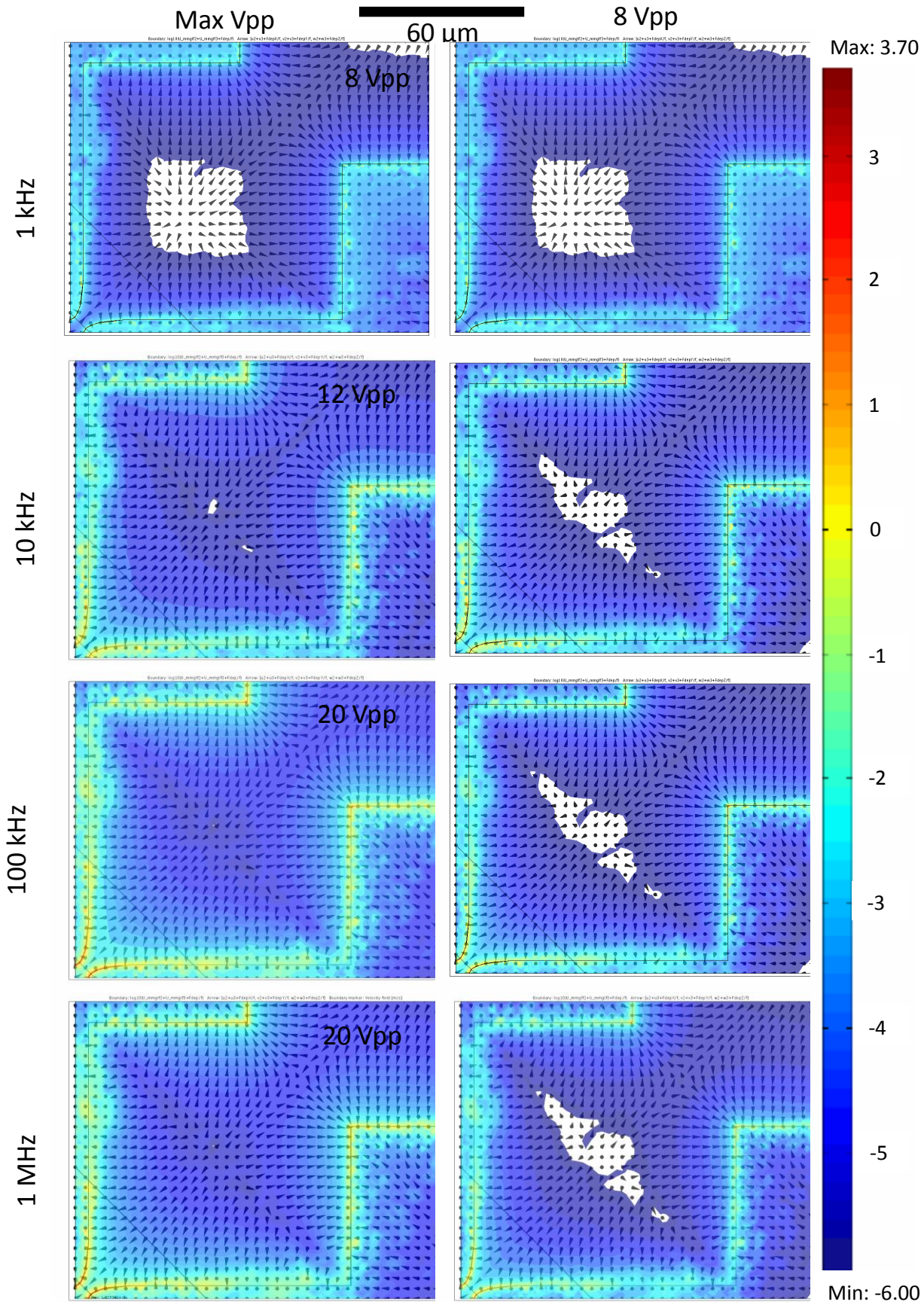
Figure 31: Net flow on the electrode, and adjacent surfaces. The colour represents the magnitude of flow, plotted on a log10 scale, ranging from 10^3.7 m/s to 10^-6 m/s. The arrows represent the direction of flow. Different operation conditions were shown, with the frequency ranging from 1 kHz to 1 MHz, and the voltage ranging from 8 Vpp to 20 Vpp. The maximum operation voltage for the given frequency were determined experimentally, and are indicated. The colour scale was truncated to better show contrast between operating conditions.
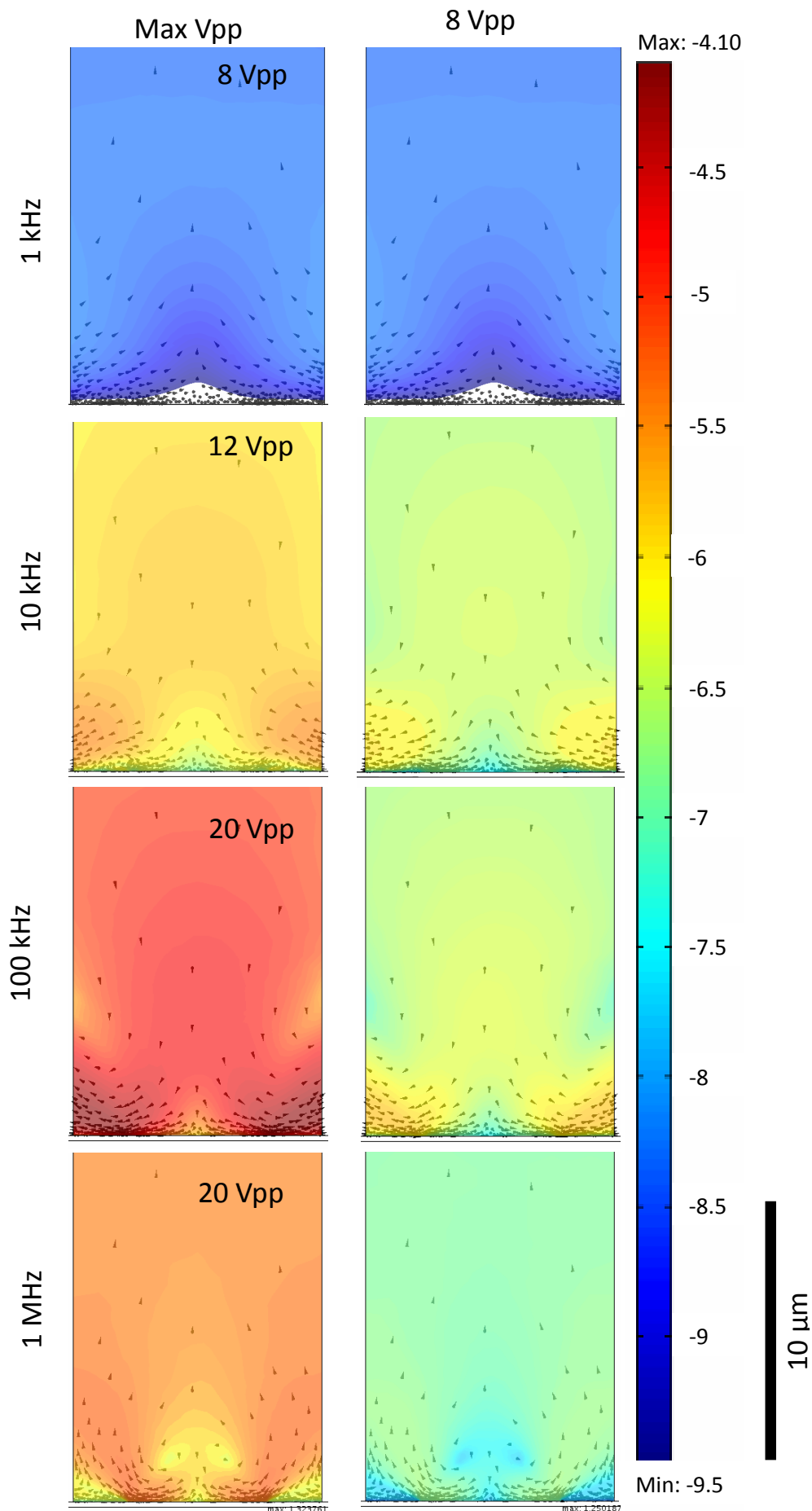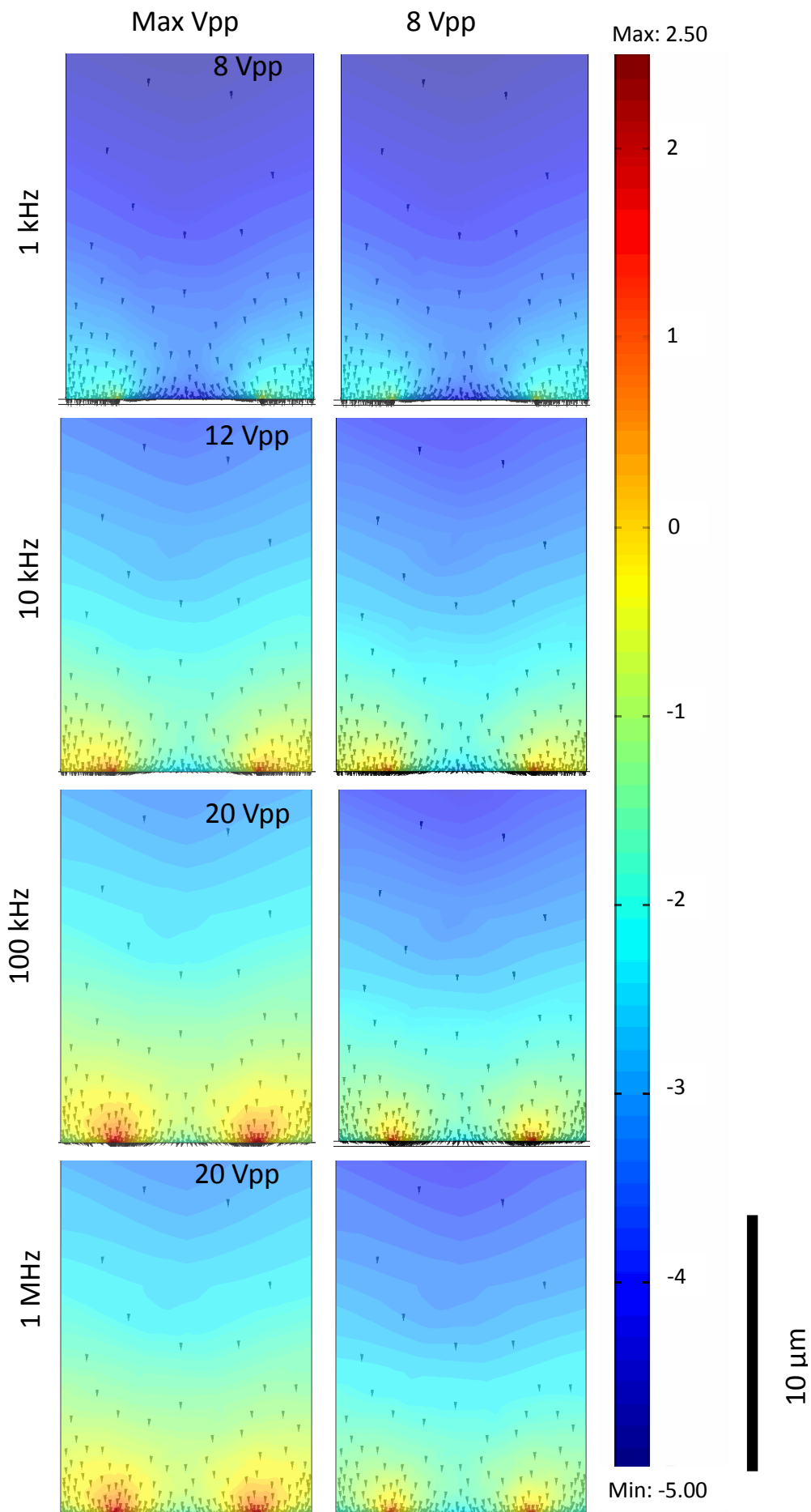
Figure 32: Net velocity vectors and magnitude plots on Plane 19, the plane intersecting the electrode tips extending 80 um from the electrode surface. The colour represents the magnitude of flow, plotted on a log scale, ranging from 10^2.5 m/s to 10^-8.5 m/s. The arrows represent the direction of flow. Different operation conditions were shown, with the frequency ranging from 1 kHz to 1 MHz, and the voltage ranging from 8 Vpp to 20 Vpp. The maximum operation voltage for the given frequency were determined experimentally, and are indicated.
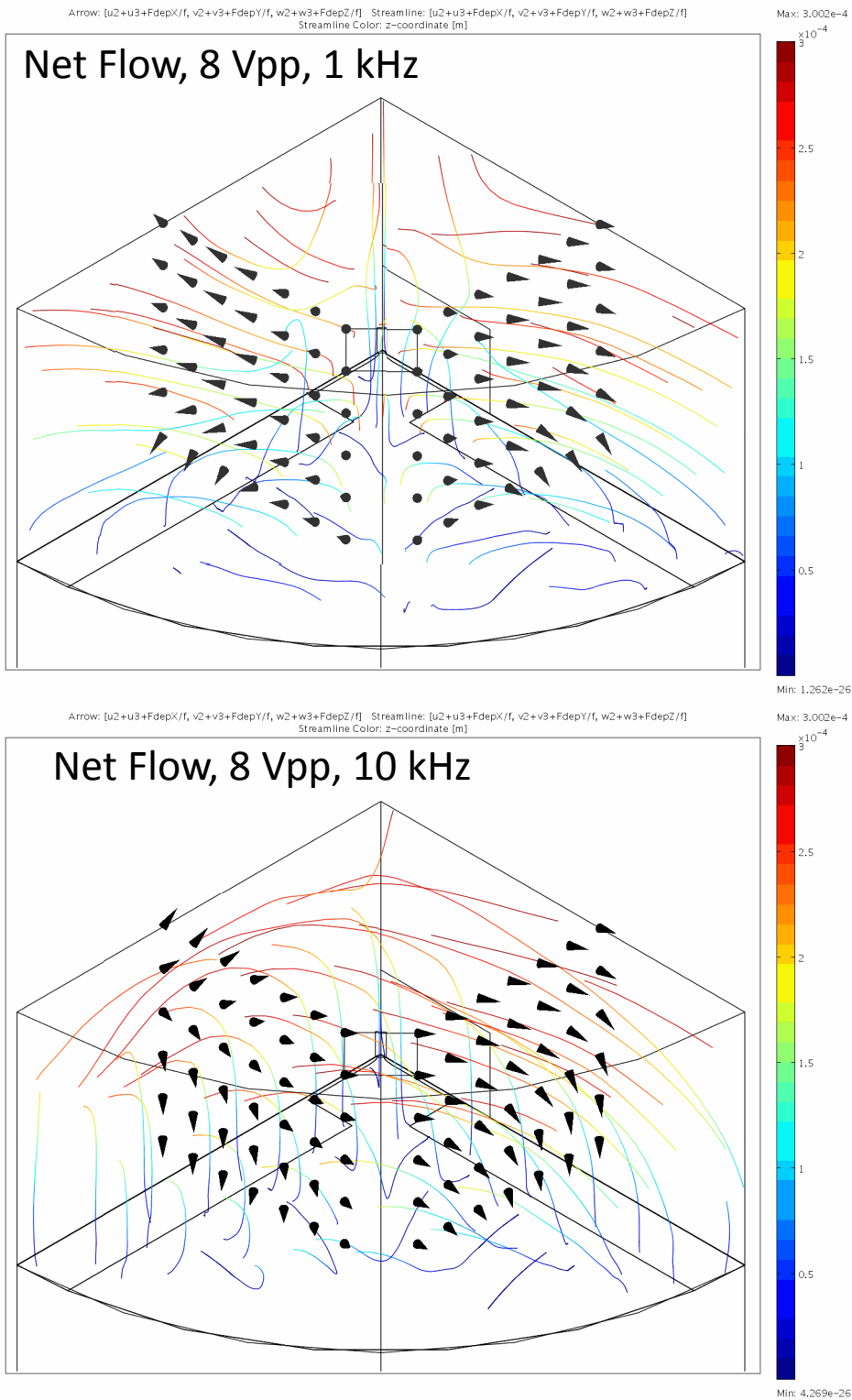
Figure 33: Pathlines depicting net flow for the operation conditions 8Vpp 1 kHz, and 8Vpp 10 kHz. The colour represents the height of the pathline in meters relative to the surface for ease of differentiating between pathlines. Two planes of arrows were added to infer the direction of flow along the pathlines.
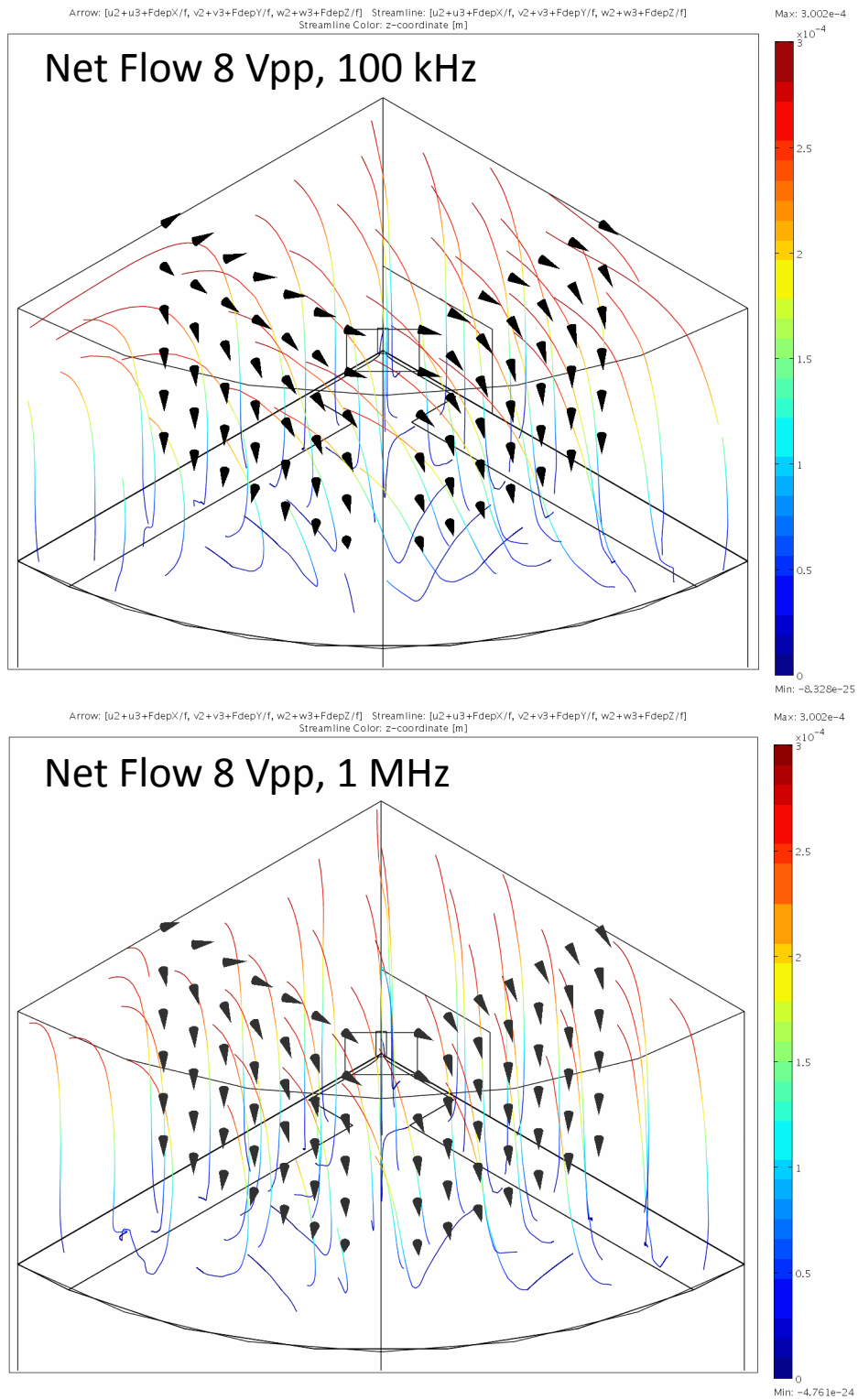
Figure 34: pathlines depicting net flow for the operation conditions 8Vpp 1 kHz, and 8Vpp 10 kHz. The colour represents the height of the pathline in meters relative to the surface for ease of differentiating between pathlines. Two planes of arrows were added to infer the direction of the flow.

5.7 Impact of Flow on Bacteria Capture

It was discussed in section 3.6.6 that the present velocity and acceleration of the bacteria was on timescales slow enough such that inertial effects could be negated, allowing the tracing of its movements as a massless particle. And by doing so allows for the analysis of the effectiveness of each operating condition in capturing bacteria. Unlike previous sections which focus on correlating simulation results with the theory, the current section tries to correlate simulation results with experimental results.

100 pathlines were plotted, originating from a 10 µm x 10 µm plane and extending in either direction. This plane is located 1 µm above the silica surface. This distance was chosen to represent the length scale of an E.coli cell. By examining and comparing the volume covered by the pathlines, an estimate could be made of the amount of bacteria captured, and bacteria trajectories would not have to be deducted by analysing vector fields.

However, there are limitations when it comes to accurate modeling of bacteria motion, besides inertia effects. If the bacterium's velocity is too slow, it would be statistically insignificant compared to Brownian motion, and any projection of its trajectory would be inaccurate. In addition, the time scale for bacteria capture is set to be 15 minutes. If the bacteria do not reach the end of its pathline by 15 minutes, it would not be considered captured.

To make clear these limitations, markers were drawn on the plots. Volumes where the velocity falls below the statistically significant velocity are highlighted green. And lines were drawn to mark off the parts of the pathlines which would take the bacteria longer than 15 minutes to reach the capture point. (Figure 35)

Figure 35: Pathline plots of bacteria trajectories for each operating condition. The pathlines are coloured to indicate the percentage contribution of the DEP force. Green volumes indicate the areas where bacteria velocities are below 99% significance. Volumes below the red mark indicate the relevant volumes that would be affected within a time period of 15 minutes.

Referring to Figure 35, there can be a trend found between the volume traced out by the bundle of pathlines, and the amount of bacteria captured. Looking at the three operating conditions, at 8 Vpp and 1 kHz, 12 Vpp, and 10 kHz, and 20 Vpp and 100 kHz, the volume traced out by the bundle of pathlines can be seen to be significantly greater than the other four operating conditions, and consequentially, the amount of bacteria captured is also seen to be greater. However, looking at the three operating conditions, it can be seen that even though 12 Vpp and 10 kHz would have the least volume drawn out out of the three, it also has the most amount of bacteria captured. This could be explained by looking at the surface.

After bacteria are drawn close to the surface, a force would have to initiate their capture. Particle tracking via pathlines close to the surface becomes less accurate due to increased velocities, and the momentum of the bacteria would have to be taken into account. Plotted in Figure 37, are areas where the downwards net force resulted in a greater friction force opposing the tangential force. Net force vectors were then overlaid on top of the coloured areas, allow for the analysis and interpretation of the movement of bacteria on the surface, where the coloured areas indicate where the bacteria would slow down upon touching the surface, due to friction. The friction coefficient was treated as an empirical value and adjusted until the coloured area matched the area where bacteria were captured at 12 Vpp and 10 kHz.

Referring to Figure 36, From analysing these plots, it can be seen that at 12 Vpp and 10 kHz, the net force pushes the bacteria directly to areas of high friction, leading bacteria to accumulate over the electrode tips. Eventually, enough bacteria would accumulate on the electrodes to bridge the gap between the electrodes.

Contrasting with 8Vpp and 1 kHz, the bacteria do bridge the gap between the electrodes, but no bacteria are accumulated on top of the electrodes. The model suggests that the force saddle point

between the electrodes slows the bacteria enough for some to accumulate between the electrodes. But this is not as efficient as the capture conditions seen in 12 Vpp and 10 kHz, despite these conditions affecting a larger volume.

At 20 Vpp and 100 kHz, the net force would accumulate the bacteria at the edges of the electrode. However, the area with significant friction forces at those edges are minimal, and relatively little bacteria is retained.

It should be noted that due to the antibody functionalization, the bacteria would be captured on the surface when its velocity falls below a certain value. So, for conditions where the tangential velocity close to the surface is relatively low, the bacteria do not follow the expected capture patterns, as seen for 8 Vpp 10 kHz, and 8 Vpp 100 kHz. (Figure 37) Also seen are a lot of bacteria landing at the center point between the two electrodes. This is due to a decrease in velocity at the force saddle point in that region.

In addition to the affected volume of bacteria, the mechanism of bacteria retention should also be observed. Bacteria would gather in areas of low velocity such as the saddle points between the electrodes, the electrode edges, where a large downwards DEP force causes higher friction, and in certain cases, on top of the electrodes. Though in general, the case where high friction is observed over the electrode tips tends to retain more bacteria than other cases.
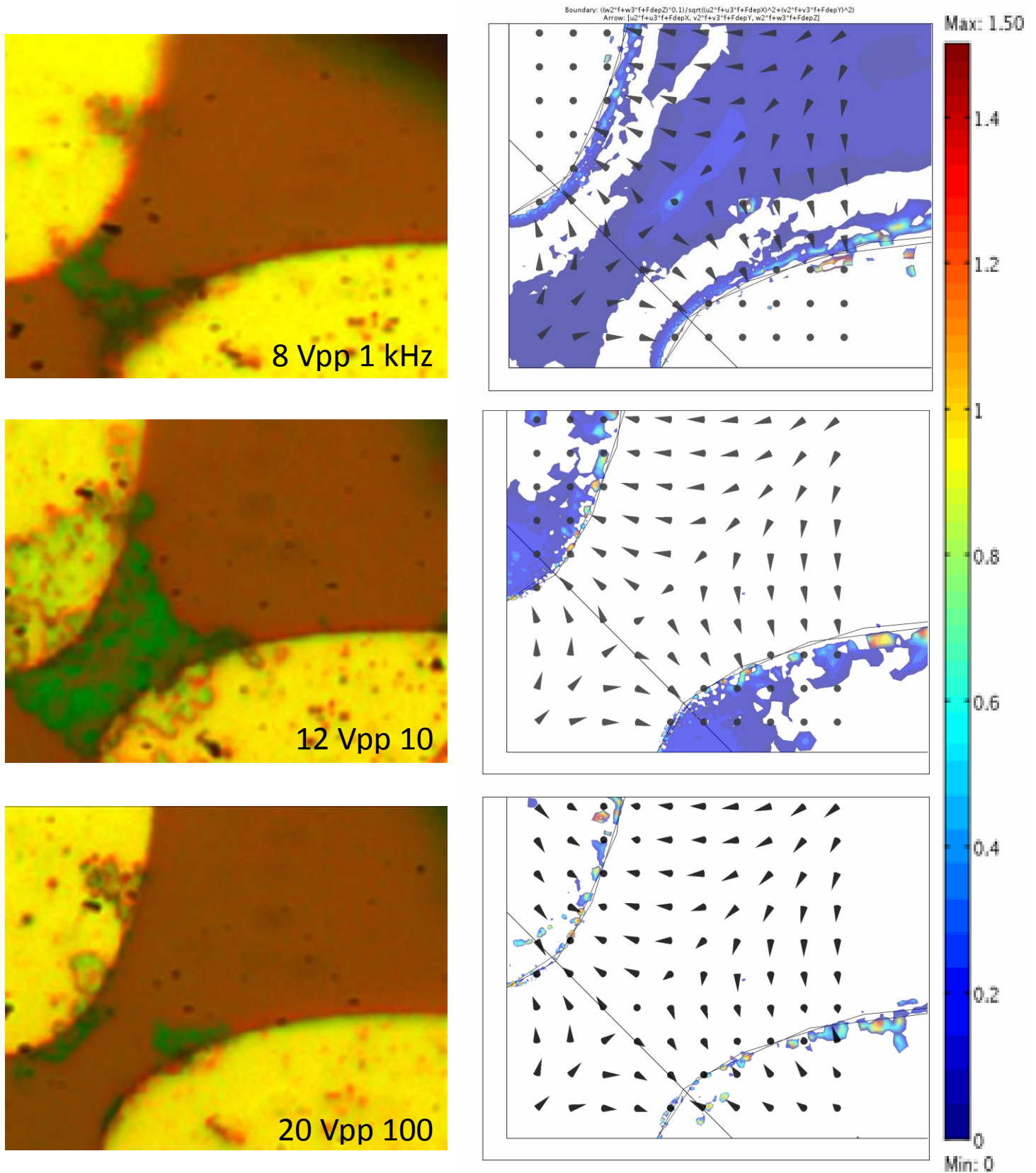
Figure 36: Plotted are the areas on the surface of the electrode where the ratio of the friction force to the tangential component of the net force is greater than 1, for a friction coefficient of 0.1. The friction coefficient was varied until the coloured area for 12 Vpp and 10 kHz resembled the area where bacteria were shown to be captured. The coloured area did not display any significant change between the friction coefficients of 0.1 and 0.8.

8 Vpp 10

8 Vpp 100 kHz
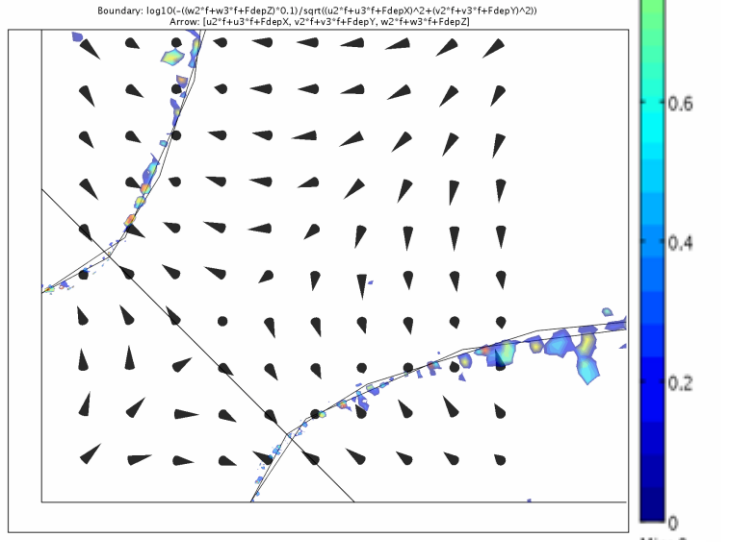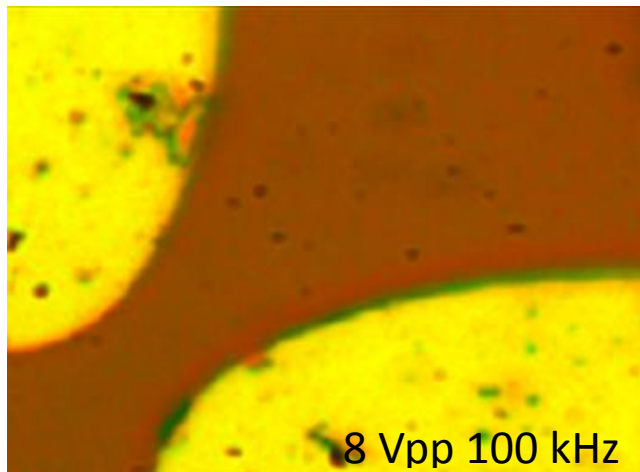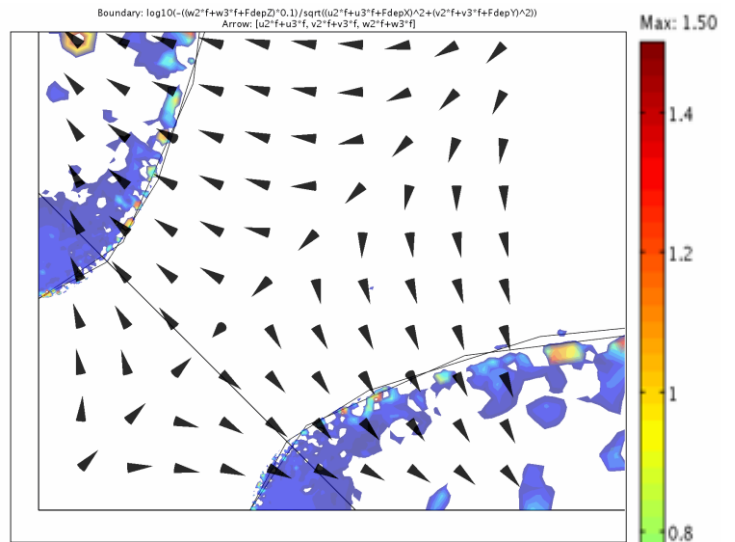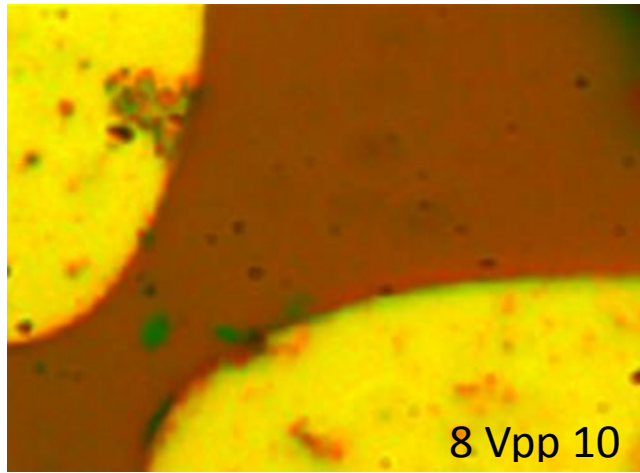
Figure 37: Plotted are the areas on the surface of the electrode where the ratio of the friction force to the tangential component of the net force is greater than 1, for a friction coefficient of 0.1. The friction coefficient was varied until the coloured area for 12 Vpp and 10 kHz resembled the area where bacteria was shown to be captured. The coloured area did not display any significant change between the friction coefficients of 0.1 and 0.8.

6.0 Conclusions and Recommendations

Rapid diagnosis of pathogens requires the ability to detect the presence of a target in a sample at very low loadings. In this thesis, a simple, sensitive and label-free, surface based, method for bacterial detection is presented with the potential to meet this goal. The method combines three key features, namely, (a) accelerated transportation to, and focusing of bacteria on, the detection surface by means of alternating current (AC) electrokinetic effects, (b) selective capture of the target microorganism using surface-immobilized antibodies, and (c) sensitive detection of target bacteria with micro-Raman spectroscopy. The non-uniform electric field is created by an AC signal-driven planar, quadrupolar, gold microelectrode array that is deposited on the detection surface (oxidized silicon wafer). AC electroosmosis and dielectrophoresis combine to produce the desired concentration amplification of bacteria on the capture surface within a few minutes. Bacterial detection is, subsequently, accomplished through Raman spectra acquired at pre-determined locations near the electrodes after sample removal and rinsing of the capture surface. Using this technique, detection of *Escherichia coli* K12 (target microorganism) at concentrations as low as 10^2 bacteria per mL was reproducibly achieved from 50 μL sample droplets. This is impressive considering that a sample droplet of 50 μL in size contains a total of roughly 5 bacteria. In fact, the method is sensitive enough to detect the capture of a single bacterium.

The bacterial capture efficiency ("sampling") was found to be very sensitive to the selection of the applied voltage and AC frequency values. Tests performed in the range 1-20 V_{pp} and 1 kHz-1 MHz showed that the most effective combination by a wide margin was (12 V_{pp}, 10 kHz). Overall, high bacteria capture efficiencies were observed at low frequencies, which underlines the key role of electroosmosis on the transport and focusing of bacteria. However, it was also found experimentally that low frequencies impose a limitation on the value of the potential difference that can be applied without causing microelectrode damage.

The ability to achieve localized concentration amplification of the target agent in areas of only a few μm^2 using specially designed microelectrodes makes micro-Raman spectroscopy a sensitive and efficient tool for biosensing. Moreover, monoculture and mixed populations experiments demonstrated that microelectrode functionalized with anti-*E.coli* imparted selectivity to the detection process, evidence by the much higher capture rate (and stronger Raman signal) of target bacteria compared to non-target *M. luteus*. The selectivity of the present method can be further improved with the use of monoclonal antibodies and by employing an immobilization method that substantially increases antibody surface density.

The capabilities of the presently described method can extend beyond detection to bacterial identification, if combined with multivariate statistical analysis. Moreover, dielectrophoretic trapping and SERS can possibly be combined towards the chemical surveillance of individual bacteria or bacterial aggregates in microfluidic environments. SERS would also allow for faster scanning using Raman spectroscopy of the surface, which would increase reliability of the chip. Finally, the presently described method can be used with a water immersion lens to eliminate the washing and drying steps, or in flow-through microfluidic systems for online sample monitoring.

Simulations were then performed in an effort to understand how the electrokinetic phenomena would change with varying frequency and voltage. Increasing the voltage was shown to have a positive effect, increasing the velocity of DEP, ACEO, and ET flow. Changing the frequency had an effect on the net flow pattern. At lower frequencies, it was shown that the flow patterns were similar to ACEO, and that the fluid would act as a conveyor belt, pulling the bacteria towards the electrode tips. At higher frequencies, the bacteria experienced a proportionally higher DEP force, and were pulled straight downwards. However, at higher frequencies, higher voltages, and thus velocities, were allowed. By comparing simulation results with experimental results, the capture of bacteria was shown to be a function of the affected volume and the pattern of the relatively high areas of friction on the electrodes. At 8 Vpp 1 kHz,

and 20 Vpp 100 kHz, the affected volume was maximized, but the friction areas on the electrodes were not ideal. Although 12 Vpp 10 kHz did not have a high affected volume, the areas of high friction were wide and were focused at the force wells, leading to the accumulation of bacteria in those areas.

Methods to test the potency of the antibodies must be required in order to improve functionalization procedures and to improve antibody shelf-life when functionalized surfaces are stored. Furthermore, tests using a miniaturized Raman spectroscopy system would also be necessary. These devices produce weaker signals compared to the scaled up models, and methods would need to be developed to compensate for this. One would be to use SERS to enhance the Raman signal for detection. The detection limit could be lowered further through the use of micro-channels. Similar to flow cytometry, sequential flow of bacteria past an electrokinetic capture device would allow for larger sample volumes to be processed, which would be necessary for concentrations down to 10^{-2} CFU/mL.

The simulations could be made more accurate by having a denser mesh, and accounting for the orientation of the bacteria with respect to flow. Currently, the friction factor is being approximated as a constant, but a more accurate representation would be a function of the orientation of the bacteria with respect to the fluid velocity. This is not a simple task, and would warrant an entire chapter by itself. Also, despite symmetrical electrode geometries, the flow was found to be asymmetrical as a result of the magnitudes on one of the electrodes being slightly larger than the other electrode due to amplified errors in calculating significantly small velocities. This is a consequence of having a not dense enough mesh, which could be fixed, given more computing power. Alternatively, half of the model could be simulated, while increasing mesh density or decreasing required processing power, at the cost of forcing symmetry.

SERS could be used in conjunction with the above techniques to further lower the detection limit, and even make detection of viruses possible. However, the dielectrophoretic force would be negligible

compared to the Stokes force, and a new electrode design would be required that could bring the

viruses into the range of capture.

References

[1] BCC Research, "The U.S. Market for Biodefense-Related Rapid Pathogen Identification and Treatments," GII Research, 2015.

[2] D. A. C. E. R. E Nester, Microbiology: A Human Perspective, McGraw Hill, 2008.

[3] H. M. Shapiro, "Multistation multiparameter flow cytometry: A critical review and rationale," *Cytometry,* vol. 3, no. 4, pp. 227-243, 1983.

[4] M. B. S. R. P. M. C. O. P. v. R. M. S. J. B. I. B. D. A. D. K. B. Hoffman, "A review of RT-PCR technologies used in veterinary virology and disease control: Sensitive and specific diagnosis of five livestock diseases notifiable to the World Organisation for Animal Health," *Veterinary Microbiology,* vol. 139, no. 1, pp. 1-23, 2009.

[5] Corgenix, "ReEBOV(TM) Antigen Rapid Test (Ebolavirus VP40 Antigen Detection) Instructions for Use," 11 March 2015. [Online]. Available: ftp://ftp.corgenix.com/Intra/ReEBOV/14005.pdf. [Accessed 18 August 2015].

[6] A. R. A. G. H. M. A. C. N. G. Green, "Fluid Flow induced by nonuniform AC Electric Fields in Electrolytes on Microelectrodes III Observations of Streamlines and Numerical Simulation," *Physcal Review,* vol. 66, no. 026305\, pp. 0263051-02630511, 2002.

[7] L. Y. Y. Hsueh-Chia Chang, Electrokinetically Driven Microfluidics and Nanofluidics, New York: Cambridge University Press, 2010.

[8] V. Freise, "Zur Theorie der diffusen Doppelschicht," *Zeitschrift für Elektrochemie,* vol. 56, no. 8, pp. 822-827, 1952.

[9] H. Pohl, "The Motion and Precipitation of Suspensoids in Divergent Electric Fields," *Journal of Applied Physics,* vol. 22, no. 7, pp. 869-871, 1951.

[10] H. Pohl, "Some Effects of Nonuniform Fields on Dielectrics," *Journal of Applied Physics,* vol. 29, no. 8, pp. 1182-1188, 1958.

[11] K. Asami, W. Bai and K. Zhao, "Dielectric properties of E. coli cell as simulated by the three-shell sheroidal model," *Biophysical Chemistry,* no. 122, pp. 136-142, 2006.

[12] A. R. A. G. H. M. a. A. C. N. G. Green, "Fluid flow induced by nonuniform ac electric fields in electrolytes on microelectrodes. III. Observation of streamlines and numerical simulation," *Physical Review E,* vol. 88, no. 2, pp. 0263051-02630511, 2002.

[13] A. R. P. Garcia-Sanchez, "The effect of electrode height on the performance of traveling wave electroosmotic pumps," *Microfluidics and Nanofluidics,* vol. 5, no. 3, pp. 307-312, 2008.

[14] D. M. M. B. R. Morrow, "The Time-Dependent Development of Electrical Double-Layers in Saline

Solutions," *Journal of Physics D: Applied Physics,* vol. 39, pp. 937-943, 2006.

[15] A. P. Y. C. A. A. Vincent Studer, "An integrated AC electrokinetic pump in a microfluidic loop for fast and tunable control," *The Analyst,* vol. 129, no. 10, pp. 944-949, 2004.

[16] C. S. A. R. A.B.D. Brown, "Pumping of water with ac electric fields applied to asymmetric pairs of microelectrodes," *Physical Review E,* vol. 63, pp. 0163051-0163058, 2000.

[17] C. M. M.R. Bown, "AC electroosmotic flow in a DNA concentrator," *Microfluidics and Nanofluidics,* vol. 2, no. 6, pp. 513-523, 2006.

[18] A. R. N. G. H. M. P. Garcia-Senchz, "Experiments on pumping of liquids using arrays of microelectrodes subjected to travelling wave potentials," *Electrostatics,* vol. 142, pp. 0120551-0120556, 2007.

[19] M. H. A. C. N. H. M. M. K.F. Hoettges, "Optimizing Particle Collection for Enhanced Surface-Based Biosensors," *Micro and Nano Electrokinetics,* vol. 22, no. 6, pp. 68-74, 2003.

[20] B. M. K. G. S. G. O. V. E.M. Melvin, "On-chip collection of particles and cells by AC electroosmotic pumping and dielectrophoresis using asymmetric microelectrodes," *Biomicrofluidics,* vol. 5, no. 034113, pp. 1-16, 2011.

[21] S. S. X. C. S. B. H. C. I. Cheng, "A rapid field-use assay for mismatch number and location of hybridized DNA," *Lab on a Chip,* vol. 10, pp. 828-831, 2010.

[22] H. C. D. H. H. C. I. Cheng, "An integrated dielectrophoretic chip for continuous bioparticle filtering, focusing, sorting, trapping, and detecting," *Biomicrofluidics,* vol. 1, no. 021503, pp. 1-15, 2007.

[23] A. E. C. M. A. J. J. S. M. Castellarnau, "Dielectrophoresis as a Tool to Characterize and Differentiate Isogenic Mutants of Escherichia coli," *Biophysical Journal,* vol. 91, pp. 3937-3845, 2006.

[24] T. P. H. ·. R. M. Westervelt, "Dielectrophoresis tweezers for single cell manipulation," *Biomed Microdevices,* vol. 8, no. 3, pp. 227-230, 2006.

[25] D. L. A. D. M.R. Tomkins, "Accelerated Detection of Viral Particles by Combining AC Electric Field Effects and Micro-Raman Spectroscopy," *Sensors,* vol. 15, no. 1, pp. 1047-1059, 2015.

[26] J. R. J. R. E. R. K. H. P. H. K. K. P. O. Y. M. E.L. Carpenter, "Dielectrophoretic capture and genetic analysis of single neuoblastoma tumor cells," *Frontiers in Oncology,* vol. 4, no. 201, pp. 1-14, 2014.

[27] Silicon Biosystems, "Silicon Biosystems, A Menarini Group Company - Home," Menarini, 31 12 2013. [Online]. Available: http://www.siliconbiosystems.com/. [Accessed 17 3 2015].

[28] L. F. N. H. F. B. M. F.-R. S. Menad, "nDEP-driven cell patterning and bottom-up construction of cell aggregates using a new bioelectronic chip," *Acta Biomaterialia,* 2015 (not yet published).

[29] F. Z. C.F. Chou, "Electrodeless Dielectrophoresis for Micro Total Analysis Systems," *Micro &*

Nanoelectrokinetics, vol. 22, no. 6, pp. 62-67, 2004.

[30] J. V. N. Gadish, "High-Throughput Positive-Dielectrophoretic Bioparticle Microconcentrator," *Analytical Chemistry,* vol. 78, no. 22, pp. 7870-7876, 2006.

[31] M. D. P. a. M. A. Hayes, "Electrophoretic and Dielectrophoretic Field Gradient Technique for Separating Bioparticles," *Analytical Chemistry,* vol. 79, no. 12, pp. 4552-4557, 2007.

[32] L. Yang, "Dielectrophoresis assisted immuno-capture and detection of foodborne pathogenic bacteria in biochips," *Talanta,* vol. 80, no. 2, pp. 551-558, 2009.

[33] C. C. V. R. V. C. N. Swami, "Enhancing DNA hybridization kinetics through constriction-based dielectrophoresis," *Lab on a Chip,* vol. 9, pp. 3212-3220, 2009.

[34] M. X. P. X. Y. X. W. D. D. Cai, "An integrated microfluidic device utilizing dielectrophoresis and multiplex array PCRfor point-of-care detection of pathogens," *Lab on a Chip,* vol. 14, pp. 3917-3924, 2014.

[35] D. K. M. F. C. Schäfer, "Capturing molecules with plasmonic nanotips in microfluidic channels by dielectrophoresis," *Lab on a Chip,* vol. 15, pp. 1066-1071, 2015.

[36] L. Y. Xiaoxing Xing, "Dielectrophoretic isolation of cells using 3D microelectrodes featuring castellated blocks," *Analyst,* vol. 140, no. 10, pp. 3397-3405, 2015.

[37] M. R.-C. B. L.-E. A. LaLonde, "Assessment of cell viability after manipulation with insulator-based dielectrophoresis," *Electrophoresis,* vol. 35, pp. 1-6, 2014.

[38] E. P. Diamandis, "Analytical methodology for immunoassays and DNA hybridization assays - Current status and selected systems - Critical Review," *Clinica Chlmica Acfa,* vol. 194, pp. 19-50, 1990.

[39] L. D. S. W. N.B. Colthup, Introduction to Infared and Raman Spectroscopy, Boston: Academic Press Inc, 1990.

[40] P. B. S. H. J. L. G. Naja, "Raman-based detection of bacteria using silver nanoparticles conjugated with antibodies," *The Analyst,* vol. 132, pp. 679-686, 2007.

[41] S. M. a. H.-C. C. Diana Hou, "Rapid bioparticle concentration and detection by combining a discharge driven vortex with surface enhanced Raman scattering," *Biomicrofluidics,* vol. 1, no. 014106, pp. 1-13, 2007.

[42] C. L. D. L. H. C. I.F. Cheng, "A dielectrophoretic chip with a roughened metal surface for on-chip surface-enhanced Raman scattering analysis of bacteria," *Biomicrofluidics,* vol. 4, no. 034104, pp. 1-11, 2010.

[43] M. M. E. D. A. Sengupta, "Detection of bacteria by surface-enhanced Raman spectroscopy," *Analytical Bioanalytical Chemistry,* vol. 386, p. 1379–1386, 2006.

[44] A. R. U. G. S. S. C. L. A. C. U. H. W. F. W. P. M. B. J. P. U. N. U.C. Schröder, "Combined Dielectrophoresis–Raman Setup for the Classification of Pathogens Recovered from the Urinary Tract," *Analytical Chemistry,* vol. 85, p. 10717–10724, 2013.

[45] A. S. S. S. R. P. I. E. C. A. P. C. D. J. J. D. E. Schultz, "A novel method for single bacteria identification by Raman identification by Raman," *Biomedical Vibrational Spectroscopy VI: Advances in Research and Industry,* vol. 8939, no. 89390D, pp. 1-14, 2014.

[46] R. G. I. T. M. B. A. W. W.E. Huang, "Raman Microscopic Analysis of Single Microbial Cells," *Analytical Chemistry,* vol. 76, no. 15, pp. 4452-4458, 2004.

[47] S. M. M. E. P. R. J. P. S. Stöckel, "Identification of Bacillus anthracis via Raman Spectroscopy and Chemometric Approaches," *Analytical Chemistry,* vol. 84, pp. 9873-9880, 2012.

[48] P. M. E. S. R. P. A. S. I. E. C. A. J. D. S.A. Strola, "Differentiating the growth phases of single bacteria using Raman spectroscopy," *Biomedical Vibrational Spectroscopy VI: Advances in Research and Industry,* vol. 8939, no. 893905, pp. 1-9, 2004.

[49] S. M. M. E. P. R. J. P. S. Stockel, "Raman Spectroscopic Detection of Anthrax Endospores in Powder Samples," *Spectroscopic Analysis,* vol. 51, pp. 5339-5342, 2012.

[50] D. Y. N. I. N. M. R. N. C. H. H. Zhou, "SERS Detection of Bacteria in Water by in Situ Coating with Ag Nanoparticles," *Analytical Chemistry,* vol. 86, pp. 1525-1533, 2014.

[51] H. N. K. T. Y. N. H. Yamada, "Charge-transfer band and sers mechanism for the pyridine-Ag system," *Surface Science,* vol. 182, no. 1-2, pp. 269-286, 1987.

[52] P. M. E. S. R. P. A. S. I. E. C. A. J. D. S.A. Strola, "Differentiating the growth phases of single bacteria using Raman spectroscopy," *Biomedical Vibrational Spectroscopy VI: Advances in Research and Industry,* vol. 8939, no. 893905, pp. 1-9, 2014.

[53] J. W. A. D. M.R. Tomkins, "Observations and analysis of electrokinetically driven particle trapping in planar microelectrode arrays," *The Canadian Journal of Chemical Engineering,* vol. 86, no. 4, pp. 609-621, 2008.

[54] S. Golchi, "Electrokinetically Enhanced Sampling of Bacteria in Planar Quadruplar Microelectrodes," Queen's Unversity, Kingstion, 2014.

[55] N. G. H. Morgan, AC Electrokinetics: Colloids and Nanoparticles, Research Studies Pr, 2002.

[56] A. P. Y. C. A. A. V. Studer, "An integrated AC electrokinetic pump in a microfluidic loop for fast and tunable flow control," *The Analyst,* vol. 129, pp. 944-949, 2004.

[57] A. L. Jurgen Blumm, "Characterization of the thermophysical properties of molten polymers and liquids using the flash technique," *High Temperatures - High Pressures,* vol. 36, pp. 627-632, 2007.

[58] A. L. Porta, "Deceleration of a particle in a resisting fluid with application to biological physics,"

September 2011. [Online]. Available: http://www2.physics.umd.edu/~alaporta/PHYS171_f12/lectures/ForceOfMotorProtein.pdf. [Accessed 23 Aug 2015].

[59] J. R. S. G. A. D. D.S. Liao, "Fast and sensitive detection of bacteria from a water droplet by means of electric field effects and micro-Raman spectroscopy," *Sensing and Bio-Sensing Research,* vol. 6, 2015.

[60] M. S. W. K. J. P. P. Rosch, "The identification of microorganisms by micro-Raman spectroscopy," *Journal of Molecular Structure,* no. 661, pp. 363-369, 2003.

[61] J. J. H. O.-Y. M.T. Wei, "Direct Measurements of the Frequency-Dependent Dielectrophoresis Force," *Biomicrofluididcs,* vol. 3, no. 012003, pp. 0120031-0120038, 2009.

[62] C. S. A. R. A.B.D. Brown, "Pumping of water with ac electric fields applied to asymmetric pairs of microelectrodes," *Physical Review E,* vol. 63, no. 016305, pp. 1-8, 2000.

[63] R. Hunter, Fundations of Colloid Science, Oxford: Oxford University Press, 2001.

Appendix

A1 – Clausius Mossotti (CM) factor as modeled by Asami *et al*

An *E. coli* bacterium is ellipsoidal in nature. Due to its dimensions, the CM factor will be different along each dimension. The CM factor of an ellipsoidal bacterium could be modeled as follows:

$$Ke_j = \frac{\frac{1}{3}(\varepsilon_{tj} - \varepsilon_m)}{\varepsilon_m + \alpha_j(\varepsilon_{tj} + \varepsilon_m)} \qquad \text{(Eq 39)}$$

Where ε_{tj} was the complex relative permittivity of the entire bacterium, j could represent x, y, or z, and α_j is the depolarization factor along each axis. The CM factor for a homogeneous ellipsoid also follows this form, but with ε_{tj} replaced by the dielectric constant of the medium.

The bacteria model is a three-shelled ellipsoid, for which the dielectric constant or complex relative permittivity could be described by ε_{tj}. Each of these shells has a unique dielectric constant, as determined by its composition. The general function for determining a homogeneous ellipsoid in a homogeneous medium could be used to sequentially calculate the effective complex permittivity of each layer, by assuming the sequential layer is the medium.
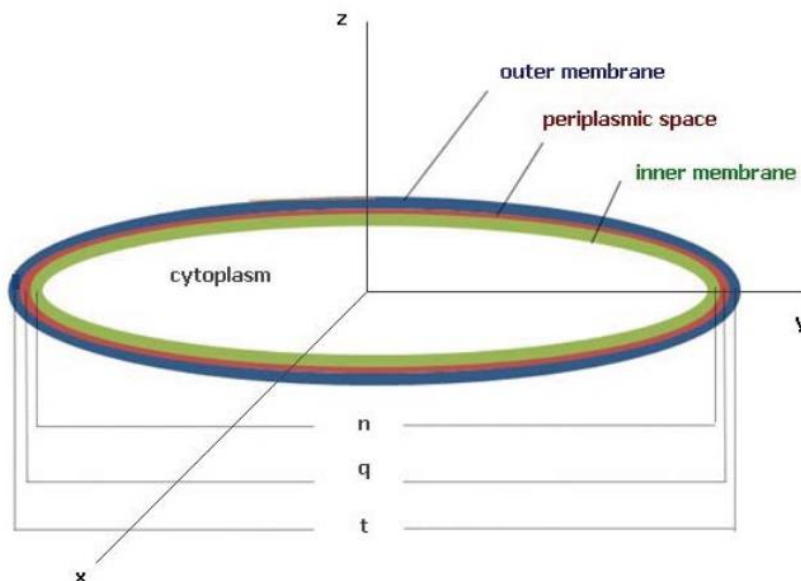
Then ε_{tj} is a function of the dielectric constant of the outer membrane (ε_{OM}), and ε_{qj}, the complex

relative permittivity of the composite containing the cytoplasm, inner membrane, and periplasmic space.

$$\varepsilon_{tj} = \frac{\varepsilon_{om}\big(\beta_j(1-v_1)\varepsilon_{om} + (1+\beta_j v_1)\varepsilon_{qj}\big)}{(\beta_j + v_1)\varepsilon_{om} + (1-v_1)\varepsilon_{qj}}$$ (Eq 40)

Similarly, ε_{qj} is dependent on the dielectric constant of the next layer, ε_{pp} and ε_{nj}, the complex relative

permittivity of the composite containing the cytoplasm, and inner membrane.

$$\varepsilon_{qj} = \frac{\varepsilon_{pp}\big(\beta_j(1-v_2)\varepsilon_{pp} + (1+\beta_j v_2)\varepsilon_{nj}\big)}{(\beta_j + v_2)\varepsilon_{pp} + (1-v_2)\varepsilon_{nj}}$$ (Eq 41)

And then, ε_{nj} is a function of ε_{im}, the dielectric constant for the inner membrane, and ε_{cp} which is the

dielectric constant for the cytoplasm.

$$\varepsilon_{nj} = \frac{\varepsilon_{im}\big(\beta_j(1-v_3)\varepsilon_{im} + (1+\beta_j v_3)\varepsilon_{cp}\big)}{(\beta_j + v_3)\varepsilon_{im} + (1-v_3)\varepsilon_{cp}}$$ (Eq 42)

And β_j is defined as:

$$\beta_j = \frac{1-\alpha_j}{\alpha_j}$$ (Eq 43)

The depolarizing factors for each axis can be defined as follows:

$$\alpha_y = \frac{1}{q^2-1} + \frac{q}{(q^2-1)^{\frac{3}{2}}}\ln q + (q^2-1)^{\frac{1}{2}}$$ (Eq 44)

$$\alpha_z = \alpha_x = \frac{1}{2}(1-\alpha_y)$$ (Eq 45)

Where q is the axial ratio defined as q=R_y/R_z. v_1, v_2, v_3 are the volume ratios, and are defined as follows

$$v_1 = \frac{(R_y - d_{om})(R_z - d_{om})^2}{R_y R_z^2}$$ (Eq 46)

$$v_2 = \frac{(R_y - d_{om} - d_{pp})(R_z - d_{om} - d_{pp})^2}{(R_y - d_{om})(R_z - d_{om})^2}$$ (Eq 47)

$$v_3 = \frac{(R_y - d_{om} - d_{pp} - d_{im})(R_z - d_{om} - d_{pp} - d_{im})^2}{(R_y - d_{om} - d_{pp})(R_z - d_{om} - d_{pp})^2}$$ (Eq 48)

Each dielectric constant varies with frequency as follows:

$$\varepsilon = \varepsilon_1 - i\frac{\sigma}{\varepsilon_0 \omega}$$ (Eq 49)

The constants used to calculate the dielectric constants for each section was then taken from Asami *et al.*

[11]

A2 - ACEO Derivation

From Hunter *et al.*, the equation for AC electroosmosis is as follows: [63]

$$U_{eo} = \frac{\varepsilon}{\eta} \langle \zeta E_t \rangle$$ (Eq 50)

Then let: $\zeta = A\, e^{ia}$ and $E_t = B\, e^{ib}$, representing the potential difference across the EDL, and electric field, respectively.

$$U_{eo} = \frac{\varepsilon}{\eta} \langle A\, e^{ia}\, B\, e^{ib} \rangle$$ (Eq 51)

Through the useful identity $\langle A\, e^{ia}\, B\, e^{ib} \rangle = AB \cos\phi = \frac{1}{2}\mathrm{Re}[AB\, e^{j\phi}] = \frac{1}{2}\mathrm{Re}[AB^*]$

Where ϕ is the difference in phase angle between ζ and E_t, U_{EO} simplifies to:

$$U_{eo} = \frac{\varepsilon}{\eta 2}\mathrm{Re}[\zeta {E_t}^*] = \frac{\varepsilon}{\eta 2}\mathrm{Re}[(V - V_0){E_t}^*]$$ (Eq 52)

A3 - Peclet number Calculation

The Peclet number is defined as follows. The constants used were averages over the entire model.

$$Re_L Pr = \boldsymbol{Pe_L} = \frac{Lu}{a}$$ (Eq 53)

Where on the LHS of the equation, Where 'a' is the thermal diffusivity (of water), being 0.143E-6 [m²/s]. [57] L*u is the length scale multiplied by the average velocity, respectively. This comes to a value of 0.0003[m]*0.00002[m/s] = 5.98E-9 [m²/s], using the height of the model, and the highest net velocity.

The height of the model was chosen, because at the chosen operating frequencies, joule heating will most likely occur at the surface. This would lead to a higher temperature gradient in the z direction, at operating conditions. Since dimensionless groups have their characteristic length chosen in the direction of the highest gradient, the height of the model should be considered.

The COMSOL simulation can give an average of the Reynold's number throughout the fluid subdomain. At 1 kHz and 8 Vpp, the conditions that produced the fastest stokes flow, Re was calculated to be 2.18X10⁻⁴. The Prandtl number was calculated through the following:

$$Pr = \frac{v}{a} = \frac{1.04E-6 \left[\frac{m^2}{s}\right]}{0.143E-6 \left[\frac{m^2}{s}\right]} = 7.27 \tag{Eq 54}$$

Thus, the Peclet number, calculated through two different methods are:

$$2.18 \times 10^{-4} \times 7.27 = 1.585E-3 = \boldsymbol{Pe_L}$$

$$\boldsymbol{Pe_L} = \frac{0.0003[m] \times 0.00002 \left[\frac{m}{s}\right]}{0.143 \times 10^{-6} \left[\frac{m^2}{s}\right]} = 0.0418 \tag{Eq 55}$$

Both cases state it is less than 1, stating that heat throughout the model will be most likely transmitted through conduction than through convection.

A4 - Effect of New C_{DL}

By modifying the capacitance to account for the steric effects of the ions, it can be seen that the shielding effect of the EDL is increased. This would make sense, since the EDL would then be modeled thicker. The change in the EDL thickness can be clearly visualized by plotting the difference between the

electrode potential with a constant double layer capacitance (V) and the electrode potential with the

steric effects accounted for in its capacitance (V12). Increasing the electric field would increase the

shielding effect, as seen in Figure 38 between 8 Vpp and 20 Vpp at 1 kHz. At higher frequencies, the
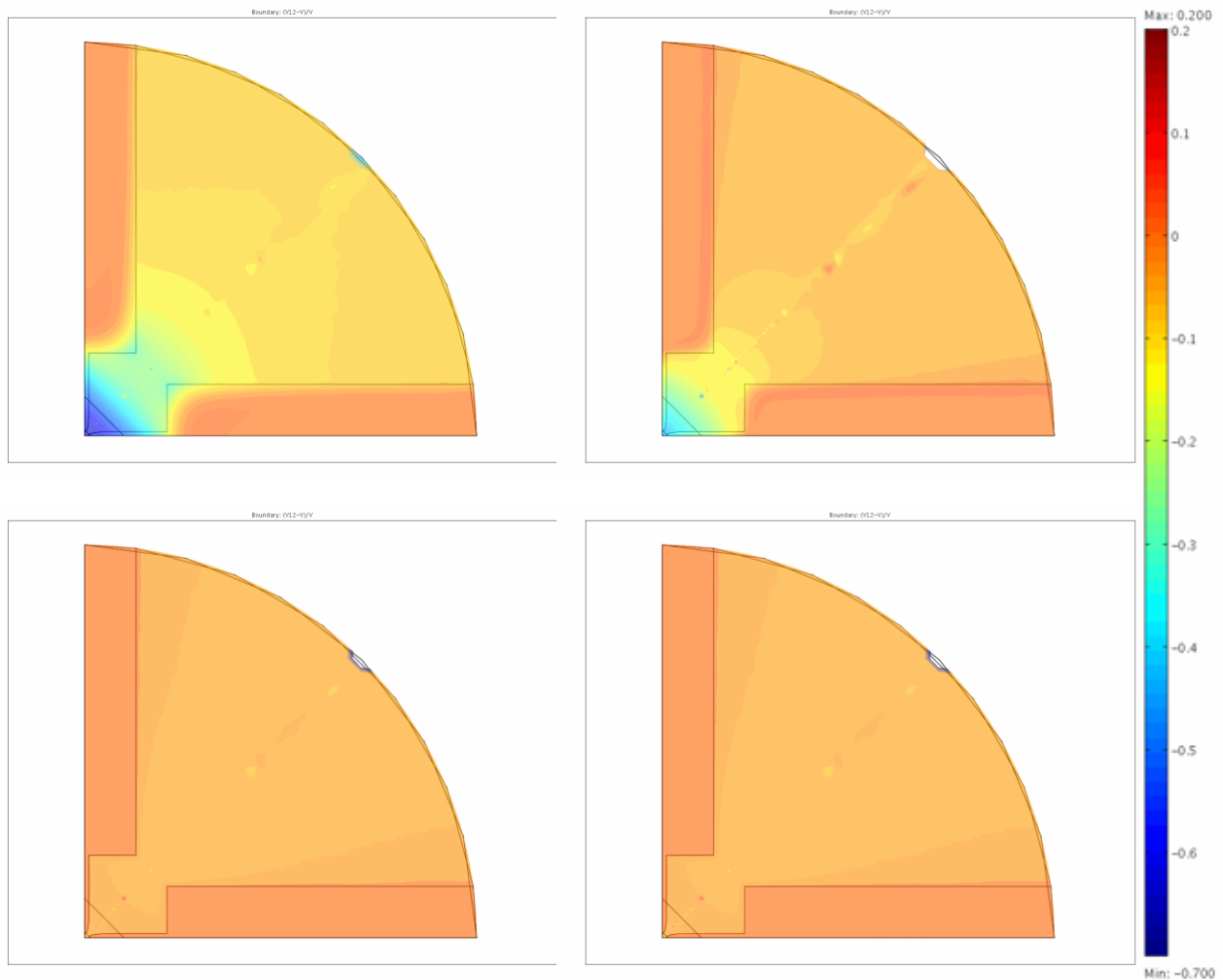

model would just converge to the previous solution.

Figure 38: Figures of the voltage difference (V12-V) as a percentage of the unmodified voltage (V). At higher electric fields, the shield 20 Vpp 1 kHz *e significant, due to steric hindra* 8 Vpp 1 kHz *ating a larger EDL.*

A5 - Charge Relaxation Calculations

The electrical model is a capacitor-resistor model. The resistance 'R' is dependent on l, the length of the

path that the current travels. And this length is dependent on electrode separation through pi.
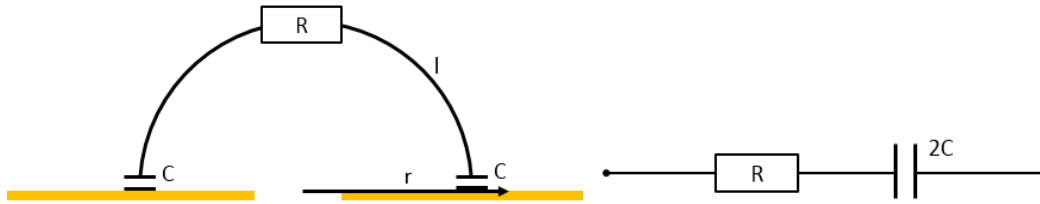
The charge relaxation model for an RC-circuit is calculated as

$$\tau = R \cdot 2C \qquad \text{(Eq 56)}$$

The resistance is given as

$$R = [\Omega\, m^2] = \rho \cdot l \qquad \text{(Eq 57)}$$

Where ρ is resistivity, and l is the length which the current travels, which is a function of the electrode

separation. The capacitance would then be

$$C = \frac{\varepsilon_0 \varepsilon_r}{\lambda} = 0.018251 \left[\frac{F}{m^2}\right] \qquad \text{(Eq 58)}$$

Calculated from the electric permittivity of water and the Debye length.

Then the relaxation period could be estimated as:

$$\tau = 2\rho lC \qquad \text{(Eq 59)}$$

The angular relaxation frequency would then be:

$$\omega = \frac{2\pi}{2\rho lC}$$

A6 - ACEO flow reversal on electrodes

The potential difference across the double layer was plotted along the red line depicted in Figure 39 on a log 10 scale to emphasize the local maxima. In Figure 40, three local maxima can be seen. However, only one directional change was observed. The second local maximum doesn't cover enough area to have a significant impact to overcome the fluid inertial forces to reverse flow. It is only the third local maximum that covers enough area to reverse flow.
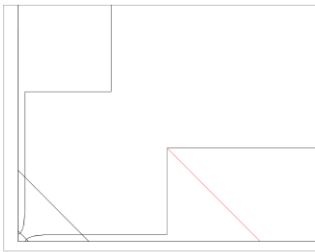

Figure 39: The line for which the potential difference across the EDL was plotted against. The line was drawn from a 45 degree angle from the perpendicular corner.
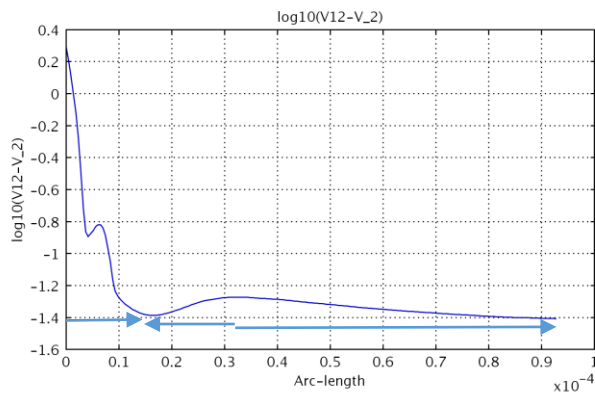

Figure 40: The potential drop along the EDL on a log 10 scale, versus the distance from the tip of the electrode. The arrows indicate the direction of the flow, which is the opposite direction of the electric field tangent to the surface. V_2 is the applied voltage, and V12 is potential at the end of the EDL.

A7 - Predicting ET flow

The electrothermal flow is a function of the thermal gradient, and the potential gradient, or electric field.

Only in the presence of a significant thermal gradient, and electric field, will there be ET flow. To

illustrate this, the product of temperature and the potential were plotted for the frequencies ranging

from 1 kHz, to 1 MHz, at 8 Vpp, with ET flow vectors overlaid. There was no change in the flow pattern

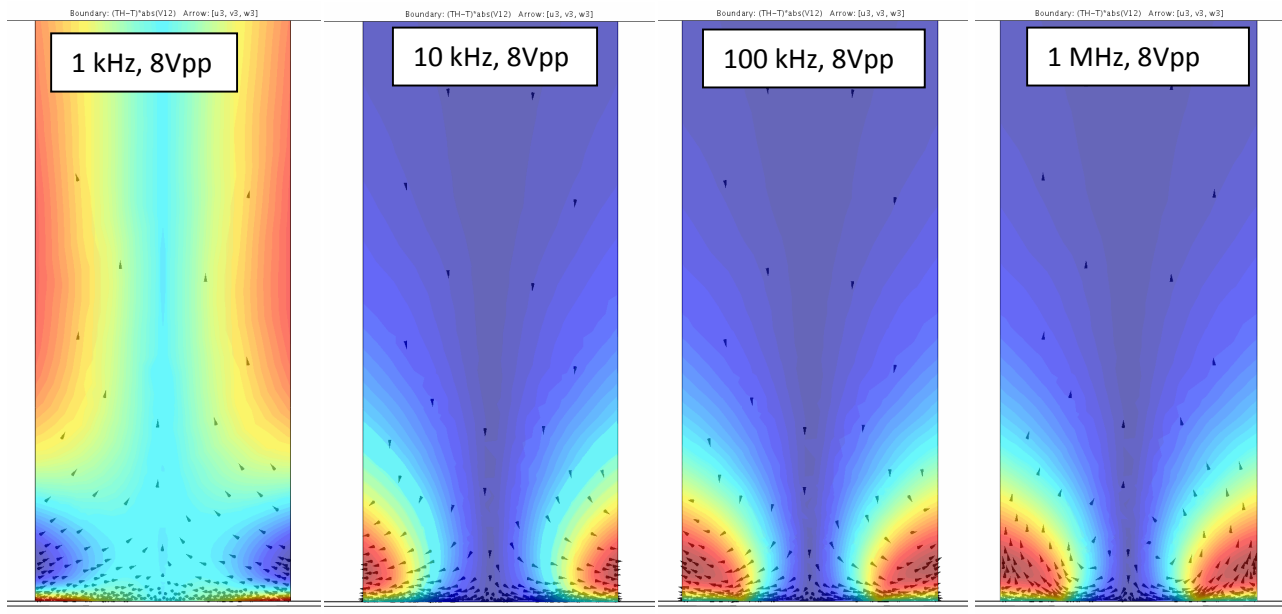at higher voltages, as seen in Figure 30, so only 8Vpp was considered.

Figure 41: Plot of the product of the temperature and the voltage with ET flow vectors overlaid. The electrothermal flow will flow from areas with high temperatures and potential to areas of low temperature and potential.

At 10 kHz, the area with the highest potential and temperature occurs close to the electrode surface.

But at higher frequencies, this area changes shape slightly, enough to incrementally angle the ET flow

upwards, such that the ET flow in the bulk reverses direction at 1 MHz. As seen in Figure 30, the velocity

of the ET flow is greatest at the tips, suggesting the majority of the ET flow direction is determined by

the thermal gradient close to the tips at frequencies higher than 1 kHz.